



**Defense Nuclear Agency
Alexandria, VA 22310-3398**



DNA-TR-94-182

**Multiscale Environmental Dispersion
Over Complex Terrain
The MEDOC Models**

**John Sontowski
Catherine Dougherty
Science Applications International Corporation
997 Old Eagle School Road, Suite 215
Wayne, PA 19087**

May 1996

Technical Report

CONTRACT No. DNA 001-92-C-0151

**Approved for public release;
distribution is unlimited.**

19960530 112

Destroy this report when it is no longer needed. Do not return to sender.

PLEASE NOTIFY THE DEFENSE NUCLEAR AGENCY,
ATTN: CSTI, 6801 TELEGRAPH ROAD, ALEXANDRIA, VA
22310-3398, IF YOUR ADDRESS IS INCORRECT, IF YOU
WISH IT DELETED FROM THE DISTRIBUTION LIST, OR
IF THE ADDRESSEE IS NO LONGER EMPLOYED BY YOUR
ORGANIZATION.



DISTRIBUTION LIST UPDATE

This mailer is provided to enable DNA to maintain current distribution lists for reports. (We would appreciate your providing the requested information.)

- Add the individual listed to your distribution list.
- Delete the cited organization/individual.
- Change of address.

NOTE:

Please return the mailing label from the document so that any additions, changes, corrections or deletions can be made easily. For distribution cancellation or more information call DNA/IMAS (703) 325-1036.

NAME: _____

ORGANIZATION: _____

OLD ADDRESS

CURRENT ADDRESS

TELEPHONE NUMBER: () _____

DNA PUBLICATION NUMBER/TITLE

CHANGES/DELETIONS/ADDITIONS, etc.) (Attach Sheet if more Space is Required)

DNA OR OTHER GOVERNMENT CONTRACT NUMBER: _____



CERTIFICATION OF NEED-TO-KNOW BY GOVERNMENT SPONSOR (if other than DNA):

SPONSORING ORGANIZATION: _____

CONTRACTING OFFICER OR REPRESENTATIVE: _____

SIGNATURE: _____

CUT HERE AND RETURN

DEFENSE NUCLEAR AGENCY
ATTN: IMAS
6801 TELEGRAPH ROAD
ALEXANDRIA, VA 22310-3398

DEFENSE NUCLEAR AGENCY
ATTN: IMAS
6801 TELEGRAPH ROAD
ALEXANDRIA, VA 22310-3398

REPORT DOCUMENTATION PAGE

Form Approved
OMB No. 0704-0188

Public reporting burden for this collection of information is estimated to average 1 hour per response including the time for reviewing instructions, searching existing data sources, gathering and maintaining the data needed, and completing and reviewing the collection of information. Send comments regarding this burden estimate or any other aspect of this collection of information, including suggestions for reducing this burden, to Washington Headquarters Services Directorate for Information Operations and Reports, 1215 Jefferson Davis Highway, Suite 1204, Arlington, VA 22202-4302, and to the Office of Management and Budget, Paperwork Reduction Project (0704-0188), Washington, DC 20503.

1. AGENCY USE ONLY (Leave blank)		2. REPORT DATE 960501	3. REPORT TYPE AND DATES COVERED Technical 920909 – 950331
4. TITLE AND SUBTITLE Multiscale Environmental Dispersion Over Complex Terrain The MEDOC Models		5. FUNDING NUMBERS C - DNA 001-92-C-0151 PE - 62715H PR - AC TA - BD WU - DH327610	
6. AUTHOR(S) John Sontowski and Catherine Dougherty		8. PERFORMING ORGANIZATION REPORT NUMBER	
7. PERFORMING ORGANIZATION NAME(S) AND ADDRESS(ES) Science Applications International Corporation 997 Old Eagle School Road, Suite 215 Wayne, PA 19087		9. SPONSORING/MONITORING AGENCY NAME(S) AND ADDRESS(ES) Defense Nuclear Agency 6801 Telegraph Road Alexandria, VA 22310-3398 SPWE/Hodge	
10. SPONSORING/MONITORING AGENCY REPORT NUMBER DNA-TR-94-182			
11. SUPPLEMENTARY NOTES This work was sponsored by the Defense Nuclear Agency under RDT&E RMC Code B4662D AC BD 00027 4400A AC 25904D.			
12a. DISTRIBUTION/AVAILABILITY STATEMENT Approved for public release; distribution is unlimited.		12b. DISTRIBUTION CODE	
13. ABSTRACT (Maximum 200 words) This report describes a capability called MEDOC which includes a suite of codes used for the assessment/prediction of Multiscale Environmental Dispersion Over Complex Terrain. The codes which were originally developed by and for the nuclear power industry have been adapted under a program described in this report, to a broader range of problems involving chemical and biological, as well as nuclear, sources which are of concern to the U.S. Defense Nuclear Agency (DNA) and the national defense community. MEDOC can operate in either a prognostic or diagnostic mode, providing both the meteorological and the concentration transport/dispersion fields over a range of atmospheric scales from local (~10's of KM), to regional (~100's of KM). Alternate methodologies, from first principles based to more approximate, are provided to allow various degrees of fidelity and computational efficiency. Thus MEDOC provides appropriate models for a variety of applications such as guidance for local scale emergency response, forecasts for regional scale impacts, and future planning studies. The codes are operational on either a super computer (CRAY), or a workstation level platform (IBM RISC/6000), and have been installed on DNA workstations where they are exercised by DNA personnel.			
14. SUBJECT TERMS Meteorology NBC Dispersal Atmospheric Diffusion		15. NUMBER OF PAGES 102	
		16. PRICE CODE	
17. SECURITY CLASSIFICATION OF REPORT UNCLASSIFIED	18. SECURITY CLASSIFICATION OF THIS PAGE UNCLASSIFIED	19. SECURITY CLASSIFICATION OF ABSTRACT UNCLASSIFIED	20. LIMITATION OF ABSTRACT SAR

NSN 7540-280-5500

Standard Form 298 (Rev. 2-89)
Prescribed by ANSI Std. Z39-18
298-102

UNCLASSIFIED

SECURITY CLASSIFICATION OF THIS PAGE

CLASSIFIED BY:

N/A since Unclassified.

DECLASSIFY ON:

N/A since Unclassified.

SECURITY CLASSIFICATION OF THIS PAGE

UNCLASSIFIED

SUMMARY

The dispersion of nuclear, biological, and chemical (NBC) agents released in the atmosphere represents a problem of great concern to the DNA and the defense community as a whole. Modeling of such events is particularly difficult for regions involving complex terrain. Wind and turbulence fields forced to conform to such terrain take on highly 3D distributions which cannot be represented by simple or classical profiles. Resulting material concentration distributions become similarly complicated. The objective of the program reported herein is to provide the DNA with a capability appropriate for atmospheric dispersion of NBC agents over complex terrain. This capability, called MEDOC, represents a suite of codes used for the assessment/prediction of Multiscale Environmental Dispersion Over Complex Terrain involving releases from nuclear and non-nuclear sources.

Originally, the MEDOC codes were developed by and for the nuclear power industry specifically for accidental releases from nuclear power plants. Under the DNA MEDOC Program, they were extended to also address applications involving chemical and biological sources of a nature associated with potential military or terrorist threats. Further, MEDOC is applicable over a broad range of problems, in either a prognostic or diagnostic mode, providing both the meteorological and the concentration fields over a range of atmospheric scales from local (~ 10's of KM), to regional (~ 100's of KM). Alternate codes/modeling methodologies, from first principles based to more approximate, allow computationally efficient applications to a variety of needs such as guidance for local scale emergency response, forecasts for regional scale impacts, and future planning studies. As established codes, MEDOC has been extensively validated. The codes are operational on either a super computer (CRAY), or a workstation level platform (IBM RISC/6000), and have been installed on DNA workstations where they are exercised by DNA personnel. A detailed description of the various MEDOC models and their applicability is included in this report. This is followed by a discussion of the code adaptations performed under the DNA MEDOC Program and then demonstrations and validations of MEDOC are presented. Finally, conclusions and recommendations are offered.

PREFACE

The work presented in this report was performed by SAIC with ARIA Technologies as a subcontractor. Participants from ARIA Technologies were involved in the original development of the MEDOC codes and were thus most intimately familiar with the code structure and performance characteristics. The authors would specifically like to extend their appreciation to Dr. Jacques Moussafir whose highly professional contribution as leader of the ARIA effort, was a key factor in the success of the program. Also, for invaluable contribution to the ARIA effort, the work of Ms. Sylvie Perdriel is gratefully acknowledged.

The authors would also like to thank LTC James Hodge, the DNA technical monitor, and his colleagues LTC Mark Byers and Major Rob Cox of the DNA Weapons Effects Division of the Shock Physics Directorate which sponsored this work. As the DNA CTM, LTC Hodge provided exceptional guidance along with very active, and effective, participation in the application of the MEDOC codes at DNA. Also participating in the application of MEDOC at DNA, LTC Byers and Major Cox provided significant guidance to the program, with LTC Byers being especially helpful in regard to source characterization while Major Cox provided valuable expertise and assistance in matters of meteorology. Finally, a special thank you is extended to Dr. Charles Gallaway of DNA who was most instrumental in initiating the MEDOC Program and guiding it through its earlier stages at DNA.

CONVERSION TABLE

Conversion factors for U.S. Customary to metric (SI) units of measurements.

MULTIPLY \longrightarrow BY \longrightarrow TO GET
TO GET \longleftarrow BY \longleftarrow DIVIDE

angstrom	1.000 000 X E -10	meters (m)
atmosphere (normal)	1.013 25 X E +2	kilo pascal (kPa)
bar	1.000 000 X E +2	kilo pascal (kPa)
barn	1.000 000 X E -28	meter ² (m ²)
British thermal unit (thermochemical)	1.054 350 X E +3	joule (J)
calorie (thermochemical)	4.184 000	joule (J)
cal (thermochemical/cm ²)	4.184 000 X E -2	mega joule/m ² (MJ/m ²)
curie	3.700 000 X E +1	*giga becquerel (GBq)
degree (angle)	1.745 329 X E -2	radian (rad)
degree Fahrenheit	$t_c = (t_f + 459.67)/1.8$	degree kelvin (K)
electron volt	1.602 19 X E -19	joule (J)
erg	1.000 000 X E -7	joule (J)
erg/second	1.000 000 X E -7	watt (W)
foot	3.048 000 X E -1	meter (m)
foot-pound-force	1.355 818	joule (J)
gallon (U.S. liquid)	3.785 412 X E -3	meter ³ (m ³)
inch	2.540 000 X E -2	meter (m)
jerk	1.000 000 X E +9	joule (J)
joule/kilogram (J/kg) radiation dose absorbed	1.000 000	Gray (Gy)
kilobars	4.183	terajoules
kip (1000 lbf)	4.448 222 X E +3	newton (N)
kip/inch ² (ksi)	6.894 757 X E +3	kilo pascal (kPa)
kmp	1.000 000 X E +2	newton-second/m ² (N-s/m ²)
micron	1.000 000 X E -6	meter (m)
mil	2.540 000 X E -5	meter (m)
mile (international)	1.609 344 X E +3	meter (m)
ounce	2.834 952 X E -2	kilogram (kg)
pound-force (lbs avoirdupois)	4.448 222	newton (N)
pound-force inch	1.129 848 X E -1	newton-meter (N-m)
pound-force/inch	1.751 268 X E +2	newton/meter (N/m)
pound-force/foot ²	4.788 026 X E -2	kilo pascal (kPa)
pound-force/inch ² (psi)	6.894 757	kilo pascal (kPa)
pound-mass (lbm avoirdupois)	4.535 924 X E -1	kilogram (kg)
pound-mass-foot ² (moment of inertia)	4.214 011 X E -2	kilogram-meter ² (kg m ²)
pound-mass/foot ³	1.601 846 X E +1	kilogram/meter ³ (kg/m ³)
rad (radiation dose absorbed)	1.000 000 X E -2	**Gray (Gy)
roentgen	2.579 760 X E -4	coulomb/kilogram (C/kg)
shake	1.000 000 X E -8	second (s)
slug	1.459 390 X E +1	kilogram (kg)
torr (mm Hg, 0° C)	1.333 22 X E -1	kilo pascal (kPa)

*The becquerel (Bq) is the SI unit of radioactivity; 1 Bq = 1 event/s.

**The Gray (Gy) is the SI unit of absorbed radiation.

TABLE OF CONTENTS

Section	Page
SUMMARY.....	iii
PREFACE.....	iv
CONVERSION TABLE.....	v
FIGURES.....	viii
TABLES	xii
1 INTRODUCTION	1
1.1 BACKGROUND.....	1
1.2 REPORT ORGANIZATION	2
2 OVERVIEW OF THE MEDOC CAPABILITY.....	3
2.1 CODE STRUCTURE/INTERFACES	3
2.2 CODE ELEMENT DESCRIPTIONS	7
3 ADAPTATIONS/EXTENSIONS OF MEDOC FOR DNA APPLICATIONS	11
3.1 OBJECTIVES	11
3.2 TECHNICAL ADAPTATIONS	12
3.2.1 Agent Decay	12
3.2.2 Agent Evaporation	13
3.2.3 Line Sources.....	16
3.2.4 Atmospheric Stability/Temperature Profile Effects	17
3.2.5 Dosage Capability and Casualty Assessment.....	20
3.3 OPERATIONAL ADAPTATIONS	22
3.3.1 I/O Interface Streamlining	22
3.3.2 TOPOREL - Topography Data Handling	24
3.3.3 HERMIN - Gridded Met Data Inputs.....	24

TABLE OF CONTENTS (Continued)

Section		Page
4	MEDOC DEMONSTRATIONS/VALIDATIONS	26
4.1	VALIDATION HISTORY AND RELATED EFFORTS	26
4.2	ANALYTICAL VALIDATIONS - STABILITY/ TURBULENCE EVAPORATION AND DECAY EFFECTS	28
4.3	SEA BREEZE DEMONSTRATION - GROUND/ ATMOSPHERE INTERACTION EFFECTS	39
4.4	SIESTA - COMPLEX TOPOGRAPHY EFFECTS	47
	4.4.1 What is SIESTA?	47
	4.4.2 The SIESTA Model Evaluation Process	47
	4.4.3 HERMES Validations with SIESTA	54
	4.4.4 TRAMES Validations with SIESTA	73
5	CONCLUSIONS	84
6	REFERENCES	86

FIGURES

Figure		Page
2-1	The primary MEDOC codes	4
2-2	Detailed structure of the MEDOC code system	6
3-1	Transport/dispersion over Southern California without species decay.	14
3-2	Transport/dispersion over Southern California with species decay.	14
3-3	Dispersion from atmospheric line source shortly after release.	18
3-4	Dispersion from atmospheric line source at later time after release (side view).	18
3-5	Dispersion from atmospheric line source at later time after release (top view).	19
4-1	HERMES concentration profiles with and without decay in uniform wind and turbulence fields.	30
4-2	Contour width variations from HERMES calculation and analytic solution for unstable atmosphere.	32
4-3	Axial variation of concentration from HERMES calculation and analytic solution for an unstable atmosphere.	33
4-4	Crosswind and vertical profiles of concentration from HERMES calculation and analytic solution for an unstable atmosphere.	33
4-5	Contour width variations from HERMES calculation and analytic solution for a neutral atmosphere.	36
4-6	Contour width variations from HERMES calculation (400 m grid) and analytic solution for a stable atmosphere.	37

FIGURES (Continued)

Figure		Page
4-7	Contour width variations from HERMES calculation (200 M grid) and analytic solution for a stable atmosphere.	38
4-8	Initial wind field for HERMES sea breeze calculation	40
4-9	Initial land and sea surface temperature for HERMES sea breeze calculation.	42
4-10	Mid day land and sea surface temperatures from HERMES sea breeze calculation.	43
4-11	Midnight land and sea surface temperatures from HERMES sea breeze calculation.	44
4-12	Wind profile in a vertical plane at initiation of HERMES sea breeze calculation.	45
4-13	Wind field in a vertical plane at mid day from HERMES sea breeze calculation.	46
4-14	3D View of SIESTA topography on 30 November.	50
4-15	Elevation contours with stationary wind vectors for SIESTA topography on 30 November.	51
4-16	3D View of SIESTA topography on 24 November.	52
4-17	Elevation contours with stationary wind vectors for SIESTA topography on 24 November.	53
4-18	Ground level concentration contours with color shading for 30 November based on HERMES with CONDOR winds. . . .	55
4-19	Cumulative distribution [%] of different models for SIESTA 30th versus PMCD- or PCMD- ratio > 1	56
4-20	Scatter diagram for HERMES/CONDOR calculated concentrations for 30 November SIESTA Experiment.	57

FIGURES (Continued)

Figure		Page
4-21	Isoconcentration surface (100 NG/M3) for HERMES/CONDOR calculated concentrations for 24 November SIESTA Experiment.	59
4-22	Plume cross section in North-South vertical plane through HERMES/CONDOR calculated concentration field for 24 November SIESTA Experiment.	61
4-23	Ground level concentration contours with color shading for 24 November based on HERMES with CONDOR winds.	62
4-24	Cumulative frequency distribution for HERMES calculation with CONDOR winds on 24 November.	63
4-25	Scatter diagram for HERMES calculation with CONDOR winds on 24 November.	63
4-26	Ground level concentration contours with color shading for 24 November based on HERMES with stationary MINERVE winds.	64
4-27	Ground level concentration contours with color shading for 24 November based on HERMES with nonstationary MINERVE winds.	65
4-28	Cumulative frequency distribution for HERMES calculation with stationary MINERVE winds on 24 November.	66
4-29	Scatter diagram for HERMES calculation with stationary MINERVE winds on 24 November.	66
4-30	Cumulative frequency distribution for HERMES calculation with nonstationary MINERVE winds on 24 November.	68
4-31	Scatter diagram for HERMES calculation with nonstationary MINERVE winds on 24 November.	68
4-32	Bar indicator comparisons between SIESTA measurements on 24 November and HERMES calculations with nonstationary MINERVE winds.	70

FIGURES (Continued)

Figure		Page
4-33	Ground level concentration contours with color shading for 30 November based on TRAMES with CONDOR winds.	71
4-34	Scatter diagram for TRAMES/CONDOR calculated concentrations for 30 November SIESTA Experiment.	72
4-35	Ground level concentration contours with color shading for 30 November based on TRAMES with stationary MINERVE winds.	74
4-36	Cumulative frequency distribution for TRAMES calculations with stationary MINERVE winds on 30 November.	75
4-37	Scatter diagram for TRAMES calculations with stationary MINERVE winds on 30 November.	75
4-38	Cumulative frequency distribution for TRAMES calculations with CONDOR winds on 30 November.	76
4-39	Ground level concentration contours with color shading for 24 November based on TRAMES with CONDOR winds.	77
4-40	Ground level concentration contours with color shading for 24 November based on TRAMES with stationary MINERVE winds.	79
4-41	Cumulative frequency distribution for TRAMES calculations with stationary MINERVE winds on 24 November.	80
4-42	Scatter diagram for TRAMES calculations with stationary MINERVE winds on 24 November.	80
4-43	Ground level concentration contours with color shading for 24 November based on TRAMES with nonstationary MINERVE winds.	81
4-44	TRAMES trajectories for nonstationary MINERVE winds on 24 November.	82

TABLES

Table		Page
4-1	Plume contour widths for an unstable atmosphere	32
4-2	Decay Fraction Comparisons	34
4-3	Plume contour widths for a neutral atmosphere	36
4-4	Plume contour widths for a stable atmosphere (400 m HERMES grid)	37
4-5	Plume contour widths for a stable atmosphere (200 m HERMES grid)	38

SECTION 1

INTRODUCTION

1.1 BACKGROUND.

MEDOC consists of a suite of codes used for the assessment/prediction of Multiscale Environment Dispersion Over Complex Terrain involving releases from nuclear and non-nuclear sources. Both the meteorological conditions as well as the material transport/dispersion fields are calculated with state-of-the-art models. Separate capabilities are included for either diagnostic or prognostic computations, and applicability extends over a range of scales from local scales requiring sub-kilometer resolution (10's of KM regions) to regional scales (100's of KM). Originally, the MEDOC codes were developed by the French Electricity Board (Electricite De France - EDF) specifically for accidental releases from nuclear power plants. For that purpose, extensive code validations have been performed over a period of nearly ten years for a variety of conditions, especially including complex terrain.

Under the DNA contract reported on here, the MEDOC capability was extended to also address applications involving chemical and biological sources, and other scenarios of concern to the national defense community. Also as part of the contract, the MEDOC codes have been installed on DNA computers where they are exercised by DNA personnel. The codes are operational on either a super computer (CRAY), or a workstation level platform (IBM RISC/6000). Thus the MEDOC codes provide a potentially vital tool for DOD activities requiring assessment and prediction of impacts due to hazardous materials released in hostile actions by military or other aggressive forces. For such purposes the codes can be applied in either a quick response or a long term planning mode. DNA initiatives such as the Hazardous Prediction and Assessment Capability (HPAC) represent ideal platforms for applications of MEDOC.

1.2 REPORT ORGANIZATION.

The following sections provide an overview of the MEDOC capability, a discussion of the modifications implemented for DNA applications, demonstration/validation results, and finally the summary and conclusions. The overview is given in Section 2 and first covers the overall code structure followed by a brief description of the key elements of MEDOC. The code adaptations are covered in Section 3 and include those of both a technical and an operational nature. Section 4 includes a cross section of demonstration and validation results intended to cover the various aspects of the MEDOC capability which are particularly important to DNA problems of interest. Finally the summary and conclusions are given in Section 5, followed by References in Section 6. As will be indicated later in the report, many of the references provide more detailed descriptions of the various key elements of MEDOC, both the technical and user aspects.

SECTION 2

OVERVIEW OF THE MEDOC CAPABILITY

2.1 CODE STRUCTURE/INTERFACES.

As noted above the MEDOC capability addresses both the meteorology and the material transport/dispersion problems and does so in both a prognostic and diagnostic mode while considering a range of scales from local to regional. Applications therefore require inputs for meteorology and material sources as well as terrain elevations. Meteorological inputs can be either gridded outputs from medium range forecast models, into which the MEDOC codes are nested, or they can be real time meteorological data from an irregular network of weather observation stations. The former would thus be utilized by MEDOC in the prognostic or forecast mode with the latter being used for diagnostic or nowcast calculations. Generally the forecast mode is employed at the regional scale as transport times are relatively long and require prognostic calculations. On the other hand, transport times across local regions are short and can be adequately, and most efficiently, treated in the nowcast mode. Forecasts at the local scale however, can be provided by using the efficient local scale model to refine regional scale forecast results in particular subregions of interest. In addition to the use of meteorological inputs from medium range forecast models or from real time weather observations, the MEDOC codes can also be driven by historical data and/or academic profiles which may be useful for parametric investigations and longer term planning exercises.

The MEDOC capabilities described above are illustrated in Figure 2-1 in terms of specific MEDOC codes. The primary MEDOC codes, shown within the enclosed area (dashed line) of Figure 2-1 include HERMES, HERMIN and MINERVE for meteorology along with TRAMES, HERMES and SPRAY for material transport and dispersion. Some details concerning the nature of these codes are given in the next subsection. In terms of applications, HERMES is generally used at the regional scale with HERMIN or MINERVE being employed at the local scale. Within the MEDOC system the meteorological codes provide the inputs,

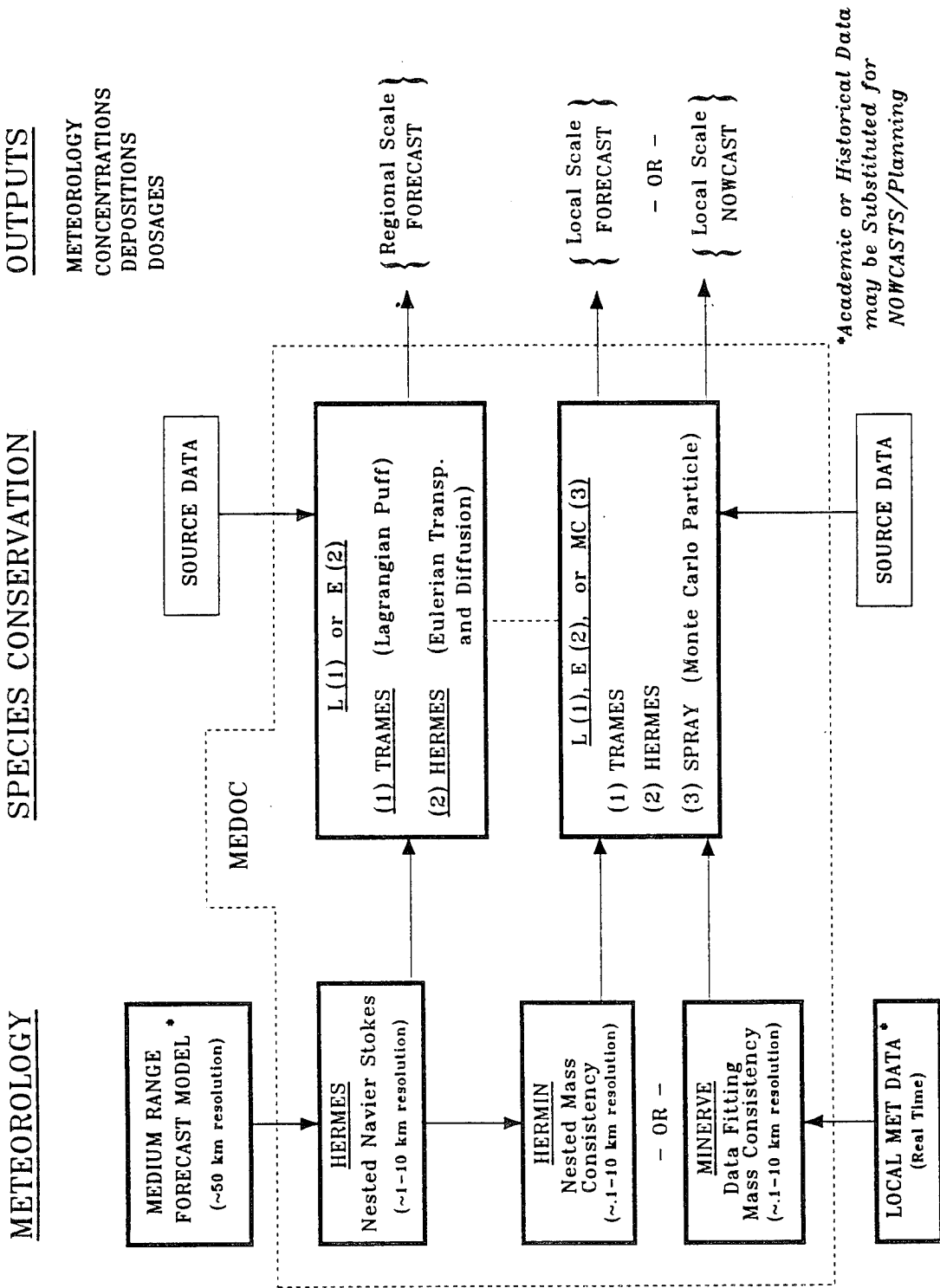


Figure 2-1. The primary MEDOC codes.

primarily wind fields, necessary to run the material transport codes. Source data in terms of species characteristics, release rates and timing are input from outside the primary system.

To support the primary MEDOC codes and basically provide interfaces with the user and input data, various support routines are included in the MEDOC system. These are shown in Figure 2-2 which gives a more detailed illustration of the MEDOC structure. The primary MEDOC codes are again shown in Figure 2-2 within the enclosed inner area of the diagram which now shows more details concerning input/output to the primary codes. Essentially, input data involving topography, cartography if available, and meteorology, must be processed to be in formats and coordinate systems consistent with the primary codes. For this purpose a software system and database structure has been established under the name ADSO. Consistent files created within this structure then serve as the inputs to the primary codes. Since input data may be available in an unlimited number of forms, from scattered raw data to files of regularly gridded data, it is generally required to construct routines to process such data into forms/formats established for MEDOC.

In the case of topography, a comprehensive high resolution source of data is the Defense Mapping Agency (DMA) Digital Terrain Elevation Data (DTED). As these data are provided in a unique variable grid, dependent on latitude, a special routine called TOPOREL was constructed to accept the DTED data from a DTED reader supplied by DNA. Further since such data are generally provided in terms of latitude and longitude, while the primary MEDOC codes are more conveniently written in terms of a rectangular grid in UTM (Universal Transverse Mercator) coordinates, MEDOC also includes a routine called RELIEF which converts terrain data to UTM coordinates. In addition RELIEF includes processing capabilities for topographical filtering/smoothing, changing of grid resolution and the selection of subregions. The resulting topography files are then entered into the ADSO database for subsequent input to the primary MEDOC codes.

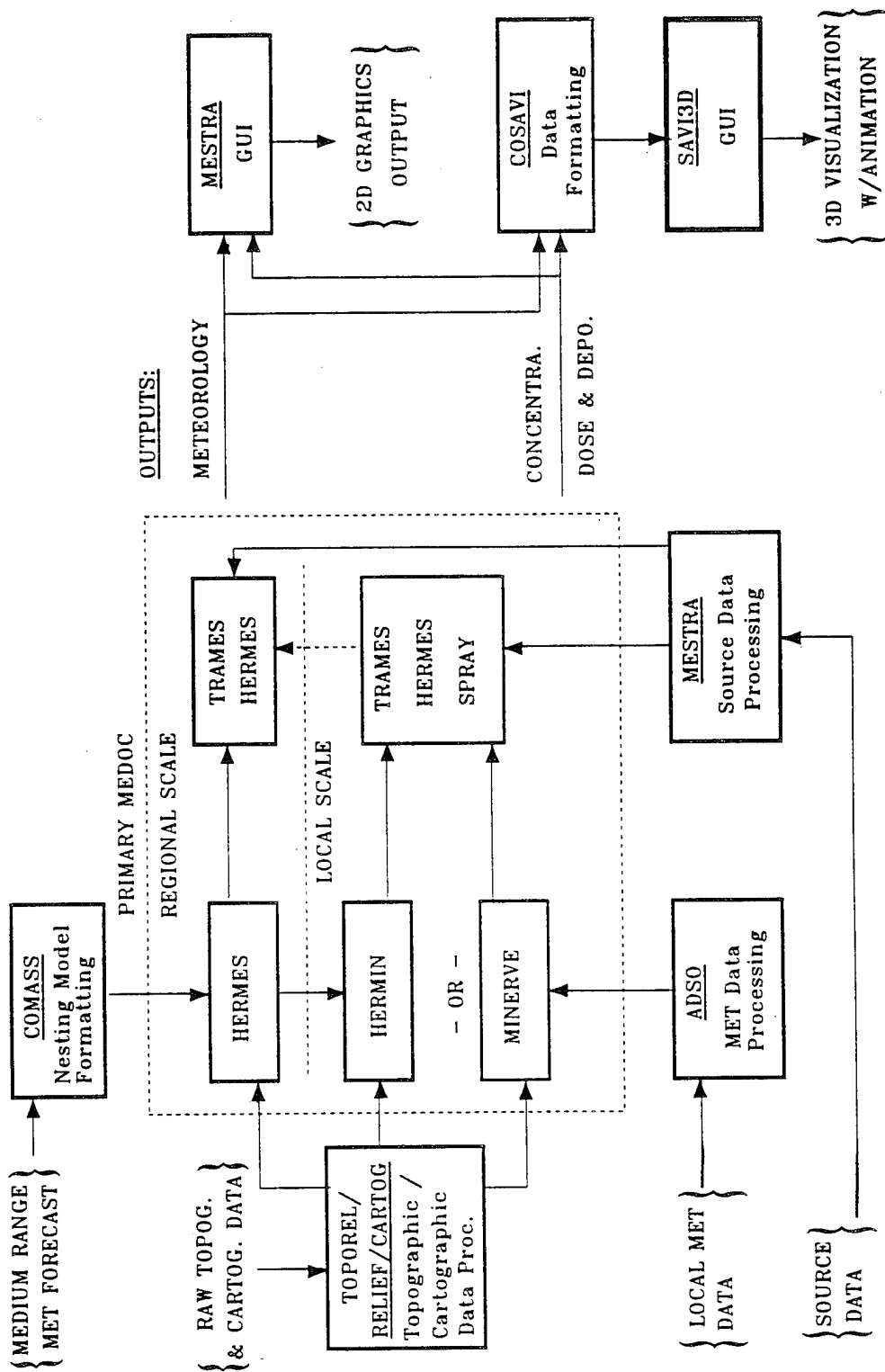


Figure 2-2. Detailed structure of the MEDOC code system.

For meteorological inputs the ADSO system provides routines for data handling, including scalar and vector field interpolation, data display, consistency evaluation, and data masking. The resulting inputs are generally used for diagnostic modeling as performed by MINERVE and displayed at the bottom of Figure 2-2. Such processing is most important for weather observation data which involve measurements from scattered locations, for different time periods, and with different sensor types for the same physical quantities. In the case of gridded met data which are used by prognostic models such as HERMES and obtained from larger scale forecast models, a specialized routine is required for each such model in order to provide the proper MEDOC formats and coordinate transformation. This is illustrated in Figure 2-2 where the routine COMASS was developed for interfacing with the MASS mesoscale forecast model (Reference 1). Source data are fed into the transport models through a processor called MESTRA as shown at the bottom of Figure 2-2.

Turning to the outputs from the primary MEDOC codes, two basic systems are provided for output display. These include the same MESTRA processor as used for source data input, as well as an alternate capability called savi3D. These are illustrated on the right in Figure 2-2. As indicated, the MESTRA capability is limited to 2D graphics while savi3D provides 3D visualizations and animation. savi3D is a separate stand-alone graphics capability (Reference 2) provided by Supercomputer Systems Engineering and Services Company (SSESCO). To provide the necessary conversions from the MEDOC binary file outputs to the savi3D formats a special routine called COSAVI has been developed and inserted into the system as shown in Figure 2-2.

2.2 CODE ELEMENT DESCRIPTIONS.

This section presents a summary description of the primary MEDOC codes with references to more detailed reports covering technical and user aspects of the codes. Of key importance amongst the primary codes is HERMES which provides a capability for calculating both the meteorology and the material transport/dispersion. HERMES is a first principles Eulerian Navier-Stokes solver which is most often applied on the regional scale. For meteorology it

provides a solution to the primitive equations, making the hydrostatic assumption. Dry or moist atmospheres are considered, with conservation equations included for vapor and liquid water in the latter case. The solution is generated using finite differences on a Cartesian grid with reduced pressure (sigma) coordinates in the vertical.

Various parameterizations, as well as a turbulence kinetic energy solver, are available in HERMES as options for turbulence modeling. The parameterizations for planetary boundary layer turbulence include the Louis formulation, Reference 3, which is the preferred turbulence model used in forecasting by the European Center for Medium Range Weather Forecasts (ECMWF). Also available is the more robust, though less refined, O'Brien model, Reference 4. For higher order turbulence modeling, a one equation kinetic energy solver is provided with the dissipation parameterized in terms of the dissipation length scale. Determination of the dissipation and mixing length scales is based on the Therry-Lacarrére theory, Reference 5. For surface layer turbulence, either the Louis or the Businger-Dyer models, References 4 and 6, can be used. Utilizing formulations which are proven and accepted within the meteorological community, the HERMES turbulence options comprise a comprehensive and flexible capability for both state of the art and computationally efficient atmospheric turbulence modeling.

Hydrological and thermal conditions at the ground can be specified as boundary conditions or calculated by solution of a ground/atmosphere interface model (Deardorff Two Reservoir Model, Reference 3). Remaining boundary and initial conditions can be obtained by nesting with output from a larger scale meteorological forecast model, in which case HERMES operates in a prognostic mode. Alternatively, HERMES can be applied in a diagnostic mode, as in planning analyses, where it can be driven by individual meteorological soundings, academic profiles, or by gridded fields from historical sources.

Along with the basic HERMES equations for meteorology is a separate equation for conservation of a passive scalar which allows solution for the concentration fields due to transport and dispersion of hazardous materials. Being uncoupled from the flow field equations, the concentration solver, which involves a relatively minor computations burden, can be efficiently

exercised repeatedly for various alternate release scenarios. This can be quite valuable in an emergency response situation where the source condition is not clearly defined. In addition, common file structures within the MEDOC system also allows the HERMES concentration solver to be driven by wind fields from the MEDOC diagnostic solver (MINERVE) which is described below. Further description of the technical and user aspects of HERMES is provided in References 7 and 8, respectively.

For local or "near to the source" scales (~ 10 's of KM), response time is generally limited and therefore computational efficiency is paramount. In such cases MEDOC uses a mass consistency model (MINERVE) in conjunction with local meteorological observations to construct wind fields in a diagnostic mode. MINERVE is based on a variational formulation which minimizes differences (in a least squares sense) between the solution field and the observed field. This is done with the strong constraint that the solution satisfy the mass conservation (continuity) equation. Thus the solution contains no artificial sources or sinks which is of importance when the wind field is utilized in material transport calculations. To accommodate terrain, MINERVE is written in a terrain following coordinate systems. Thus, terrain slopes are realistically modeled, which is essential in certain situations such as drainage flows. Finally, MINERVE models atmospheric stability effects by controlling the relative adjustment of the vertical and horizontal wind components according to stability conditions which are either user specified or derived from available temperature profiles and surface roughness. The nature of the MINERVE formulation allows very rapid computations, typically on the order of a minute per time frame on a workstation (IBM RISC/6000). This is based on a MINERVE solution algorithm which uses a highly accurate 27 point block SOR (successive over-relaxation) method. A more recently developed version using a 15 point solver has been found to also give excellent results with a significant reduction in computation time as well as reduced storage requirements. Further technical and user related information (in French) concerning MINERVE is available in References 9 and 10, respectively.

In addition to the HERMES Euler based material transport model, MEDOC also includes a Gaussian puff/Lagrangian model called TRAMES. As a Gaussian solver, using analytic

distributions, it is significantly faster computationally than the HERMES code. It provides more approximate and limited solutions however since the parameterized analytic distributions are imposed directly upon concentrations. HERMES on the other hand parameterizes more basic turbulence quantities (diffusivities, or dissipation and length scales) and thus allows more general concentration distributions. Turbulence is characterized with TRAMES by user specification of standard atmospheric stability categories and corresponding correlations for the puff sizes (horizontal and vertical σ 's). Options for stability classification include the Pasquill-Gifford, Briggs, and Brookhaven correlations. As an alternative to user specification of stability, temperature data, if available, can be used to allow automatic selection of stability class. More complete information regarding TRAMES is available in Reference 11.

While HERMES and TRAMES serve as a very effective pair of capabilities which provide both accuracy and computational efficiency sufficient for most problems of interest, MEDOC also includes a third option for material transport/diffusion which is called SPRAY. The basis of SPRAY is a Monte Carlo approach which treats individual/random particle motions in sufficient number to give realistic statistical distributions of particles. Eddy diffusivities need not be defined, as random motions are related to turbulence statistics which are commonly measured and/or readily parameterized in terms of atmospheric stability and surface conditions. Complex turbulent motions, particularly those associated with strong convection as well as highly sheared and separated flows, can thus be simulated with superior accuracy and detail. In addition, the Monte Carlo methodology is grid-free and as a result can most efficiently provide a high degree of time and space resolution. Unlike TRAMES and HERMES, the status of SPRAY is more of a research rather than an operational tool. It is described in more detail in Reference 12. The full complement of MEDOC primary codes thus represents a comprehensive state-of-the-art capability for carrying out both meteorological and hazardous material transport calculations.

SECTION 3

ADAPTATIONS/EXTENSIONS OF MEDOC FOR DNA APPLICATIONS

3.1 OBJECTIVES.

As the MEDOC codes were originally developed for applications involving nuclear power plant accidents, the primary adaptations required for DNA purposes are those aimed at chemical and biological sources of types expected in military and other defense related activities. Thus the required adaptations involve extensions to the nature and behavior of the hazardous material species being transported, and the configuration/geometry as well as timing of their release. Concerning species behavior, the key adaptations made to MEDOC involve decay and evaporation, while source configurations were extended to allow treatment of arbitrarily oriented lines in space. Thus behavior typically associated with chemical and biological agents as well as potential source configurations associated with military delivery systems can now be modeled with MEDOC. Other modifications to MEDOC involve extension of the methodology for determination of atmospheric stability and of the dosage calculation capability along with casualty assessment.

Along with the technical adaptations involving MEDOC phenomenology as noted above, changes of an operational nature were also made to MEDOC in order to accommodate differences between the originally intended MEDOC user and the expected DNA/DOD user. These adaptations have primarily involved streamlining and tailoring of the user interfaces for DNA applications and users. Also as the DNA/DOD user is expected to have specialized sources of input data, special routines were also developed to interface with such data. Details concerning the above noted adaptations, first technical then operational, are given in the following two subsections.

3.2 TECHNICAL ADAPTATIONS.

3.2.1 Agent Decay.

A key facet of the behavior of many NBC agents is a decay process associated with aging after atmospheric release. In many cases this can be described as a first order reaction in which decay occurs at a rate proportional to the first power of the local concentration. The proportionality constant can then be defined in terms of a known half-life for the particular agent. Such a description provides a realistic approximation for radioactive decay of nuclear species and for chemical decay of species dependent on reaction with ambient constituents of relatively constant concentrations. For biological agents however, the aging process/decay rate can be most significantly influenced by sunlight. Thus, while decay might still be represented by a first order reaction, the proportionality "constant" could be varying as a function of solar irradiance.

To provide a capability more appropriate for decay of biological agents, MEDOC was extended to factor in a dependence of decay rate on solar irradiance. Since the solar conditions are essentially determined by latitude, time of year and time of day, and since these are part of standard MEDOC inputs, a geographically specific diurnal variation of irradiance is readily determined as part of the MEDOC simulation. Thus, given a dependence of half-life on irradiance level for a specified agent, MEDOC can automatically account for a diurnally varying decay rate. This has been incorporated into MEDOC by setting up a special input file in which the user specifies species half-life at several selected irradiance levels covering the expected diurnal range. Within this range, MEDOC then determines the time specific half-life/decay rate by linear interpolation. This procedure has been implemented in the HERMES concentration model. In this case, the governing equation for transport and diffusion of a passive scalar is modified to include an additional term which represents the decay, i.e., a species sink for viable agent. This term is linear in the concentration and includes a time constant determined by the diurnally varying half-life. Also, to accommodate future upgrades the routine for controlling

decay rates was modified in a way to readily allow decay rate dependence on other potentially important factors such as air temperature, humidity and cloud cover.

While the above modifications have been performed to the HERMES code, the TRAMES puff model is also capable of treating first order decay. In the case of a puff model, the linear decay results in the individual puff concentrations being reduced by an exponential function of the puff age and the time constant or species half-life. Although the time constant can be changed at each computation step to reflect irradiance effects as above, TRAMES presently assumes a non varying time constant.

As an illustration of the MEDOC decay capability, two sample HERMES results are shown for an identical case, first without decay in Figure 3-1 and second with decay in Figure 3-2. The modelled region covers a 200 KM square area of Southern California with ocean in the southwest portion and the San Bernardino and San Jacinto mountains to the east. Two sources were specified along the seacoast in the Los Angeles area, with prevailing winds from the west. The wind field was adjusted to the topography by means of the MINERVE code. The simulations were made over a 30 hour period with 30 second releases each 3 hours at the 2 sites. Figures 3-1 and 3-2 show results at the end of the 30 hour period in the form of 3D isoconcentration surfaces with colors indicating direction of the surface outward normals (upward-red, horizontal-green). For the simulation with decay, rates were assumed as those typical of anthrax with diurnal variations included as discussed above. While the effects of decay are obvious in comparing Figures 3-1 and 3-2, it is also worth noting that the topography has significant effect as well. This effect is enhanced by the assumed stable atmospheric conditions which retard vertical transport in the vicinity of the higher terrain features.

3.2.2 Agent Evaporation.

As MEDOC was developed for nuclear sources, it included no capability for evaluation of evaporating agents. For chemical agents, evaporation is often highly important. Such evaporation is generally treated as two separate parts, primary evaporation and secondary



Figure 3-1. Transport/dispersion over Southern California without species decay.



Figure 3-2. Transport/dispersion over Southern California with species decay.

evaporation. Evaporation which occurs from atmospherically entrained particles after release at altitude is referred to as primary; evaporation from ground surfaces after deposition of particles is called secondary. The objective under the current MEDOC Program was to develop a primary capability which could later be extended to include secondary evaporation.

Within MEDOC, evaporation can be incorporated into either the HERMES Eulerian transport code or the TRAMES Lagrangian puff code. Considering the advantages and disadvantages of these alternatives, it was decided to develop HERMES for this purpose. The primary reason for this selection was that since HERMES allows area source boundary conditions at the ground surface, it would facilitate future implementation of the secondary evaporation capability. Further, HERMES is expected to more realistically model diffusion from higher altitude releases where turbulence differs significantly from that of the planetary boundary layer for which the more commonly employed empirical diffusion models were developed. Finally, as an Eulerian model, HERMES provides an approach which is an independent alternative to the existing evaporation codes such as NUSSE and VLSTRACK.

To accommodate evaporation in HERMES, each size from the initial particle size distribution is treated as an individual species which is transported and diffused according to the HERMES passive scalar transport equation. This includes fallout and evaporation which occurs at rates dependent upon the particle diameters as well as agent properties such as vapor pressure, molecular weights, and the critical temperature and pressure. Diameter reductions due to evaporation are determined at each computational time step for each initial size class. The corresponding evaporation from each class at each time step then contributes to a primary vapor source term in the conservation equation for the vapor species. Particles reaching ground level are deposited where they then contribute to the source terms for secondary evaporation. HERMES thus provides, along with the secondary evaporation source, the spatial distribution of mass concentration for each initial particle size and for the primary vapor. In addition, a summation of particle mass over all particle sizes is calculated at each grid point. Thus HERMES has been adapted to provide a unique methodology amongst commonly used DoD models for the treatment of primary evaporation, with preliminary accommodations included for

the calculation of secondary evaporation. As the evaporation formulation is at an interim stage, with secondary evaporation to be included later, documentation currently is limited to comment statements within the evaporation source code.

3.2.3 Line Sources.

The simulation of chemical and biological threats associated with military conflict in many cases involves instantaneous, and near instantaneous, sources which are characterized as a line through the atmosphere. Such a configuration might result from bulk release from an attack missile, spray release from an aircraft, or a munitions leaker subsequent to theater high altitude missile intercept. The line configuration which results can thus have any orientation in space which may or may not intersect with the ground. Since the line source configuration becomes the initial source condition for MEDOC, and since MEDOC was not originally structured for such sources, a modification was required. It should be noted that another source configuration typical of military conflicts is a cloud/airburst at altitude. Since MEDOC/HERMES allows Gaussian clouds as initial conditions, modifications for this purpose were not required.

To accommodate line sources with MEDOC, a program was written to accept near instantaneous line source specifications and cast them into a form and format consistent with the standard MEDOC source files. Thus no changes were required to the material transport and dispersion codes (HERMES and TRAMES) which call these sources files. For description of the line, a series of two or more points in space are specified with MEDOC then constructing straight lines connecting the points. Thus it is possible for the user to specify a piecewise linear source through the computation domain. Source strength is then defined uniformly along the entire line.

To illustrate the MEDOC line source capability, sample results were generated with TRAMES for a source which is initiated at 1 km altitude above ground and continues in a straight line to a ground level intersection. The calculation was performed for a complex topography with the wind field being calculated with MINERVE using local met data. Figure 3-3 shows results,

shortly after source release, as an isoconcentration surface. At this early time the contour surface appears as an elongated cloud along a nearly straight line. At a later time, displayed in Figure 3-4, the contour surface is seen to be highly distorted and broken apart as a result of the 3D wind fields induced by the complex topography. This is further illustrated in Figure 3-5 which provides a view from above at the same time.

3.2.4 Atmospheric Stability/Temperature Profile Effects.

In producing a mass consistent 3D wind field which conforms to complex topography, MINERVE must perform adjustments to the three wind components at all grid locations. For such adjustments to be physically realistic however, they should reflect conditions of atmospheric stability which affect the relative amount of vertical and horizontal motions. In addition, the amount of vertical motion is affected by the topography, as steepness of local slopes induces such motions. To incorporate these effects of stability and topography, MINERVE involves a coefficient α which controls the relative amount of vertical and horizontal adjustments to the wind. A value of $\alpha = 1$ would give equal weight to horizontal and vertical adjustments and therefore tend to represent neutral conditions. Smaller α would reduce the vertical adjustment relative to the horizontal and therefore correspond to stable conditions, while larger α simulates unstable atmospheres. Since stability is determined by atmospheric properties such as wind speed and, most importantly, the vertical profile of temperature, these properties also affect the value of α . Specification of values for α consistent with properties of the atmosphere along with characteristics of the topography is thus seen as an important step in obtaining a MINERVE solution.

As stability can be a spatially varying property of the atmosphere, e.g., inversions aloft, MINERVE also allows for spatial variation of α . In the simplest applications however, reasonable approximations are obtained with a uniform value of α which is specified by the user. This, however, requires that the user be knowledgeable with regard to the existing stability

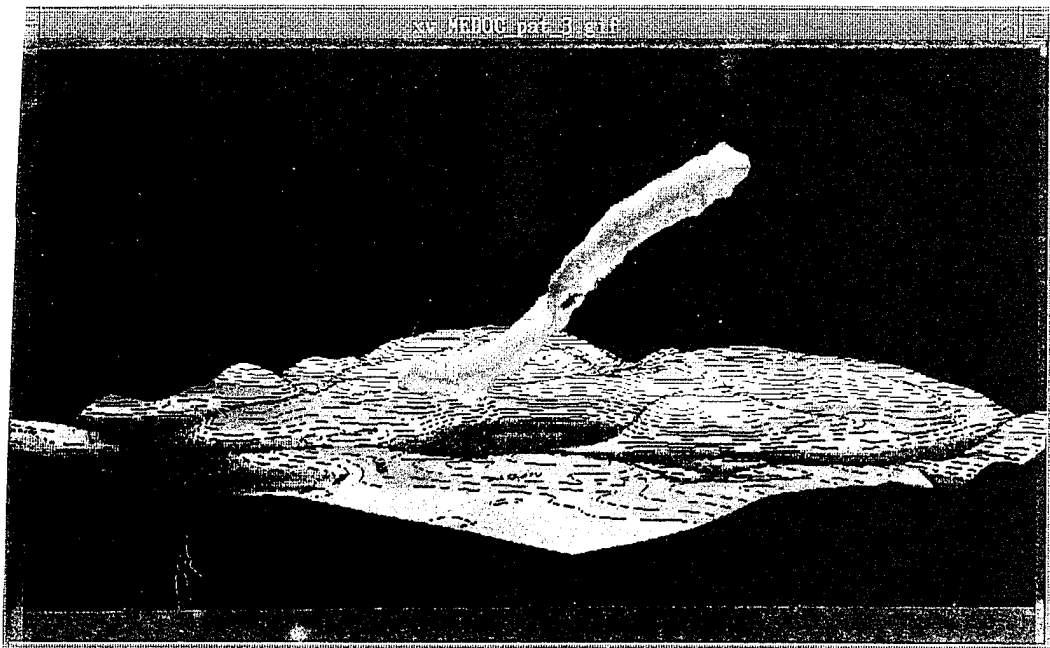


Figure 3-3. Dispersion from atmospheric line source shortly after release.

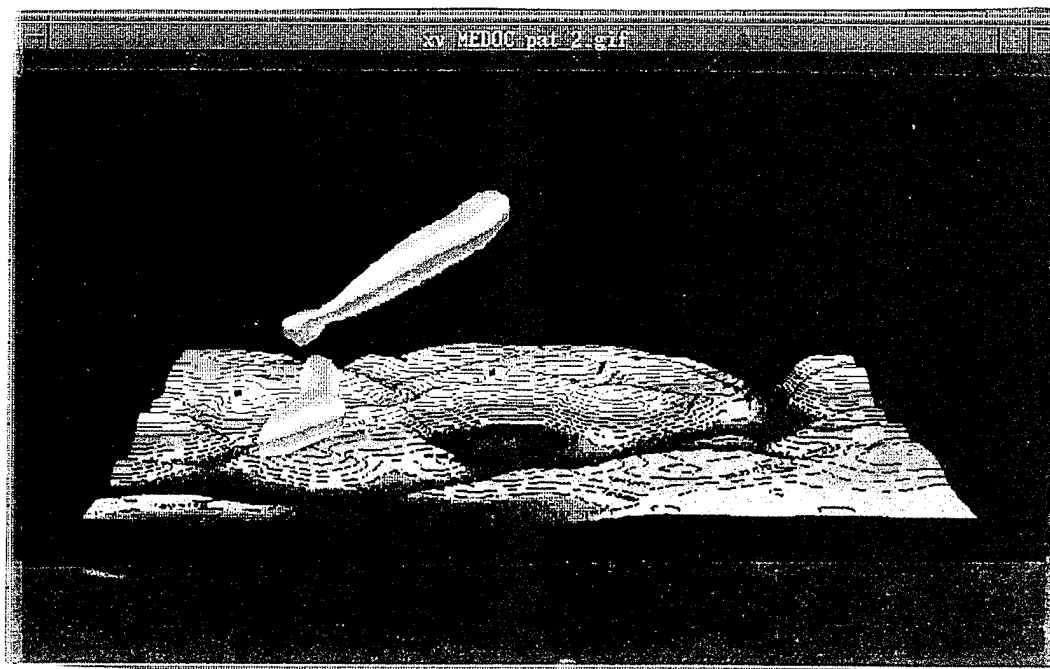


Figure 3-4. Dispersion from atmospheric line source at later time after release (side view).

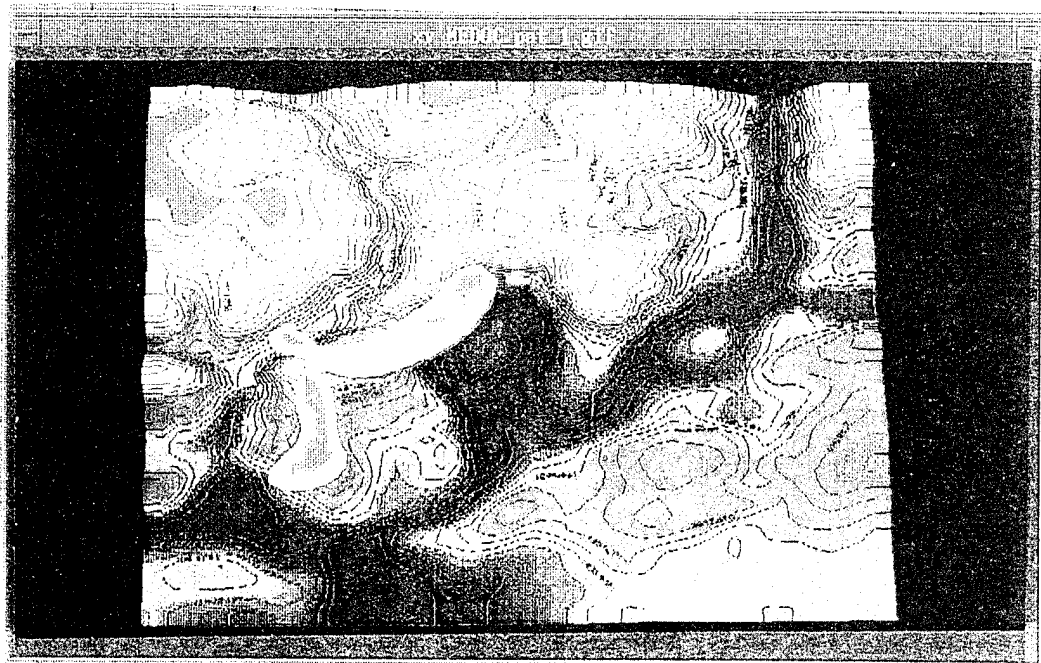


Figure 3-5. Dispersion from atmospheric line source at later time after release (top view).

conditions. To avoid the need for user estimation of stability and specification of α , and to include spatial variations, MEDOC also includes options which internally specify local values of α based on local properties of the atmosphere as well as the topography. While these options were put into place with the original MEDOC development they were not fully operational. In addition more recent developments, in particular those of Moussiopoulos et al, (Reference 13) have added to the understanding and characterization of the relationship of α to the physical properties of the atmosphere and the topography. While conceptually similar to the existing MEDOC options, involving the Strouhal number (or its reciprocal the Froude number) which characterizes the relationship of gravity to inertia forces, the Moussiopoulos formulation provides a different functional dependence of α on the Strouhal number. In addition the required length scale is related differently to the topography.

Under the DNA MEDOC program, the existing MEDOC options for internal determination of α were activated in order to relieve the DNA/DoD user from this responsibility. The primary tasks in this regard required development of valid procedures for obtaining and processing temperature profiles, as well as testing of the resulting options. Also as a new option, the formulation of Moussiopoulos et al. was incorporated into MEDOC. The various stability options available for determination of α are documented in Reference 9 and 10.

3.2.5 Dosage Capability and Casualty Assessment.

The determination of dosages is a multi-faceted procedure, particularly in the case of nuclear sources. First, dosages must be categorized in terms of particular effects on the human body and on specific body organs, e.g., lungs, thyroid, and bone marrow. Effects can be acute (near term) and/or chronic (long term). In addition, each can occur through one or more of many potential pathways, e.g., inhalation, immersion, ground shine, deposition resuspension, food chain, etc. Further complication is added as protective measures might or might not be employed by the exposed population. Finally each hazardous species can have its own effects and pathways. In the case of nuclear sources the number of such species in a single release can easily be in the hundreds.

While MEDOC has the framework for determining dosages for most types of effects and for different pathways, the potential number of such dosage calculations makes full implementation impractical. For the currently available DNA version of MEDOC, the dosage capability has been limited to the overall effects of immersion and deposition/ground shine. All MEDOC transport/dispersion codes, however, do provide time integrated concentrations which act as the basic ingredient and indicator of dosage levels. In the case of nuclear sources, dosages are related to integrated concentrations through dose conversion factors. For the DNA version of MEDOC, does conversion factors have been taken from the Nuclear Regulatory Commission (NRC) code, RASCAL (Radiologic Assessment System for Consequence Analysis) which is described in Reference 14. These factors have been incorporated into MEDOC for immersion and ground shine as noted above, and for alternate sets of nuclear species.

In order to provide a most easily manageable set of species, for which emergency response calculation can be carried out most rapidly, typical species have all been segregated into six basic groups, each with similar properties and effects. These include: noble gases, iodines, cesiums, tellures, strontium, and plutonium. Such groupings are standard and have been found reasonable for nuclear dose calculations. Dose conversion factors have been derived for each group as a weighted average of the constituent species in each group for a typical nuclear release scenario. These have been incorporated into the MEDOC dose calculation routine so as to provide dosages for each of the six basic groups as well as for their summation. In addition to the system of six species groups, an expanded system allowing up to twenty-nine species, plus a thirtieth for summation, has been incorporated into the DNA version of MEDOC. Tests were performed in which dosages from the 6 and 29 species systems were compared. These were found to be in very good agreement, indicating the adequacy of the simplified 6 species system, at least for approximation purposes. Although the DNA MEDOC is currently limited to the 6 and 29 species systems for immersion and ground shine, the procedure can be readily extended to include additional species as well as other effects/pathways.

As a further step in the determination of effects, potential casualties can be estimated from dosages by relating dosage levels to the expected percent of exposed population to be affected.

Such relations have been incorporated into MEDOC, thus allowing percent of population casualties from acute effects to be determined for each ground level grid cell. Given population density maps, expected numbers of casualties could be calculated. This last step has not been carried out as it requires coupling with specific maps of known formats which had not been firmly established at the time of development. As an interim capability, useful for uniform population densities, the amount of area in each dosage band, i.e., percent casualty band, is calculated by MEDOC. Area wide percent of casualties, and therefore total number of casualties, is then determined assuming a uniform population density. Extending this to nonuniform population densities by overlaying population density maps would be straightforward.

3.3 OPERATIONAL ADAPTATIONS.

3.3.1 I/O Interface Streamlining.

There are two distinct methods of input used by the MEDOC codes: preparation of an input data file, and interactive communication with a running program.

Because of its compute-intensive nature, HERMES is usually run as a background (batch-like) process. The user prepares a text-based input file according to the format described in Reference 8. Communication with the executing HERMES is minimal, although the user may view graphically the results of the HERMES calculation while the run is proceeding. This is a familiar mode to users working in the supercomputer environment. For DNA applications, a significantly reduced and reorganized input file structure has been set up. The new file size is on the order of half the original size. This has been accomplished by judiciously setting defaults and simplifying a number of options such as for turbulence where options are numerous and originally intended more for comparative evaluation of turbulence models. Related input variables have been gathered into sections such as: job description, initialization, time and grid management, surface boundary conditions, and concentration related inputs. With the changes

to the input file structure, not only is the input process simplified, but post calculation reference to and interpretation of, input files is more efficient.

The other elements of MEDOC (MINERVE, TRAMES, RELIEF) are run in an Xwindows-based, interactive mode. Each program opens a dialogue window, and the options chosen by the user in the course of the dialogue determine the program flow. Because of the wide-ranging capabilities of MEDOC, the number of possible options which could require a decision from the user currently exceeds 800. While useful in a research mode, this amount of information is prohibitive for practical applications, both in time and in training. However, MEDOC has been structured in a way that permits customization of the I/O interface. All the information concerning a particular option (units, default values, acceptable ranges, even on-line help) are contained in a 'resource file', a text file opened by the program of interest. By modifying the text of the resource file, it is possible to 'mask' an option, setting it to a default value and removing it from the user's view, all without requiring a change to the source code. In addition, since all resource files are kept in a single directory whose name is made available to the program, multiple directories of resource files can be created, each with custom values for defaults, masked options, even languages.

The DNA version of MEDOC contains a directory of resource files (/ADSO/DIALOG/DNA) with options set specifically for the problems likely to be addressed by the DNA user. Other input parameters have values calculated internally in order to minimize the amount of input required from the user. For example, the vertical height of the computational grid for MINERVE is computed internally based on the maximum elevation in the domain. Also, the computational time step in TRAMES is automatically calculated to provide maximum trajectory coverage of the domain without violating the Courant condition. In addition to these adaptations, text 'help' files have been created(/ADSO/SAIC/*.hlp). These files can be viewed in a window adjoining the window opened by the MEDOC element of interest; they provide further explanation of that element's options.

3.3.2 TOPOREL - Topography Data Handling.

As discussed in Section 2.1, the MEDOC routine TOPOREL was developed to provide the conversion from the format of DNA's terrain elevation data (DMA DTED data extracted with DNA Reader) to MEDOC's Primary DTM (Digital Terrain Model).

TOPOREL accepts DTED elevation data in latitude-longitude coordinates over square regions from one to five degrees. The corners of the latitude-longitude space are converted to UTM (Universal Transverse Mercator) coordinates and displayed to the user. The user is then prompted for the location of the southwest corner of the rectangular UTM grid defining the Primary DTM, as well as the number of grid points in the west-east and south-north directions, and the distance in meters between grid points.

TOPOREL converts each grid point from UTM to latitude-longitude and performs a bilinear interpolation in the DTED latitude-longitude space to obtain elevation values at the UTM grid points.

Although TOPOREL was developed to process DTED data, it is easily applicable to any terrain elevation data which is equally spaced in latitude-longitude space.

3.3.3 HERMIN - Gridded Met Data Inputs.

The MEDOC mass consistency model MINERVE requires meteorological input data which are usually obtained from weather observation stations or from climatological data. However, for some DNA applications, it is necessary to provide gridded data from a forecast model as the met input to MINERVE. HERMIN was developed to combine the nesting capability of HERMES with the computational efficiency of MINERVE. A preprocessor created specifically for the forecast model of interest (for example, COMASS created for MASS - Reference 1) converts the gridded met data to the standard MEDOC binary format. In addition to the creation of proper formats, COMASS also performs transformations of physical variables such as from

reduced pressure coordinates to geopotential as might be required by MEDOC. The resulting MEDOC binary file is then read by HERMIN which initializes the computational grid using the same nesting procedures as HERMES. HERMIN then calculates a mass consistent wind field using the same procedures as MINERVE. The output wind field can then be used to drive either of MEDOC's transport/diffusion models, or to provide high resolution wind fields for other purposes, including other dispersion codes. In this regard it is noted that MINERVE outputs have been coupled with the SCIPUFF dispersion code (Reference 15) which is also used by DNA.

While the above developments were aimed at the coupling of MINERVE with larger scale gridded met fields, it is noted that they also accommodate HERMES. In particular, the COMASS preprocessor provides files which can be used to drive HERMES in a nesting mode for finer resolution calculations.

SECTION 4

MEDOC DEMONSTRATIONS/VALIDATIONS

4.1 VALIDATION HISTORY AND RELATED EFFORTS.

As a mature operational capability, the MEDOC codes had been extensively validated prior to their application to DNA problems. Further, as the codes continue to be used by their original developers (the French Electricity Board - EDF) they are the subject of ongoing periodic testing and validation. The original validations were performed against field experiments conducted at French nuclear power plant sites. These covered a variety of terrain types from flat to very mountainous, both with and without proximity to the sea. Tests were carried out against weather station data and tracer concentrations in order to validate the meteorological as well as material transport components of MEDOC.

Experimental tests/data used in the early validation work included the following carried out at French power plant sites:

CREYS (June 1985) - 5 weeks field experiment, 10 SF6 tracer experiments (42 sampling units), 1 radiosounding unit, 13 ground meteorological stations, 2 sodars, 1 experimental aircraft.

CHOOZ (June 1986) - 4 weeks field experiment, aimed at MINERVE validation. No tracer experiments (objective limited to winds validation), 1 radiosounding unit, 15 ground meteorological stations, 3 sodars.

PENLY (September 1986) - 5 weeks field experiments, 10 SF6 tracer experiments (44 sampling units), 1 radiosounding unit, 10 ground meteorological stations, 1 sodar, 1 met tower. Dispersion validations at a site along the French Atlantic coast.

Results of these experiments are documented in internal EDF reports.

After the above initial experiments, two longer term experimental systems were installed for validation purposes: one in the Rhone Valley (CRUAS) and one in the Loire Valley (CHINON). The experiments in the Rhone Valley were aimed mainly at regional scale validations of meteorology calculations with HERMES in a complex terrain environment. HERMES was run primarily in a forecast mode with nesting into the larger scale French Meteorological Office model (PERIDOT). Data included French Met Office measurements along with EDF sodar data. Results showed that deviations between calculated and measured data, primarily for wind direction and temperature, were significantly less for HERMES than for PERIDOT. This basically was a consequence of complex topography which was more accurately accounted for by HERMES. Also, time lag errors for wind direction forecast by PERIDOT were greatly reduced with HERMES. Details of the Rhone Valley validations are presented in Reference 16. Similar validations were performed for the Loire Valley experiments where results were also good but less interesting as they involved a basically flat terrain.

For validations of MINERVE, the Italian Electricity Board (ENEL) has performed systematic comparisons against wind tunnel data as well as against other models including the MATHEW (ARAC) mass consistency model. Results of these tests are presented in Reference 17. The wind tunnel data was obtained from the US EPA RUSHIL experiment (Reference 18) which involved planar (two dimensional) hills of analytical shape and varying slope. This included one hill of sufficient height to cause reversed flow in the lee side region, and constitutes a very challenging case to model. As the wind tunnel data were very detailed, extensive testing of MINERVE (and MATHEW) was possible in which the models were driven with different numbers of available profiles and then tested with the unused data. Tests included cases where only a single profile along with a few near surface measurements were used, as might be encountered in practical applications with field data. As a general conclusion in Reference 17, it was found that "All the considered models show an ability to describe the flow with errors confined within the reasonable limit of 20% (excluding the wake region) and can therefore be considered suitable for practical applications." Regarding the wake region, in the most extreme

case (highest hill) involving reversed flow (a recirculation region), both mass consistency models accurately simulated the height of the measured line of reversal of the horizontal wind component when all available data (15 profiles) were used to drive the models. However "for simulations based on 4 profiles only, MINERVE remains not far from reality", while "the recirculation is exaggerated by MATHEW". In less demanding flow regimes it was found for tests using only one vertical profile along with several near ground measurements that, "the results of this 'atmospheric-like' simulation show small differences when compared to those obtained starting from three profiles and reveal limited errors; thus they can be considered encouraging for practical applications".

In addition to the above, a number of other validation studies have been carried out with the MEDOC codes. These have involved sulfur dioxide (SO_2) concentrations from industrial sources in the vicinity of LeHavre, France, hydrogen sulfide (H_2S) from geothermal sources in Larderello, Italy, and sulfur hexafluoride (SF_6) experiments in the Swiss Alps. The last of these is most interesting as it involved detailed tracer measurements in a highly complex terrain, with model validations being performed independently by Swiss investigators for numerous models in addition to MEDOC. For these reasons the Swiss case is discussed separately in Section 4.4 of this report.

4.2 ANALYTICAL VALIDATIONS - STABILITY/TURBULENCE, DECAY, AND EVAPORATION.

As a supplement to the code-to-data validations, a number of calculations were carried out for validation against exact/analytic solutions in cases where they were known. This was done primarily for HERMES since it involves complex numerical solution; therefore it is important to assess and characterize the numerical accuracy. With models such as TRAMES, which are based on analytic formulations, such evaluations are of less concern because accuracy is directly related to the quality/validity of the correlations.

Since the governing equation for transport and diffusion of a passive scalar quantity is relatively complex, exact solutions are known only for simplified conditions. These include a flat terrain in which the wind and turbulence fields are uniform. For such a case in which a source of strength Q is emitting continuously from a point at height H , the steady state solution for concentration at downwind (crosswind) distance X (Y) and height Z above ground is given by the relationship:

$$C = \frac{Q}{4\pi X \sqrt{K_v K_h}} \exp \left(\frac{-Y^2}{4X K_h / U} \right) \left[\exp \left(\frac{-(Z-H)^2}{4X K_v / U} \right) + \exp \left(\frac{-(Z+H)^2}{4X K_v / U} \right) \right] \quad (4.1)$$

where U represents the constant uniform wind field with K_v and K_h representing the uniform values of the vertical and horizontal diffusivities, respectively. The above equation applies to inert, non-decaying, species with an impervious perfectly reflecting ground surface. For the case of a decaying species in which the local decay rate is linearly proportional to the concentration, the governing equation for species transport and diffusion is modified by inclusion of a sink term involving the first power of concentration. This results in a modification of the solution which then requires multiplication of equation (4-1) by an exponential decay term dependent on the species half-life and the transport time (X/U).

HERMES was exercised for various cases involving the assumptions associated with the above solution. Sample results are shown in Figure 4-1 for two sources each emitting continuously at a rate of one gram/second, one with a decaying species of 34 minute half-life and the other with a non-decaying species. Concentration contours are shown in a horizontal plane at the release height of 100 meters. Winds were assumed constant at 4 meters/second from left to right while the turbulent diffusivities were taken as 120 meters²/second and 52 meter²/second in the horizontal and vertical directions, respectively. These turbulent diffusivities are representative of an unstable atmosphere.

For comparison of HERMES calculations, such as those in Figure 4-1, with the exact solution, plume widths for various concentration levels were determined at a number of

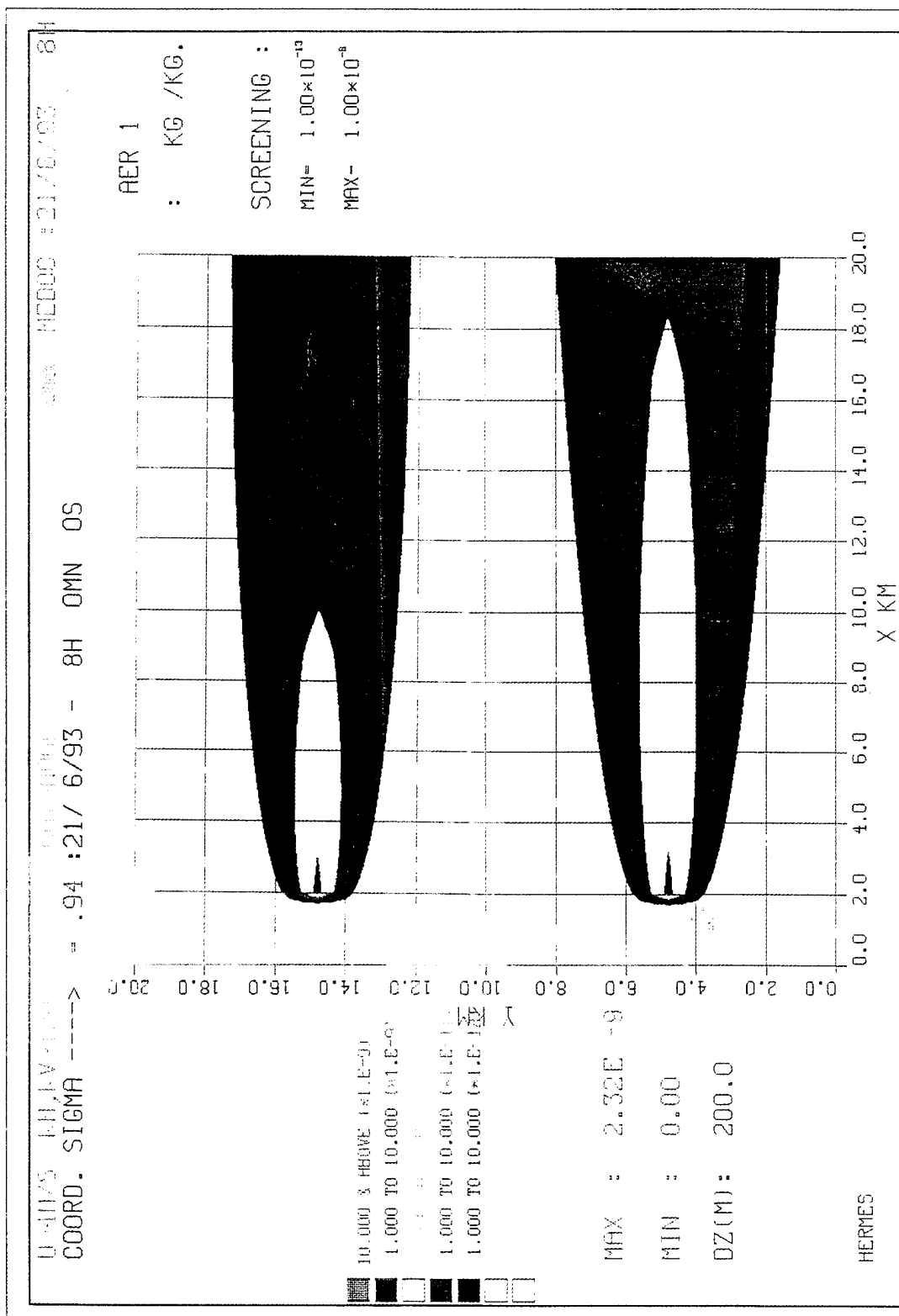


Figure 4-1. HERMES concentration profiles with and without decay in uniform wind and turbulence fields.

downwind distances. From the exact solution, equation 4-1, the plume width at the height of release is determined to be:

$$W = 4 \sqrt{\frac{K_H}{U} X \ln \left[\frac{Q/C}{4 \pi X \sqrt{K_V K_H}} \left[1 + \exp \left(\frac{-H^2}{X K_V / U} \right) \right] \right]} \quad (4-2)$$

For the non-decaying case illustrated in Figure 4-1, a comparison of plume widths for contour levels 10^{-10} , 10^{-11} , and 10^{-12} KG/KG from the HERMES calculations, versus those determined by the exact equation (4-2) is given in Table 4-1. Except for some deterioration of the HERMES solution at the lower contour levels, particularly (10^{-12}), HERMES is seen to be in excellent agreement with the exact solution. The error at the 10^{-12} contour is not considered numerically significant as it is at a level 3 orders of magnitude below the peak concentration values. These comparative results are illustrated graphically in Figure 4-2. To further display the accuracy of the HERMES solution, direct comparisons with concentrations from the exact solution are shown graphically in Figures 4-3 and 4-4 for axial and crosswind profiles, respectively. Crosswind profiles include both the horizontal and vertical directions. As seen, the HERMES and exact solutions are practically indistinguishable for both the axial and crosswind distributions.

As a test of the species decay capability incorporated into HERMES, the ratio of concentrations from the HERMES solutions of Figure 4-1 with and without decay were compared with the ratio of exact solutions with and without decay, i.e., compared with the exponential multiplicative factor using a 34 minute half-life. Comparisons were performed at various downwind and crosswind distances. Results are given in Table 4-2. The HERMES prediction including species decay is seen to be in excellent agreement with the exact solution.

For further validation, similar HERMES calculations and comparisons were carried out for non-decaying species of the same source strength (1 gm/sec), in atmospheres of different stabilities/turbulence levels. For simulation of an approximately neutral atmosphere, horizontal and vertical diffusivities of 64 meters²/sec and 4.8 meter²/sec, respectively, were assumed.

Table 4-1. Plume contour widths for an unstable atmosphere.

HERMES vs. ANALYTICAL PLUME WIDTHS
(Unstable Conditions: $KH = 120 \text{ M}^2/\text{S}$, $KV = 52 \text{ M}^2/\text{S}$)

Contour (KG/KG)	Solution Method	Plume Widths (KM) @ Downwind Distance (KM) =				
		2	4	8	12	16
1.00E-12	HERMES*	3.2	3.8	4.8	5.5	6.1
"	Analytic	2.51	3.37	4.50	5.31	5.95
1.00E-11	HERMES*	2.4	2.8	3.5	4.0	4.3
"	Analytic	2.02	2.64	3.38	3.86	4.21
1.00E-10	HERMES*	1.4	1.6	1.6	1.3	0.2
"	Analytic	1.36	1.59	1.61	1.28	0.17

*400 M Grid

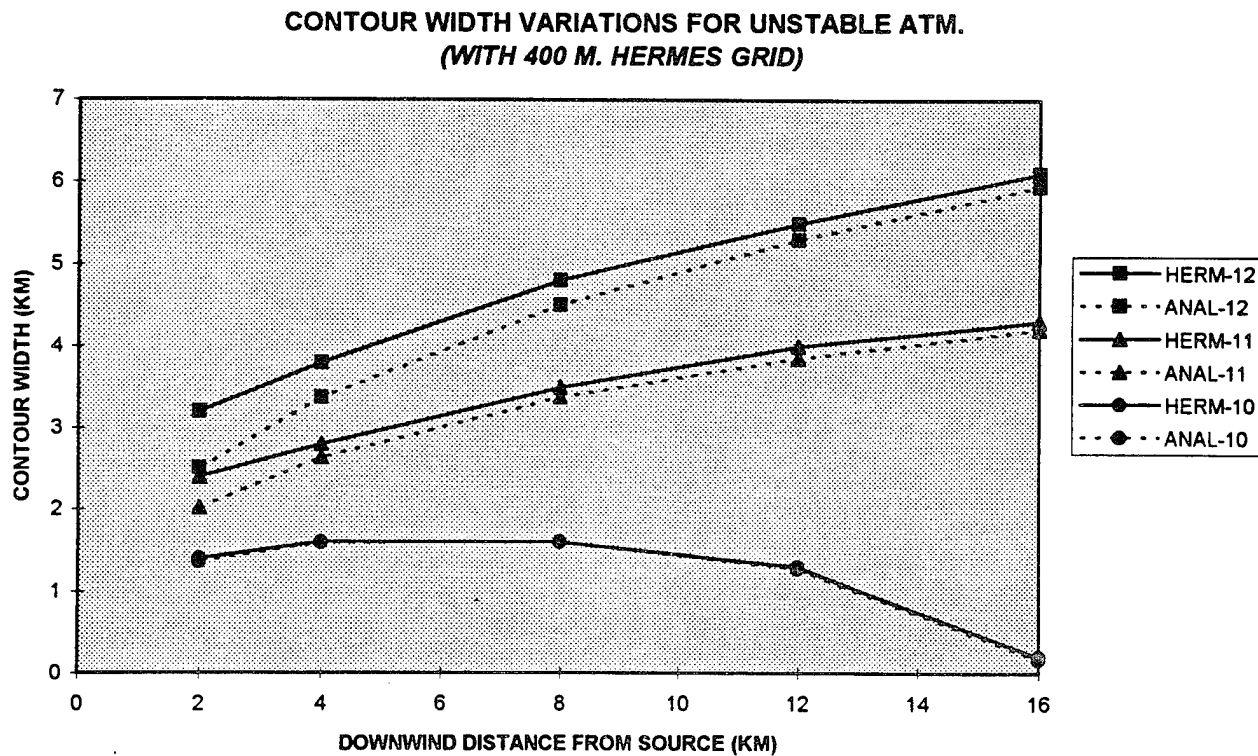


Figure 4-2. Contour width variations from HERMES calculation and analytic solution for unstable atmosphere.

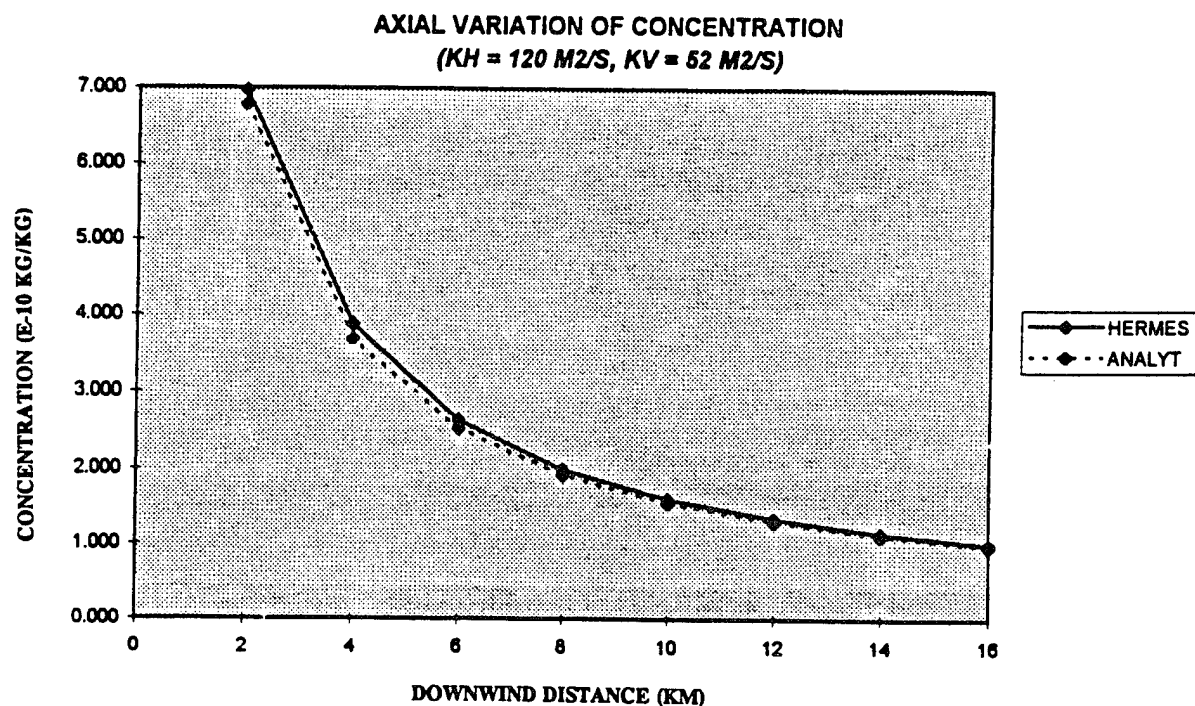


Figure 4-3. Axial variation of concentration from HERMES calculation and analytic solution for an unstable atmosphere.

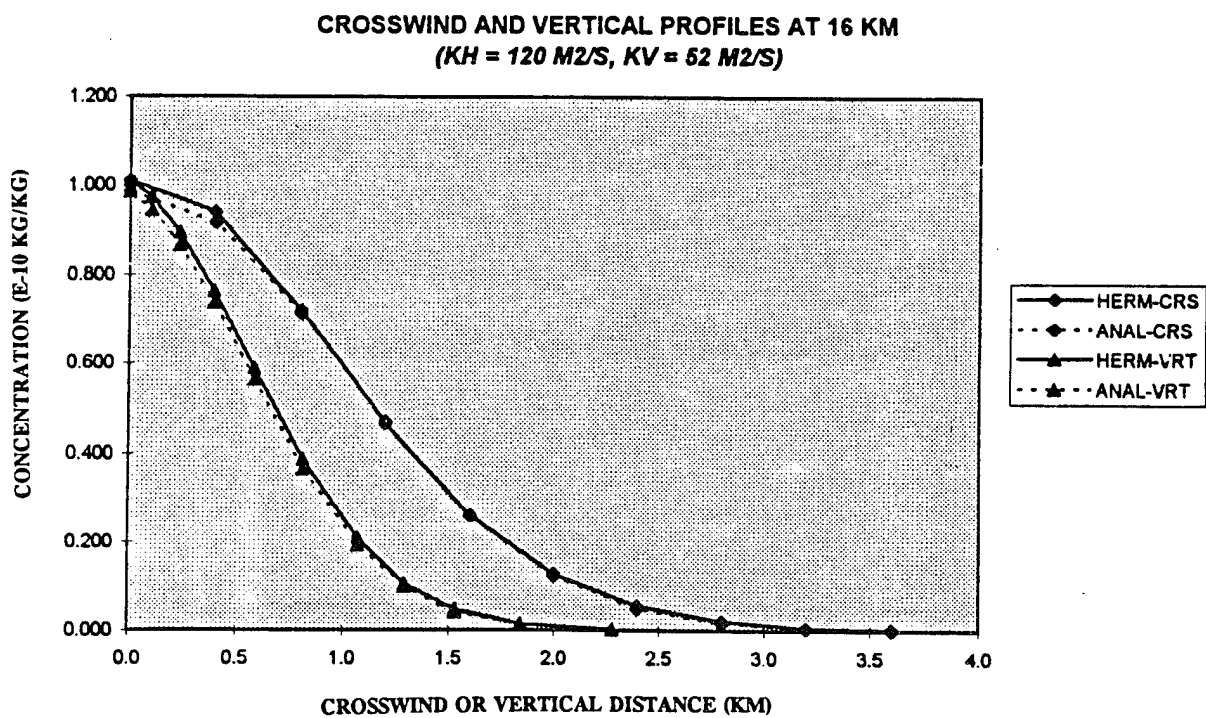


Figure 4-4. Crosswind and vertical profiles of concentration from HERMES calculation and analytic solution for an unstable atmosphere.

Table 4.2. Decay Fraction Comparisons.

HERMES vs. ANALYTICAL DECAY FRACTIONS*
 (Unstable Conditions: $KH = 120 \text{ M}^2/\text{S}$, $KV = 52 \text{ M}^2/\text{S}$)

Off-Axis Distance (KM)	Solution Method	Decay Fractions @ Downwind Distance (KM) =				
		2	4	8	12	16
0	HERMES	.820	.692	.492	.351	.250
	Analytic	.844	.712	.507	.361	.257
1	HERMES			.488		.248
	Analytic			.507		.257
2	HERMES			.488		.247
	Analytic			.507		.257

*Ratio of solutions with and without decay.

Plume width values are shown for comparison in Table 4-3, with the results shown graphically in Figure 4-5. Again the HERMES prediction is in very good agreement with the exact solution for the higher concentration contours. As for the unstable case, HERMES overestimates the contour width for the lowest contour value (10^{-12}). Though the disagreement has increased in comparison with the unstable case, it is still considered numerically insignificant, as it again applies to a contour which is three orders of magnitude below peak values, and therefore well below typical meteorological uncertainties.

Finally, HERMES was exercised for a case corresponding to a stable atmosphere, with horizontal and vertical diffusivities of 36 meters²/second and 1.1 meters²/second, respectively. Plume width values calculated with HERMES and analytically are given in Table 4-4 with graphical results displayed in Figure 4-6. Comparisons in this case show significant deterioration of the HERMES solution, not only for the lowest contour level (10^{-12}), but also for the intermediate level (10^{-11}) and, close to the source, for the highest (10^{-10}) level. For this HERMES calculation, as well as all those discussed above, a horizontal grid point spacing of 400 meters was used. While this grid point resolution was found sufficient for neutral and unstable atmospheric conditions, the stable case involves reduced spreading and narrower plumes, particularly near to the source, which apparently requires greater grid resolution. To demonstrate this, HERMES was rerun with a 200 meter grid spacing. The numerical and graphical results in this case are presented in Table 4-5 and Figure 4-7, respectively. With the finer grid resolution, the HERMES solution is seen to be clearly improved, now having accuracy comparable with that for the neutral stability case. In summary, HERMES has been demonstrated to give excellent accuracy based on exact analytic solutions. Care must be exercised, however, to employ adequate grid resolution, particularly for reduced turbulence levels/stable atmospheres.

Table 4-3. Plume contour widths for a neutral atmosphere.

HERMES vs. ANALYTICAL PLUME WIDTHS
(Unstable Conditions: KH = 64 M²/S, KV = 4.8 M²/S)

Contour (KG/KG)	Solution Method	Plume Widths (KM) @ Downwind Distance (KM) =				
		2	4	8	12	16
1.00E-12	HERMES*	2.8	3.3	4.2	4.8	5.3
"	Analytic	1.96	2.67	3.63	4.34	4.92
1.00E-11	HERMES*	1.8	2.5	3.2	3.6	4.0
"	Analytic	1.64	2.18	2.91	3.43	3.84
1.00E-10	HERMES*	1.4	1.7	2.0	2.3	2.4
"	Analytic	1.23	1.55	1.94	2.17	2.31

*400 M Grid

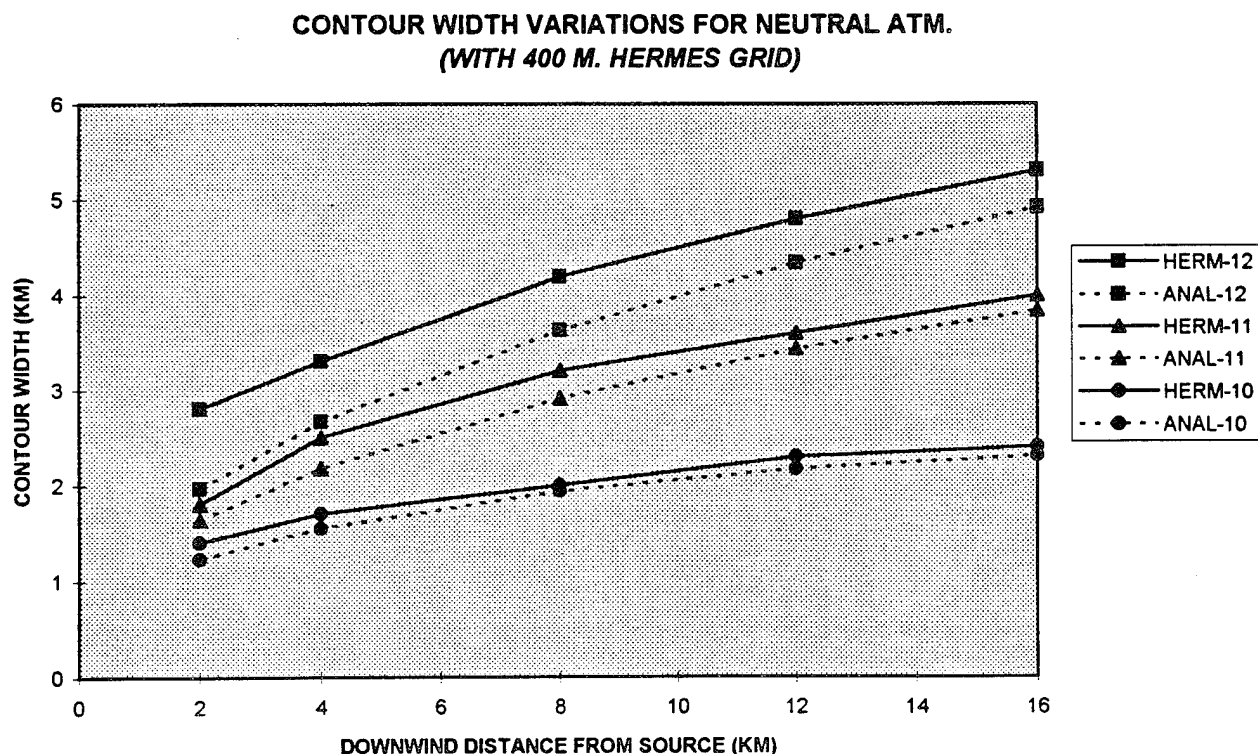


Figure 4-5. Contour width variations from HERMES calculation and analytic solution for a neutral atmosphere.

Table 4-4. Plume contour widths for a stable atmosphere (400 M HERMES grid).

HERMES vs. ANALYTICAL PLUME WIDTHS
(Stable Conditions: $KH = 36 \text{ M}^2/\text{S}$, $KV = 1.1 \text{ M}^2/\text{S}$)

Contour (KG/KG)	Solution Method	Plume Widths (KM) @ Downwind Distance (KM) =			
		2	4	8	12
1.00E-12	HERMES*	2.5	2.9	3.5	4.0
"	Analytic	1.57	2.13	2.87	3.43
1.00E-11	HERMES*	1.7	2.3	2.8	3.1
"	Analytic	1.34	1.79	2.37	2.79
1.00E-10	HERMES*	1.4	1.6	1.8	2.0
"	Analytic	1.07	1.37	1.72	1.95

*400 M Grid

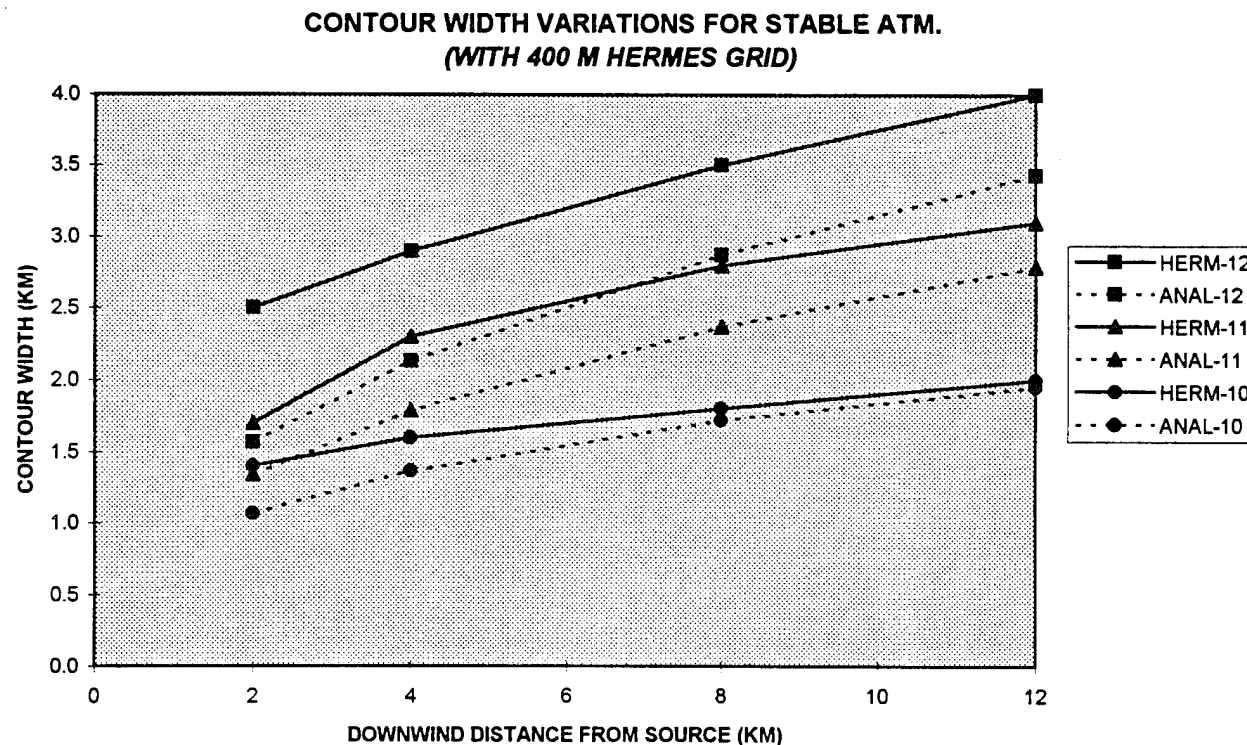


Figure 4-6. Contour width variations from HERMES calculation (400 m grid) and analytic solution for a stable atmosphere.

Table 4-5. Plume contour widths for a stable atmosphere (200 M HERMES grid).

HERMES vs. ANALYTICAL PLUME WIDTHS
(Stable Conditions: $KH = 36 \text{ M}^2/\text{S}$, $KV = 1.1 \text{ M}^2/\text{S}$)

Contour (KG/KG)	Solution Method	Plume Widths (KM) @ Downwind Distance (KM) =			
		2	4	8	12
1.00E-12	HERMES*	2.0	2.4	3.1	3.6
"	Analytic	1.57	2.13	2.87	3.43
1.00E-11	HERMES*	1.6	1.9	2.5	2.9
"	Analytic	1.34	1.79	2.37	2.79
1.00E-10	HERMES*	1.2	1.4	1.8	2.0
"	Analytic	1.07	1.37	1.72	1.95

*200 M Grid

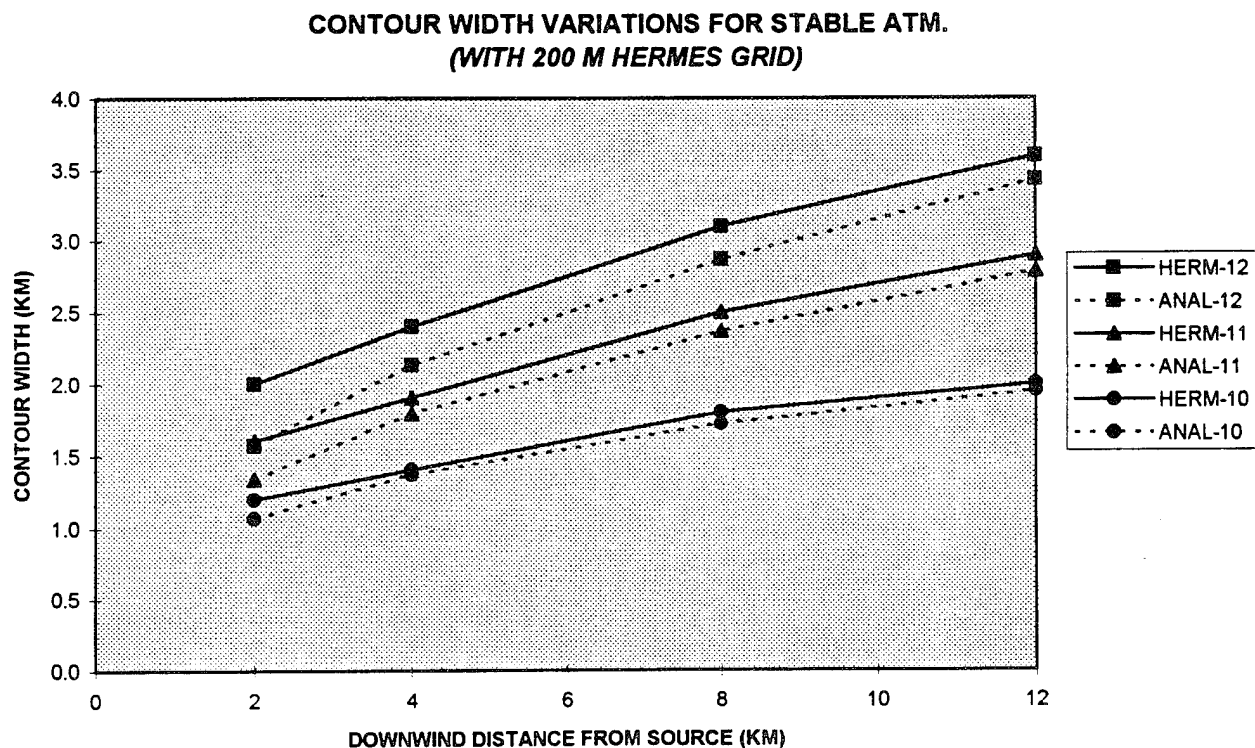


Figure 4-7. Contour width variations from HERMES calculation (200 M grid) and analytic solution for a stable atmosphere.

4.3 SEA BREEZE DEMONSTRATION - GROUND/ATMOSPHERE INTERACTION EFFECTS.

Because sea breeze conditions are potentially of interest in DNA applications, special effort was directed at demonstrating the applicability of HERMES in such cases. As sea breezes are essentially driven by differential heating/temperatures between adjacent land and sea surfaces, HERMES allows two primary methods of simulating such conditions. The first, more simple and direct, approach is to select one of several available periodic forcing functions for ground and sea temperatures. This boundary condition with the HERMES physics generates the corresponding sea breeze conditions. This approach is appropriate when diurnal surface temperature variations are reasonably well known, and was found to give realistic sea breeze flow in sample calculations for the South Korean coast.

As a more fundamental approach, particularly appropriate for sea breeze phenomena, HERMES also includes the option to determine surface temperatures via the Deardorff Two Reservoir Model (Reference 4). In this way the surface temperature is calculated as an interface condition between the atmosphere and the subsurface or ground (rather than specified as a boundary condition). The ground is described as two layers or reservoirs of user specified thicknesses, moisture content, thermal and hydrologic properties. Hydrological and thermal balances imposed between ground and atmosphere, along with appropriate solar conditions, then determine surface temperature. The Deardorff model is run in a coupled mode along with the HERMES meteorological model.

As a test of this capability, the South Korea sea coast region was again evaluated. Relatively calm, light southerly winds were assumed for initial morning conditions as displayed in Figure 4-8. The land mass was assumed to be "coarse earth" with corresponding material and thermal properties. To accentuate land mass heating and sea breeze flow, minimal ground water content was assumed along with zero cloud cover. A typical morning sounding was taken for the initial temperature profile at 8AM local time. As shown in Figure 4-9, this provides initial land

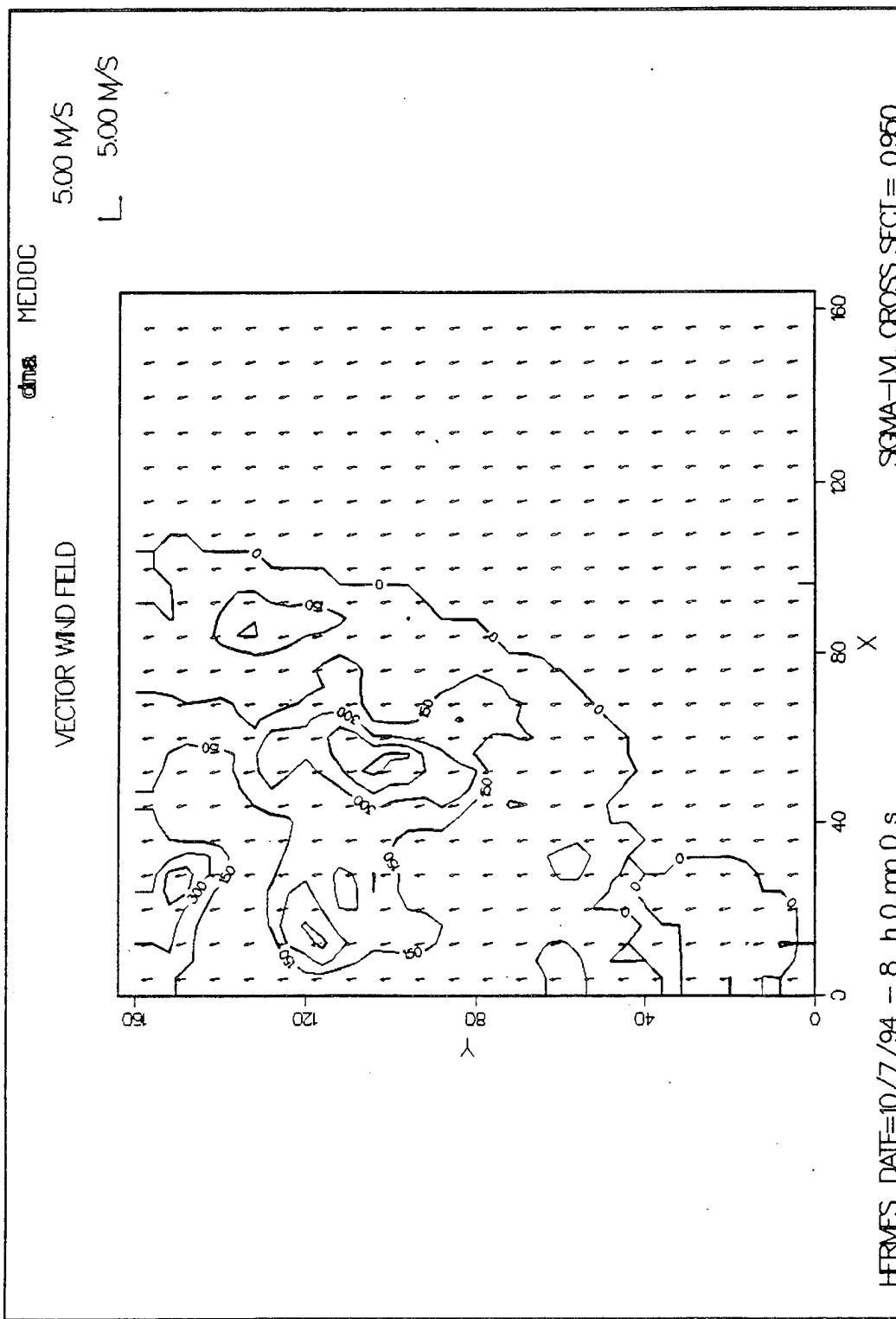


Figure 4-8. Initial wind field for HERMES sea breeze calculation.

temperatures that are equal to or, for high elevations, less than the sea temperature. HERMES was then applied in the Deardorff mode over the next sixteen hour period.

Sample results are given in Figures 4-10 to 4-13. The calculated afternoon (4 PM) and nighttime (midnight) surface temperatures are displayed in Figures 4-10 and 4-11, respectively. As opposed to the initial surface temperatures (Figure 4-9), the afternoon land temperatures are now warmer than the sea temperature, with the differential in most land areas ranging from 6 to 10 degrees. Because of topographical effects however, differentials at the higher elevations are seen to be somewhat less (2 to 6 degrees), while those in the lower valley areas are hotter (10 to 13.7 degrees). Subsequently, nocturnal radiative cooling, particularly strong with the assumed dry cloudless conditions, drives the land surface to temperatures below those of the sea surface, as shown in Figure 4-11. Again this is seen to be most pronounced at the higher elevations.

To illustrate the associated sea breeze conditions, Figures 4-12 and 4-13 show vertical, west to east, slices (at $Y = 80$ KM) of the wind field at the initial (8AM) and afternoon (4PM) times respectively. Starting from the near calm winds in the morning a well defined sea breeze circulation is seen to have developed in the afternoon. It might also be noted in Figure 4-13 that particularly strong updrafts are generated in the region approximately 30KM from the western boundary. Reference to Figure 4-10 shows this region ($Y = 80$ KM and $X = 20$ to 40 KM) to possess especially high ground temperatures as a result of its low elevation inland topography. While the updrafts in this region are strong, it should be pointed out that they are *graphically exaggerated by differences between the vertical and horizontal scaling of both spatial distances and velocity vectors*. This demonstrates that HERMES possesses the necessary capabilities for simulation of sea breeze conditions.

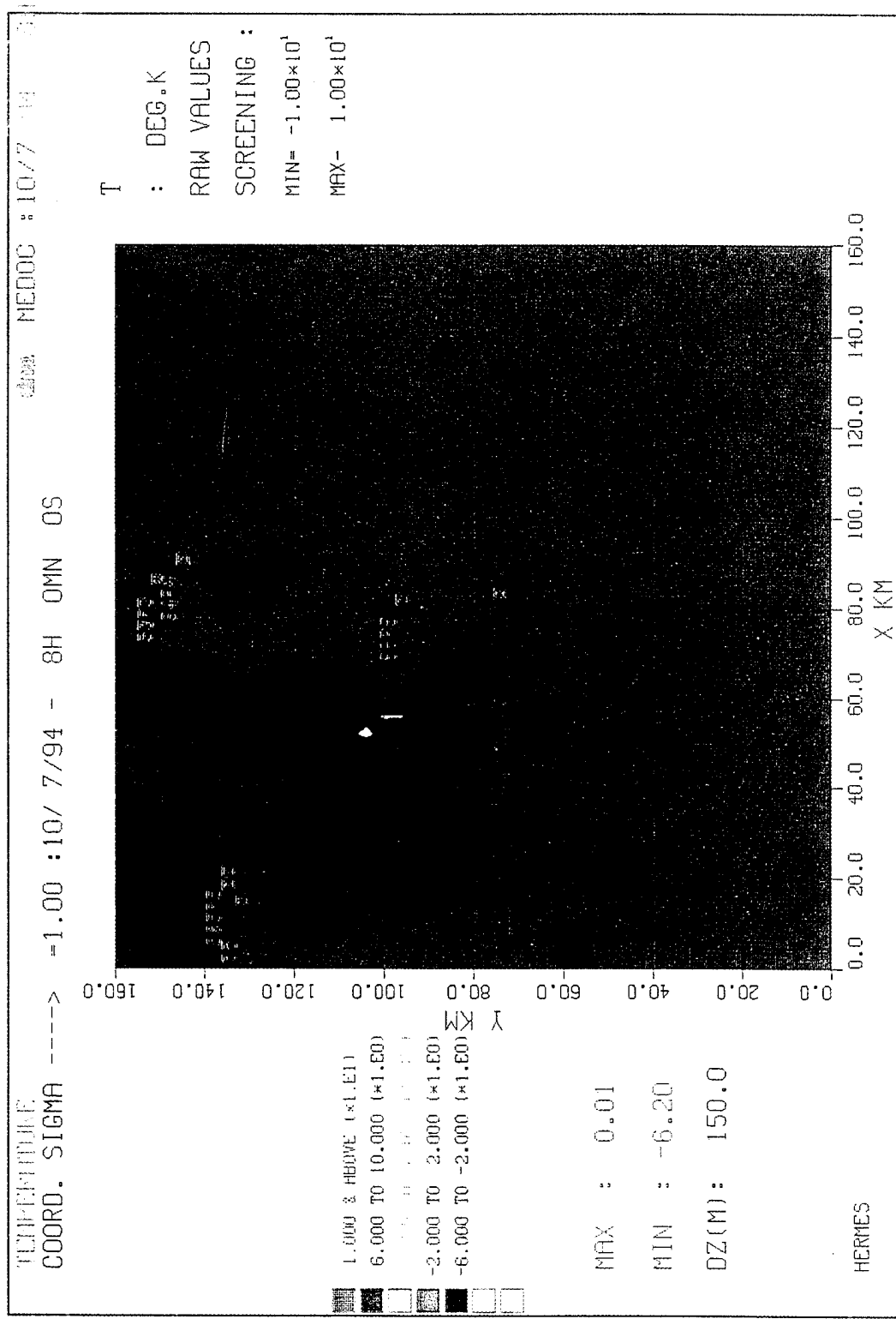


Figure 4-9. Initial land and sea surface temperature for HERMES sea breeze calculation.
(Temperatures shown as differentials relative to sea surface temperature.)

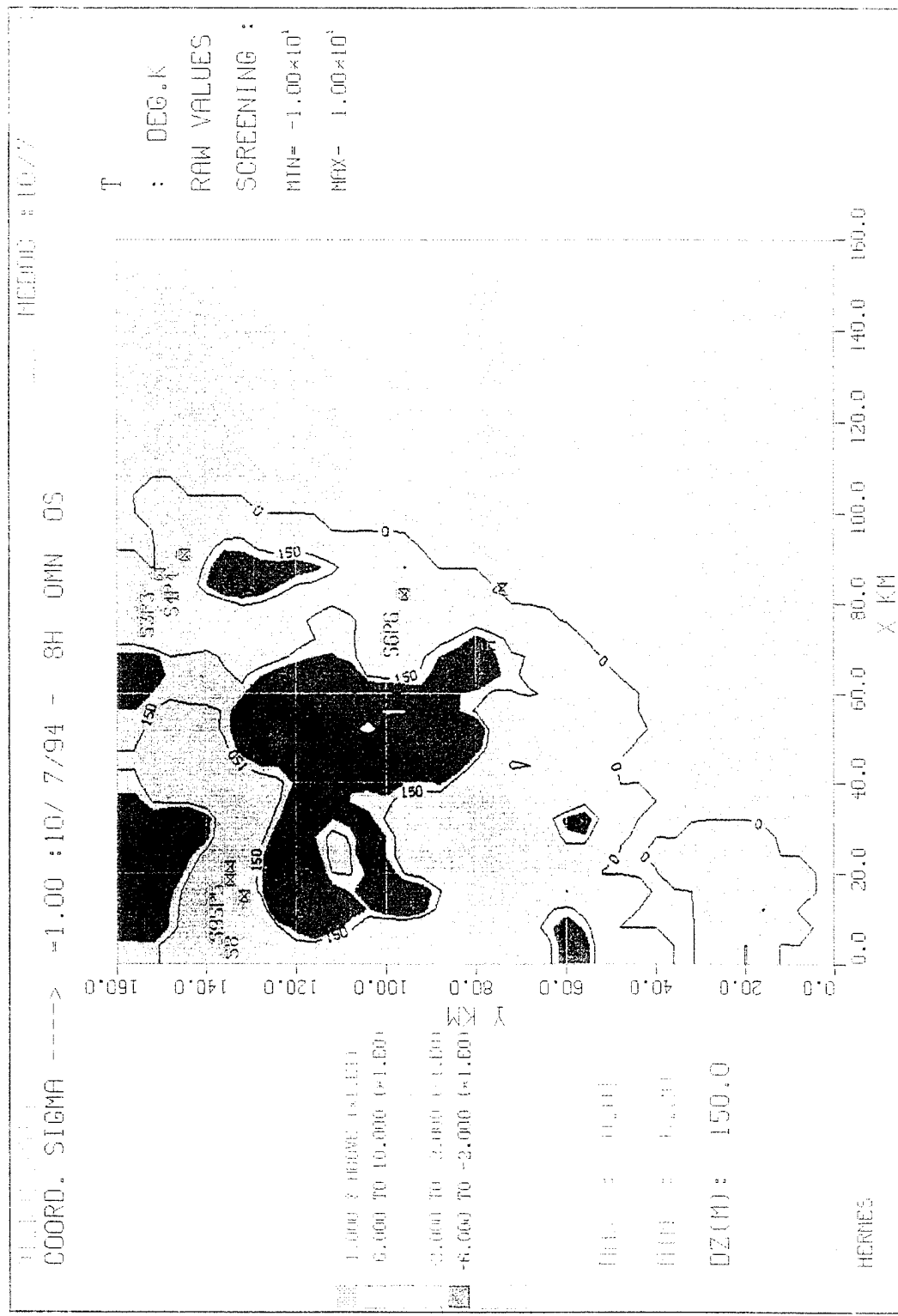


Figure 4-9. Initial land and sea surface temperature for HERMITS sea breeze calculation. (Temperatures shown as differentials relative to sea surface temperature.)

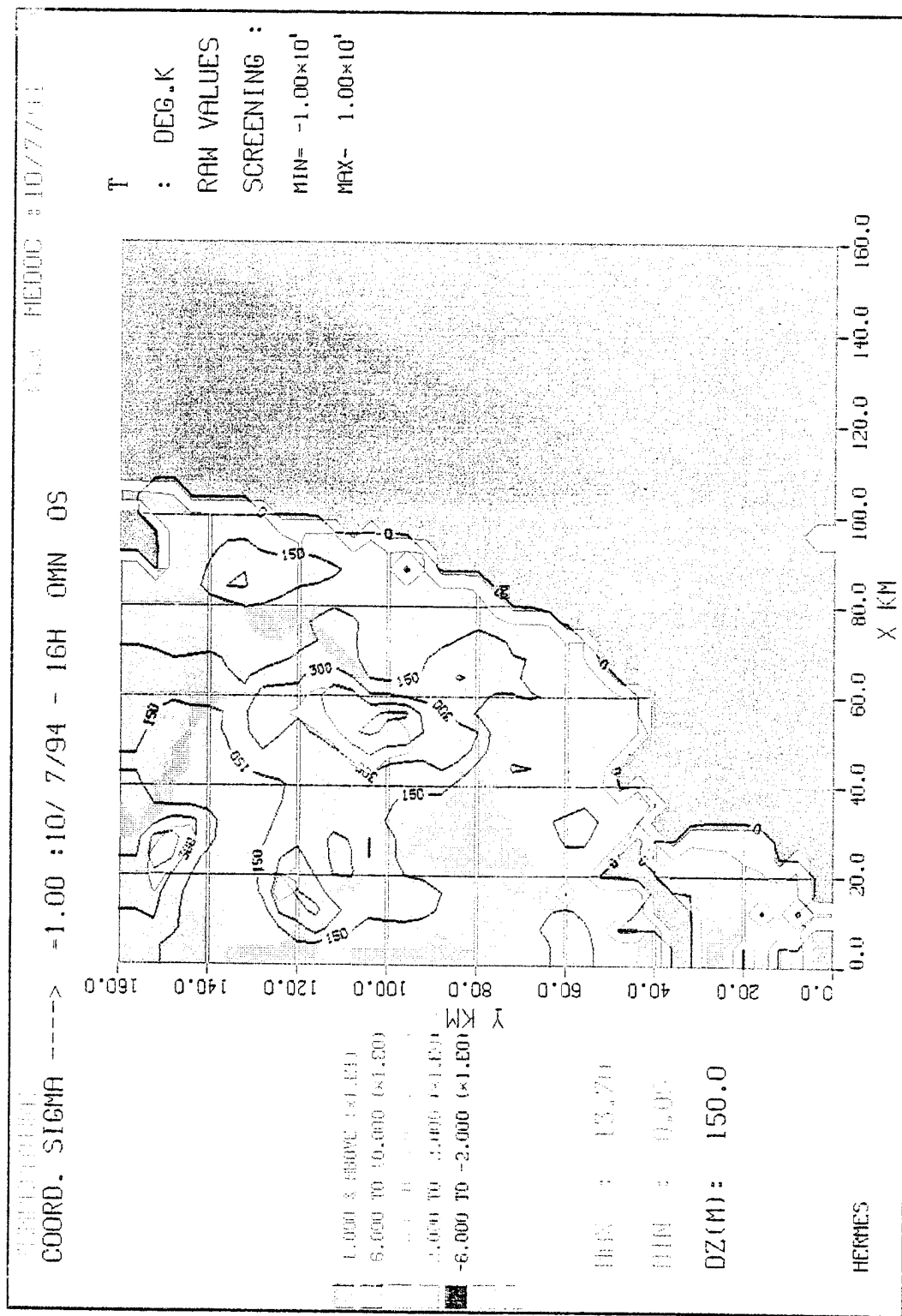


Figure 4-10. Mid-day land and sea surface temperatures from HERMES sea breeze calculation. (Temperatures shown as differentials relative to sea surface temperature.)

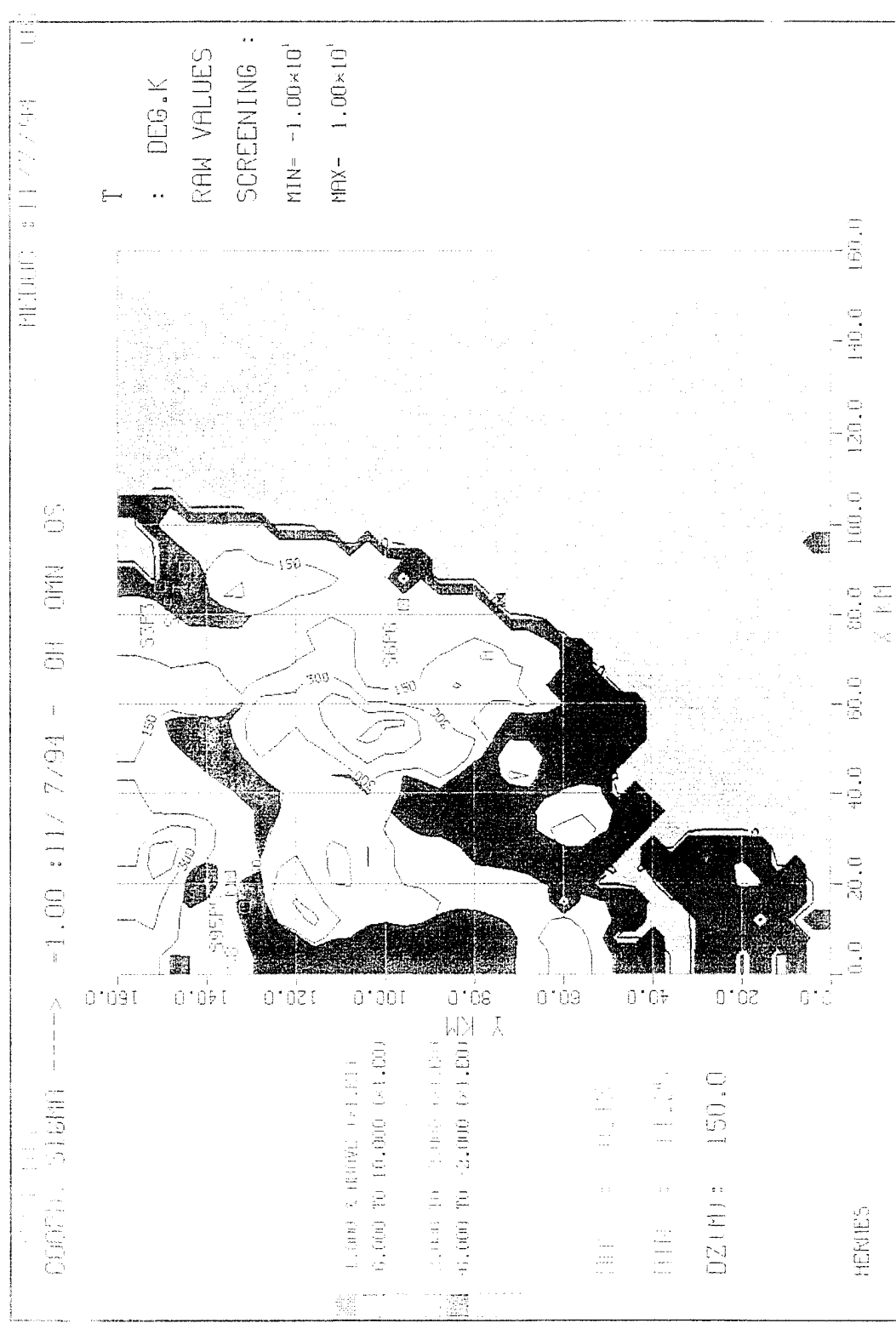


Figure 4-11. Midnight land and sea surface temperatures from HERMES sea breeze calculation. (Temperature shown as differentials relative to sea surface temperature.)

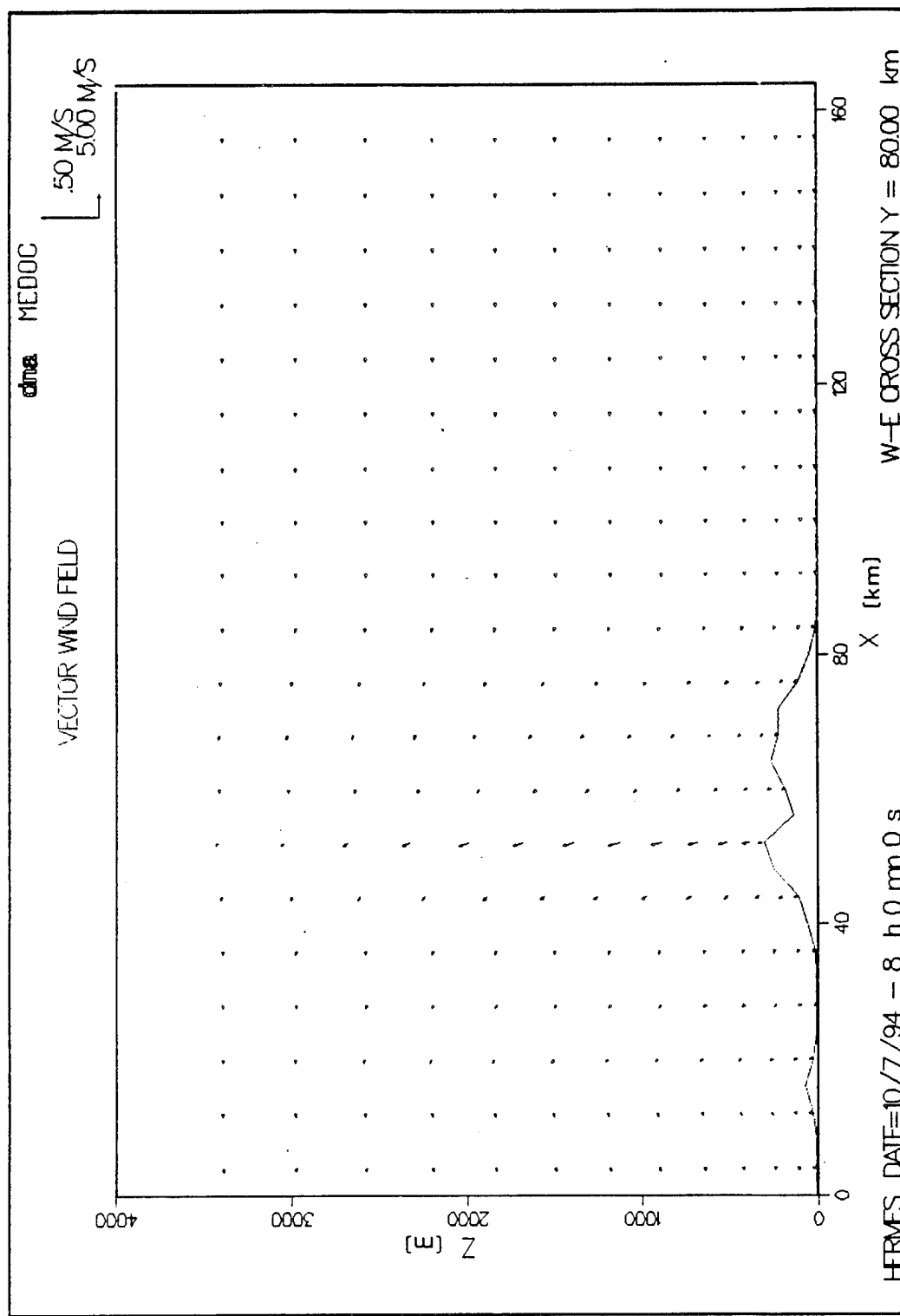


Figure 4-12. Wind profile in a vertical plane at initiation of HERMES sea breeze calculation.

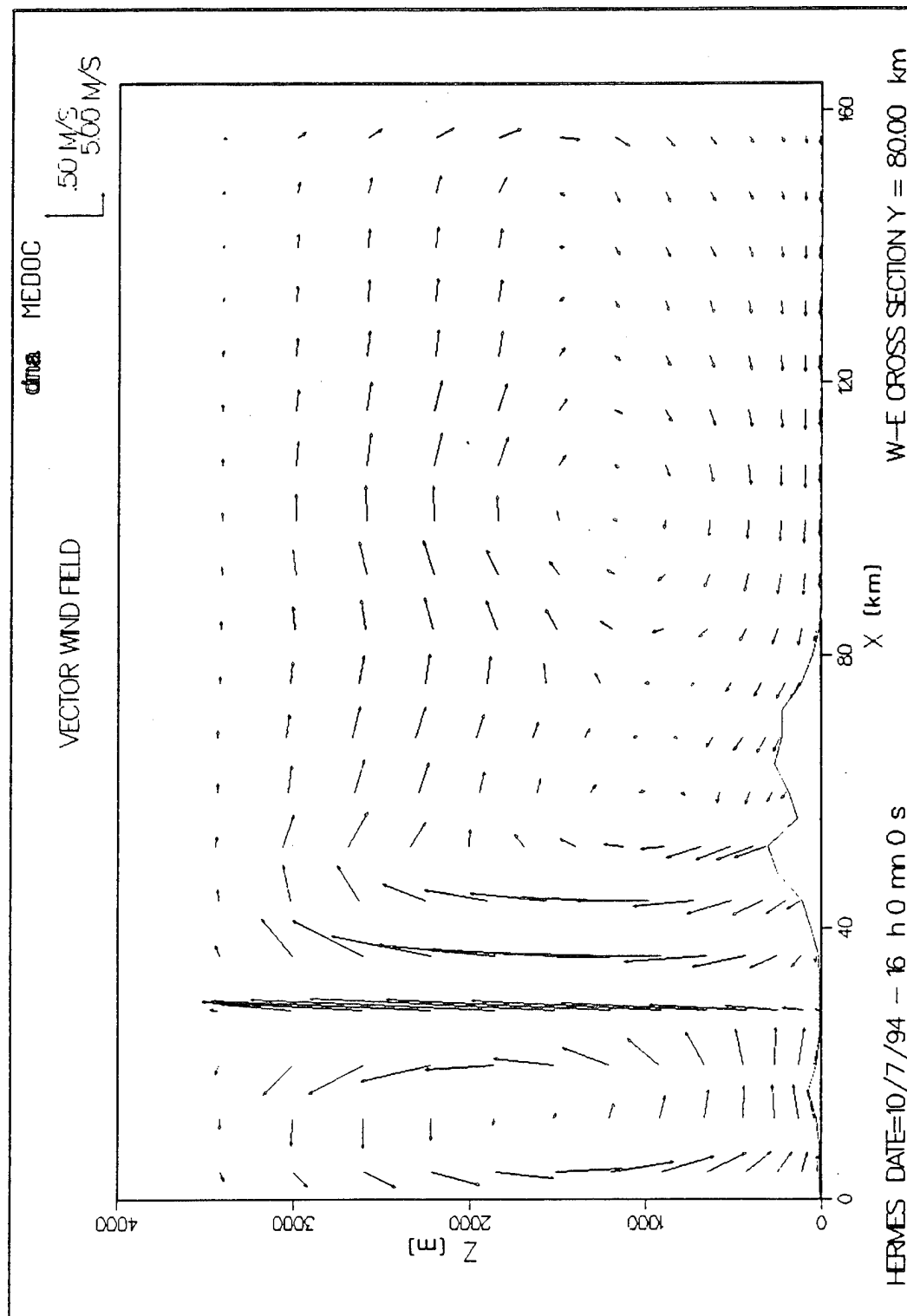


Figure 4-13. Wind field in a vertical plane at mid day from HERMES sea breeze calculation.

4.4 SIESTA - COMPLEX TOPOGRAPHY EFFECTS.

4.4.1 What is SIESTA?

"SIESTA" represents an international mesoscale tracer experiment (Reference 19) for transport of gases in a complex terrain environment. This landmark experiment was conducted during November 1985 in the Swiss Alps near the Gosgen, Switzerland nuclear power plant site. Mean winds and turbulence along with SF6 tracer concentrations were measured over regions covering approximately 35 KM downwind from the tracer release point. Wind and turbulence data were collected from meteorological towers, tethered balloons, and routine Swiss soundings. SF6 concentrations were sampled at a height of 1 meter above ground level along a series of arcs downwind from the source point which was situated 6 meters above ground.

Given the comprehensive and extensive nature of the SIESTA experiments, they were subsequently chosen for use in the evaluation and selection of calculational models for dispersion simulation of potential airborne radioactivity from power plants in complex terrain areas. This evaluation was conducted by the Paul Scherrer Institute (PSI), a public funded Swiss research center, under the supervision of Dr. Volker Herrnberger (Reference 20). Modeling results for the SIESTA cases were generated by numerous modelers from the international community.

4.4.2 The SIESTA Model Evaluation Process.

For the evaluation of models, two particular days from the SIESTA Experiment were selected involving different wind and stability conditions. As the wind direction on the two days differed by approximately 180 degrees, with the same tracer release point, the two days also involved different topographies. The days selected were the 24th of November with a neutral atmosphere and winds from the NEE direction, and the 30th of November with a stable atmosphere and weak winds from the WSW to S directions.

As the primary intent of the model evaluation was to assess the relative performance of the dispersion models, a common meteorological database was supplied to all modelers, thus eliminating any influence of individual diagnostic flow models. Further, because "the time variation of the meteorology was fairly modest" and "to facilitate the analysis for the modeler by offering a database of moderate size", the database supplied was derived as an average of the wind field and turbulence data taken (on each day) over a six hour period. During these periods the SF₆ tracer was released continuously at a constant rate. Expecting concentration distributions in the last hour of the release periods to be near steady state throughout the data collection region, calculated values were compared to concentration data averaged over the last (sixth) hour. While this represents a significant simplification, it was considered reasonable in view of the objectives and the prevailing conditions as stated above. As a follow-on, however, a time dependent evaluation was planned by PSI in which "the modeler generates the (non-stationary) windfields and turbulent parameters from the original meteorological measurements by averaging over reasonably small time intervals depending on his flow model and expertise". Results of this second phase of model validation are to be reported for all models by PSI.

In attempting to find the best of all available models for evaluation, the evaluation team formulated a detailed questionnaire covering approximately 90 items which was then distributed to 34 modelers responsible for 38 different models. After careful screening of the questionnaire responses, 10 models were selected for more detailed evaluation involving calculations and comparisons with the SIESTA data. *The calculations were performed as a blind test in which none of the modelers had access to the measured concentration data.* The selected models, which provided a variety of methodologies, included: 2 puff models, 3 Eulerian models, 3 Lagrangian models, and 2 Eulerian/Lagrangian hybrids. Of the 10 models, 2 were MEDOC codes, including HERMES and TRAMES. MEDOC results from the evaluation are presented below. In addition, because SIESTA represents an important validation of MEDOC, the follow-up effort to perform the non-stationary calculations was carried out in part under the DNA MEDOC Program and is presented below. Because of their interest in the MEDOC codes and their validation, partial support for this additional validation effort was provided to ARIA Technologies by the French Electricity Board.

Before discussing model performance, the topographies involved in the experiment are illustrated along with sample wind fields. Figure 4-14 shows a three dimensional view of the topography involved on the 30th of November. It is a moderately hilly region with elevations ranging from 293 to 824 meters. The same topography is also illustrated in Figure 4-15 in the form of elevation contours. Also shown in Figure 4-15 are wind vectors near ground level for the average or stationary wind field case. A general pattern of flow from the southwest to the northeast is indicated. Significant curvature of the flow to a more southerly wind direction occurs through the northern valley region.

Turning to the experiment on the 24th of November, the affected topography is illustrated in Figure 4-16 from a three dimensional perspective, while Figure 4-17 gives the two dimensional view with elevation contours and the wind field vectors near ground level. The topography on this day is more rugged, with elevations ranging from 373 to 1273 meters. The most significant features are the prominent ridges ("Jura" Ridges) which separate a large valley to the south from narrower valleys to the north. These were found to play a significant role in the dispersion process on the 24th. The stationary wind pattern displayed in Figure 4-17 is seen to essentially blow parallel to the ridges.

For the stationary wind fields used in the model evaluations, PSI supplied all modelers with gridded fields which were derived from the 6 hour averaged wind data by application of a mass consistency wind field reconstruction model. The model used was CONDOR (References 21 and 13) which is similar to MINERVE. Horizontal grid resolution employed by CONDOR was 1 km. For further validation under the current DNA MEDOC Program and subsequent to the Swiss model evaluation, similar wind field reconstruction with the Swiss met data was performed using MINERVE with 1 km resolution followed by concentration calculations with HERMES and TRAMES. Winds and concentrations were found to be in reasonable agreement with those obtained using CONDOR with HERMES and TRAMES. This provides validation of MINERVE, not only on a code to code basis, but also in an objective sense since concentration calculations based on MINERVE winds were found to be in good agreement with data, in fact generally better agreement than calculations using CONDOR winds.

TOPOGRAPHY.
SIESTA
11/30/85

DATA MEDOC

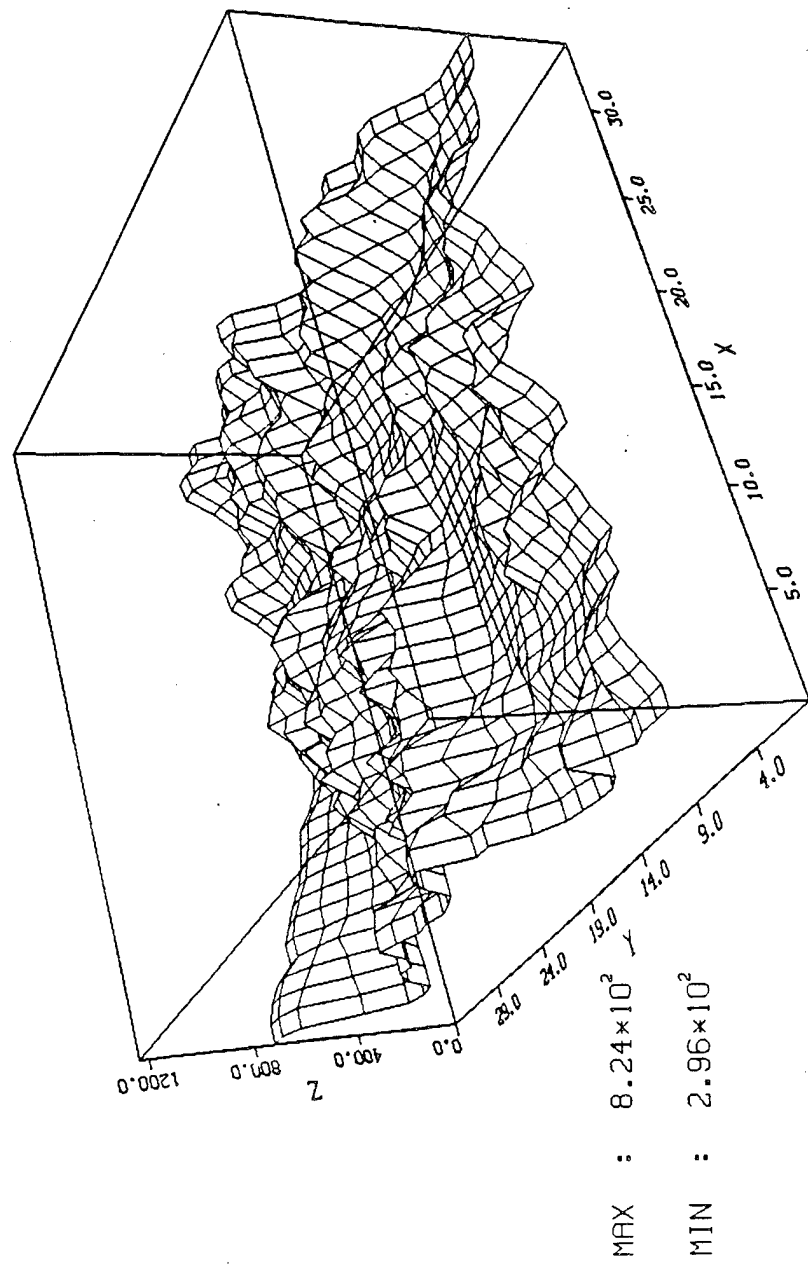


Figure 4-14. 3D View of SIESTA topography on 30 November.

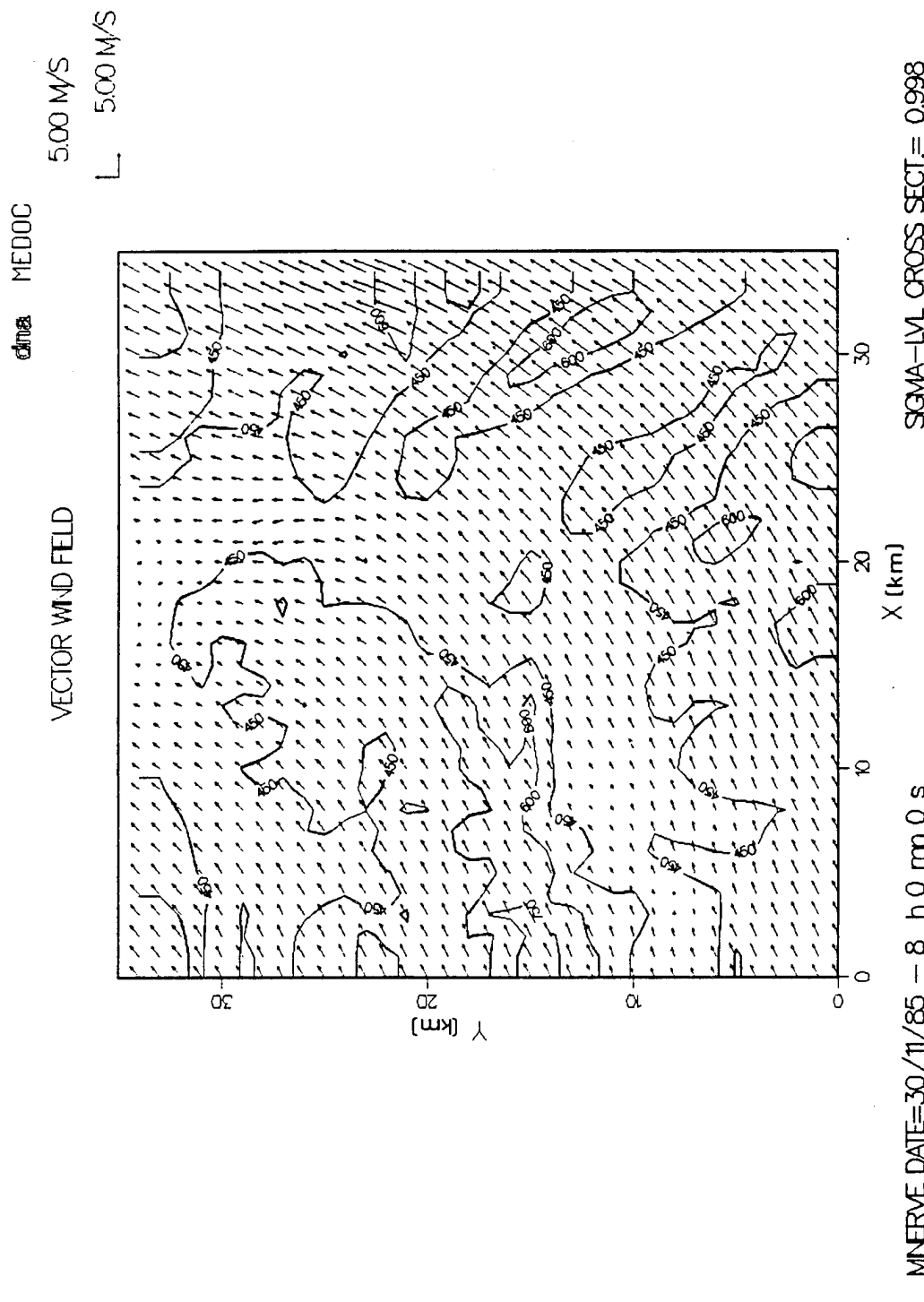


Figure 4-15. Elevation contours with stationary wind vectors for SIESTA topography on 30 November.

TOPOGRAPHY.
SIESTA
11/24/85

SIESTA
11/24/85

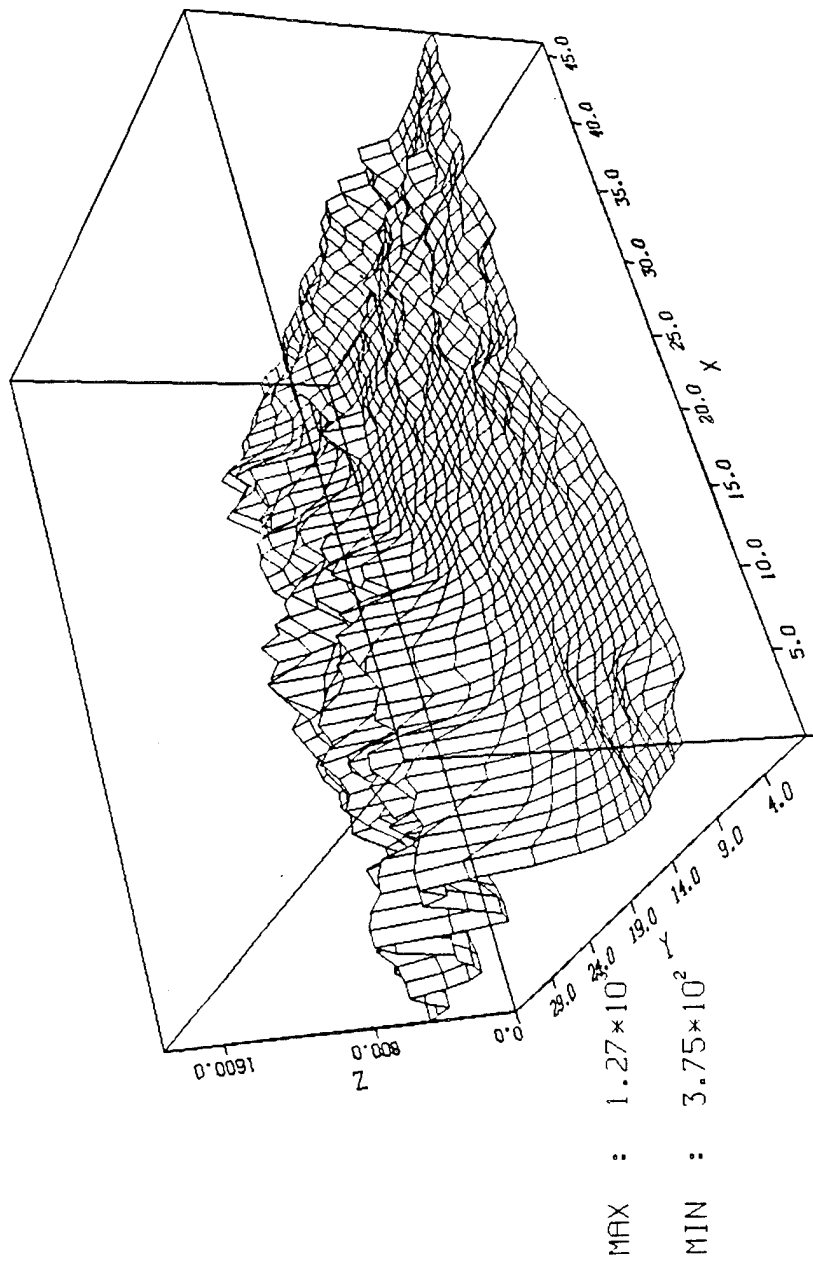


Figure 4-16. 3D View of SIESTA topography on 24 November.

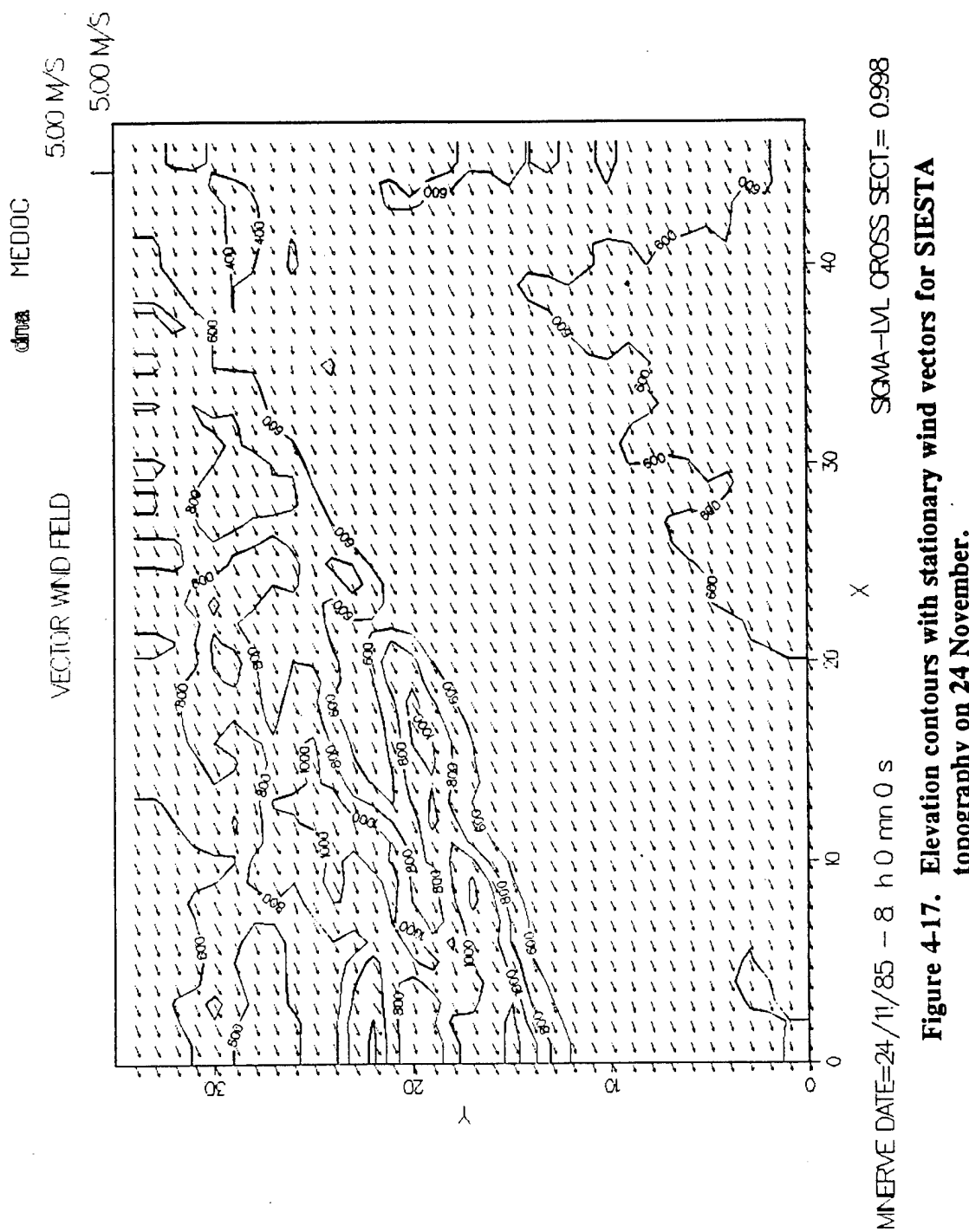


Figure 4-17. Elevation contours with stationary wind vectors for SIESTA topography on 24 November.

4.4.3 HERMES Validations with SIESTA.

HERMES concentration results from the Swiss evaluation study for the 30 November case are presented in Figure 4-18. These were generated with the DNA version of HERMES and found to be in very good agreement with HERMES results generated earlier for the Swiss study, thus verifying the integrity of the DNA version. They represent a steady state solution corresponding to the stationary wind field provided by PSI and generated with the mass consistency model CONDOR. The results in Figure 4-18 are presented for ground level concentrations in terms of isopleths with color shading. Given light winds in this case, advection is to some extent dominated by diffusion as indicated by the relatively wide plume. This is most evident near the source release point which is located near $X = 4$ km and $Y = 8$ km. The calculated ground level results are directly comparable to the SIESTA data, which were collected at a height of 1 meter, and are of greatest practical importance as they indicate population exposure.

For comparison with the data, PSI performed a series of visual and statistical tests which were applied to the blind test results of all models considered in the evaluation. Included amongst the statistical tests was the cumulative frequency distribution for the ratios of pairs of calculated to measured data, or measured to calculated, whichever is greater than one. The distribution for the 30th of November, as evaluated by PSI, was presented in Reference 20 and is shown here in Figure 4-19. While results for all of the models evaluated in the study are shown in the figure, their identification by name was withheld by PSI. However, because participating modelers were told which results applied to their particular models, it is known that the frequency distributions for "EUL-2" and "PUFF-2" correspond to HERMES and TRAMES, respectively. Thus, since greater modeling accuracy is indicated by smaller values for the pair ratios, HERMES is seen to be the best model, based on cumulative frequency distribution for the 30th of November.

For further statistical evaluation, PSI also generated scatter plots which complement the frequency distributions by indicating whether models over or under estimate data and whether the indicated errors are in the high or low ranges of the data, or both. The scatter diagram for

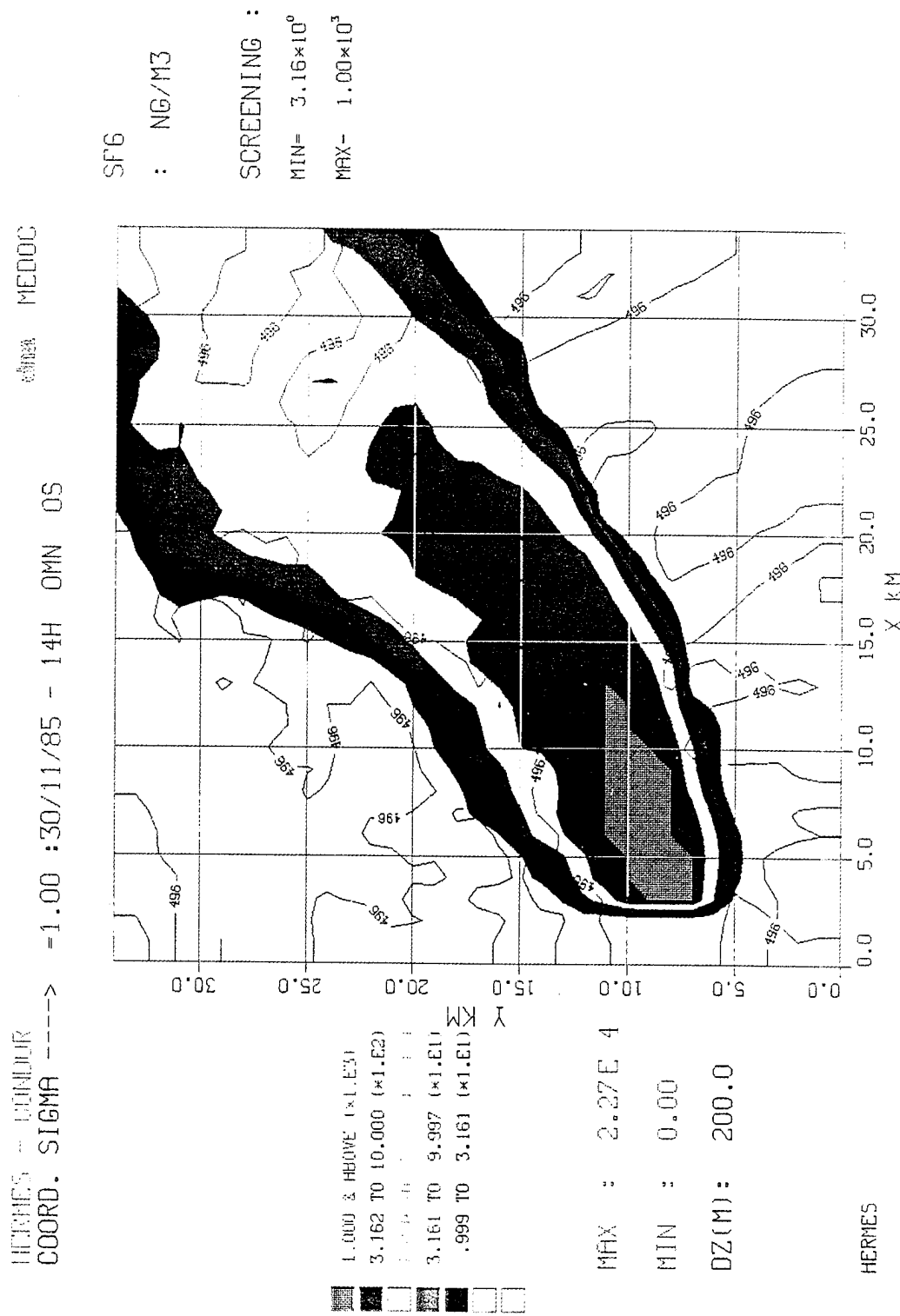


Figure 4-18. Ground level concentration contours with color shading for 30 November based on HERMES with CONDOR winds.

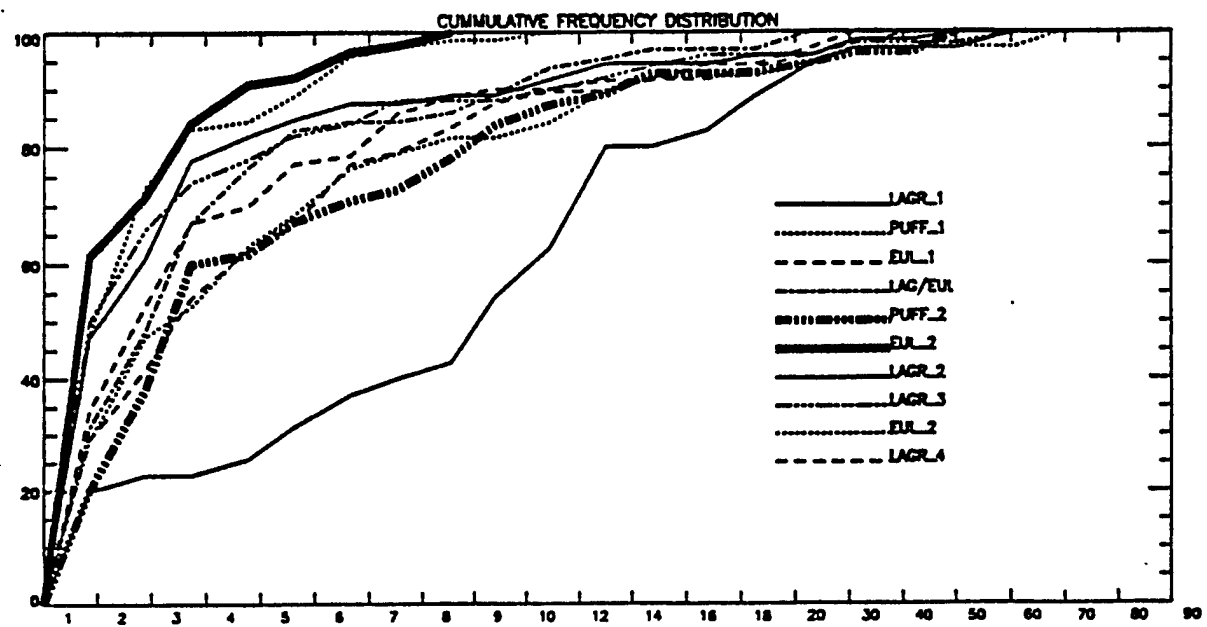


Figure 4-19. Cumulative distribution [%] of different models for SIESTA 30th versus PMCD- or PCMD- ratio > 1 .

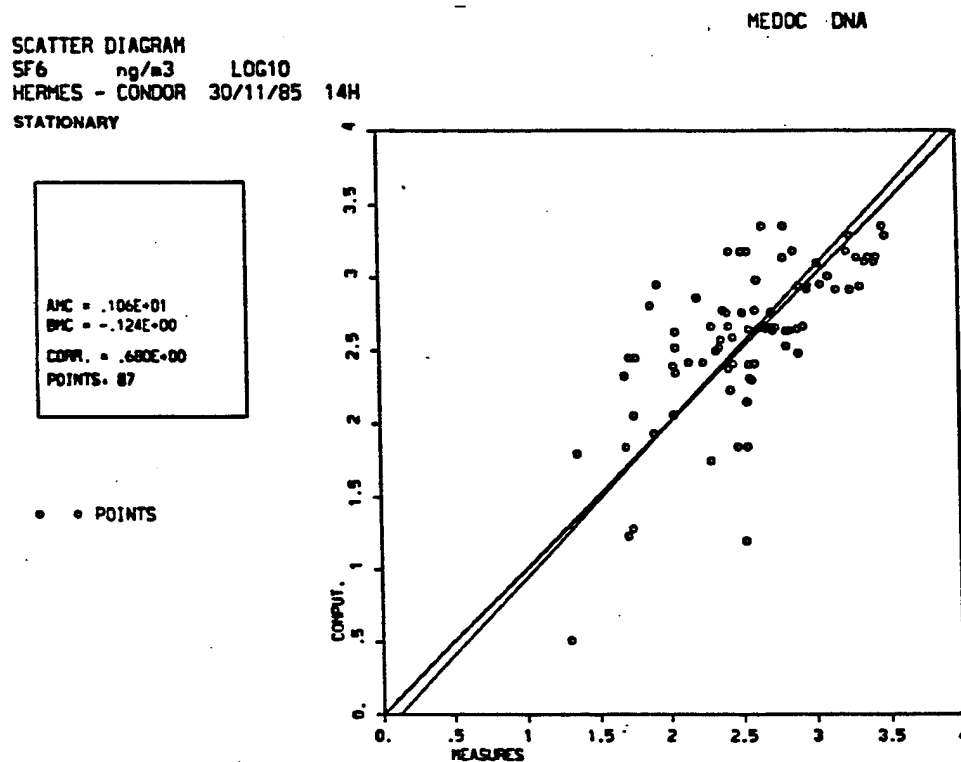


Figure 4-20. Scatter diagram for HERMES/CONDOR calculated concentrations for 30 November SIESTA Experiment.

HERMES corresponding to the frequency distribution in Figure 4-19 is given in Figure 4-20. Computed values are seen to be in good agreement with measured values. Shown with the plotted points is a least squares regression line as well as the computation/measurement bisector, i.e., the line for perfect agreement between computation and measurement. For the HERMES results in Figure 2-20, the least squares "best fit" line is seen to be very close to the bisector, with the amount of over- and under-prediction by the model being about equal. The spread in calculated concentrations, relative to measured values, is seen to be \pm one order of magnitude. The associated correlation coefficient is found to be 0.68, which is considered quite good for atmospheric dispersion calculations.

It should be noted that in the process of generating frequency distributions as given in Figure 4-19, PSI employed symmetric screening in which all points involving either measured or calculated values less than 30 nanograms/cubic meter (NG/M³) were ignored. This was based partly on the fact that the measurement threshold of instrumentation employed in the SIESTA Experiments was assumed to be 30 NG/M³. (actual thresholds were determined to be 18 NG/M³ for sensors provided by Danish contributors and 30 NG/M³ for those supplied by Italian participants). Thus it is appropriate to discard points where measurement values are less than 30 NG/M³. However, we do not feel it is similarly reasonable to discard points because calculated values are less than 30 NG/M³. This issue is particularly important when trying to assess the relative performance of different models, since poor model results, which are indicated by low calculated concentrations at points where sensor measurements are high, are not taken into account. However, to be consistent with the PSI frequency distributions, symmetric screening was employed in frequency distributions generated for this report. To provide another measure of the relative performance of HERMES and TRAMES on different days and with stationary and nonstationary winds, asymmetric screening (screening only measured values < 30 NG/M³) was used for the generation of scatter diagrams and regressions. In so doing a more compete set of meaningful data points is presented, including points with low calculated, but high measured, values.

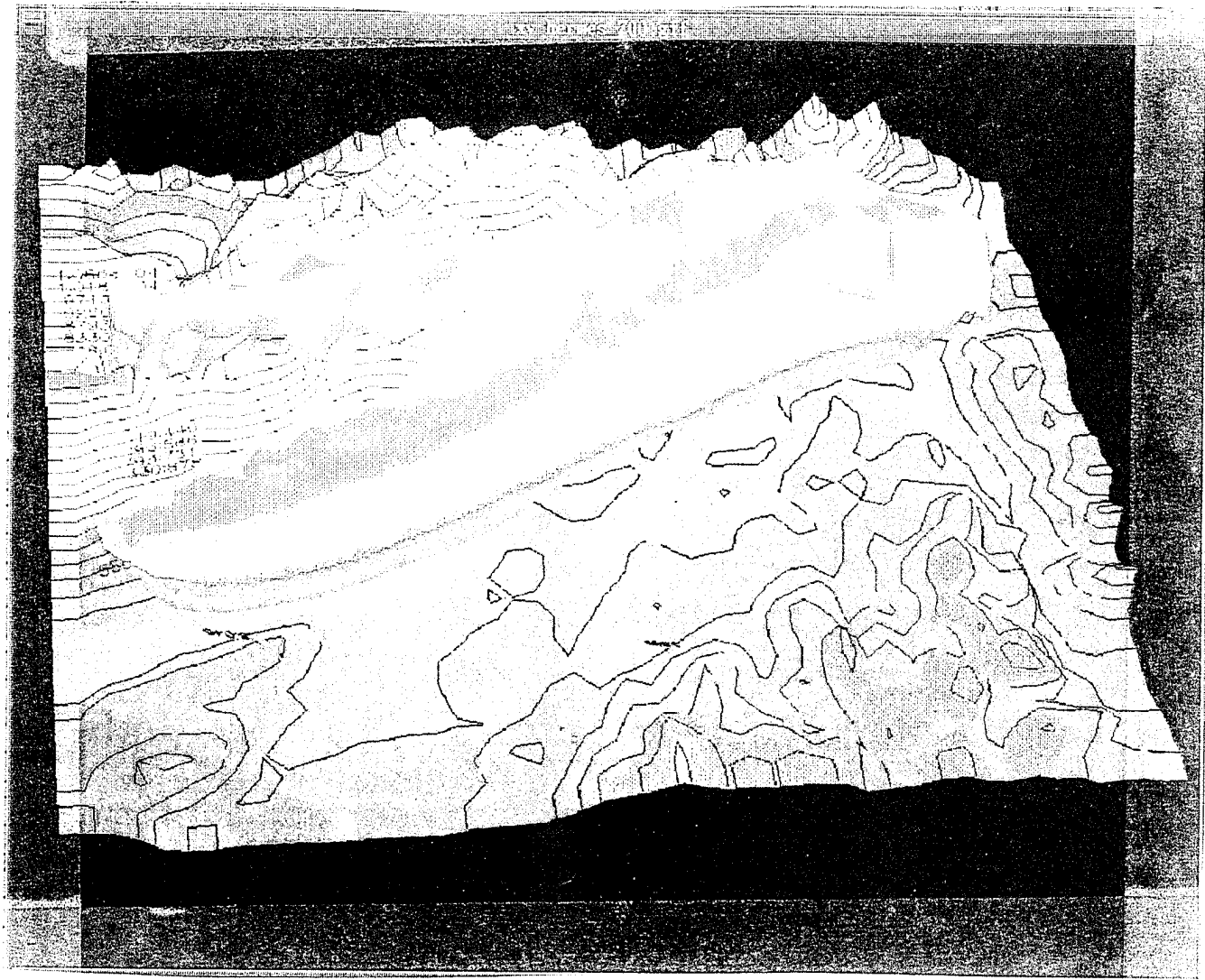


Figure 4-21. Isocconcentration surface (100 ng/m³) for HERMES/CONDOR calculated concentrations for 24 November SHESTA Experiment.

Turning to the evaluation for the 24th of November, HERMES calculations display a much more interesting concentration distribution. This is shown in Figure 4-21, in the form of an isoconcentration surface (concentration = 100 NG/M³). Because of the topography, particularly the Jura Ridge, the SF₆ cloud is seen to have bifurcated, with one branch in the main valley to the south and another in a narrower valley to the north. This behavior is further illustrated in Figure 4-22 which shows concentration contours in a north to south vertical slice through the plume. Here the concentrations (presented as mass fractions, i.e., NG of SF₆/KG of air) in the north valley are clearly seen to reach peak values of the same order of magnitude as in the main valley. Though the bifurcation is believed real, data were, unfortunately, not available to confirm transport into the north valley. As reported in Reference 20, concerning the arcs along which measurements were made, "the calculated mean plume direction lies by some degrees outside the outer (downwind) arcs in mountain regions (north valley), where arc measurements were foreseen, but could not be completed due to difficult snow conditions." None the less, the only three models in the evaluation, including HERMES, which showed the bifurcation, are considered superior by PSI.

The HERMES calculated ground level concentrations, which can be compared with the measured values, are displayed in Figure 4-23 in terms of isopleths with color shading across intermediate regions. The computations illustrated in the figure were performed with 1 km horizontal grid resolution. The source was located near the coordinates X = 43 km and Y = 29 km. Comparing these results with the measured data yields the cumulative frequency distribution and scatter diagram shown in Figures 4-24 and 4-25 respectively. While the results shown in Figure 4-24 and 4-25 are not as good as similar results for HERMES on November 30 (Figure 4-19 and 4-20), they are still considered quite good, having been judged by PSI as one of the three best models. The difference in accuracy/statistical evaluations between the two days is believed to be an effect of the greater complexity of the terrain, and possibly the reduced number of operating sensors in impacted regions, on the 24th. From the scatter diagram, Figure 4-25, it is noted that a correlation coefficient of 0.612 is obtained with the regression line indicating a tendency for HERMES to underestimate values in low concentration (measurement) range and

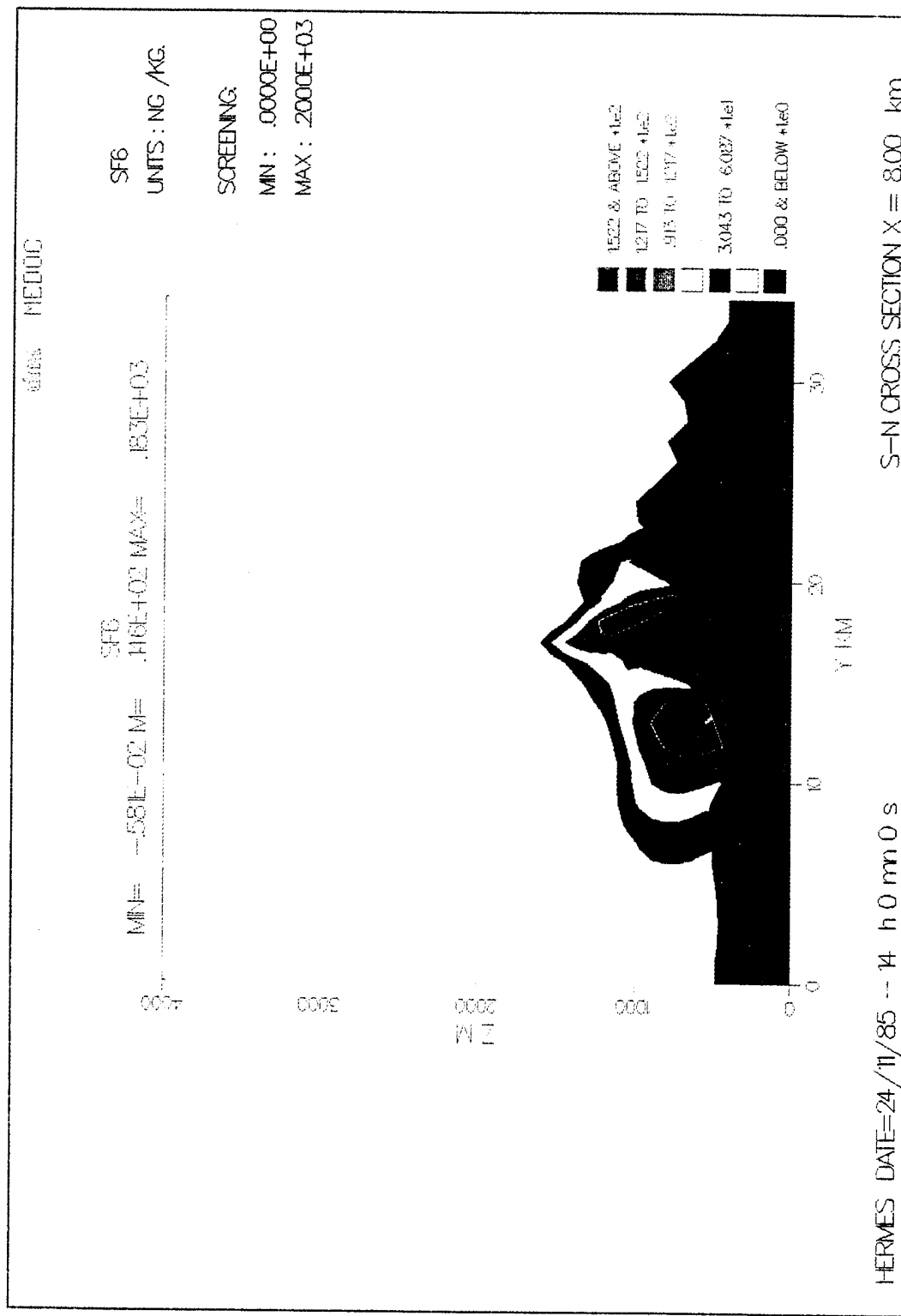


Figure 4-22. Plume cross section in North-South vertical plane through HERMES/CONDOR calculated concentration field for 24 November SIESSTA Experiment.

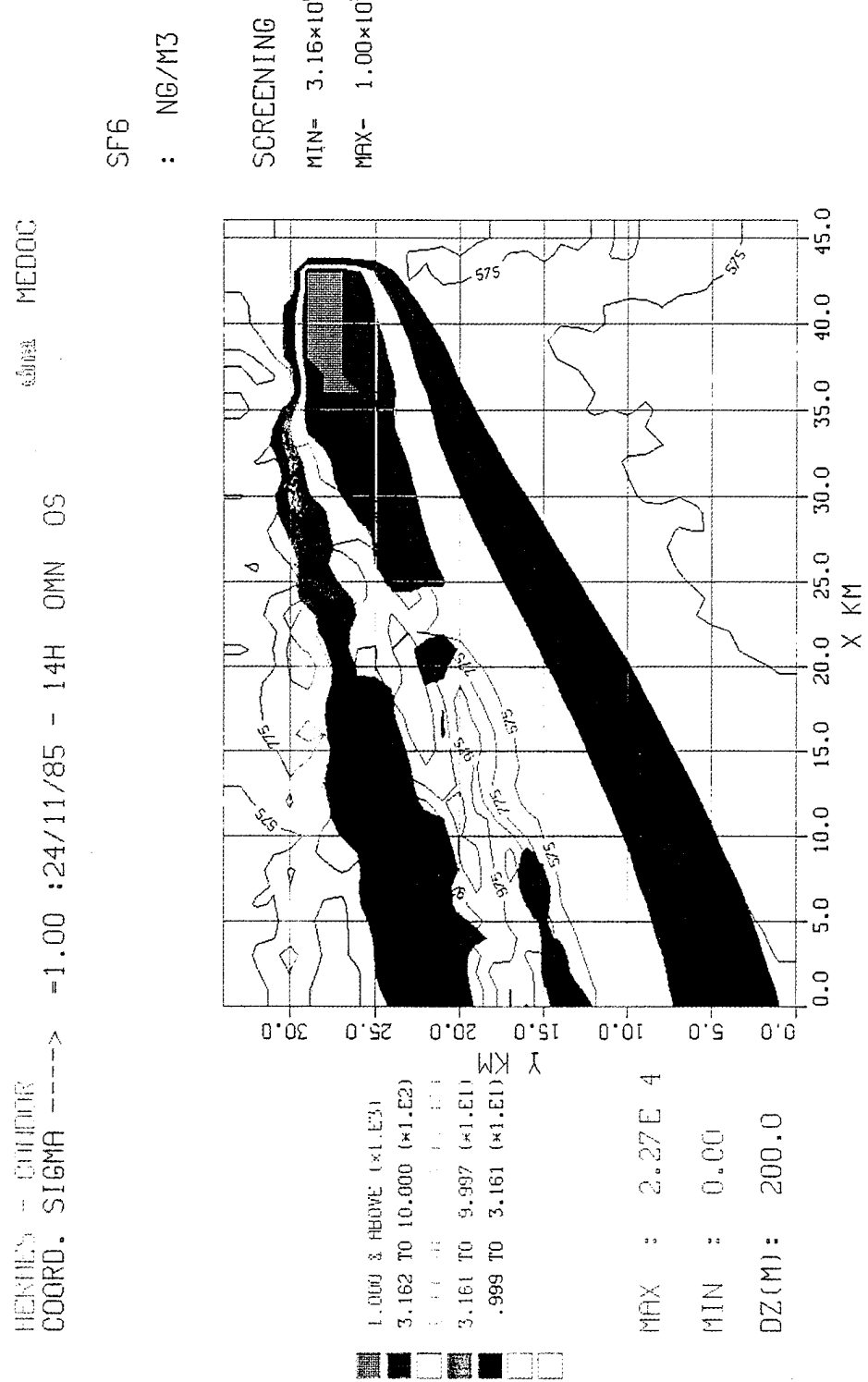
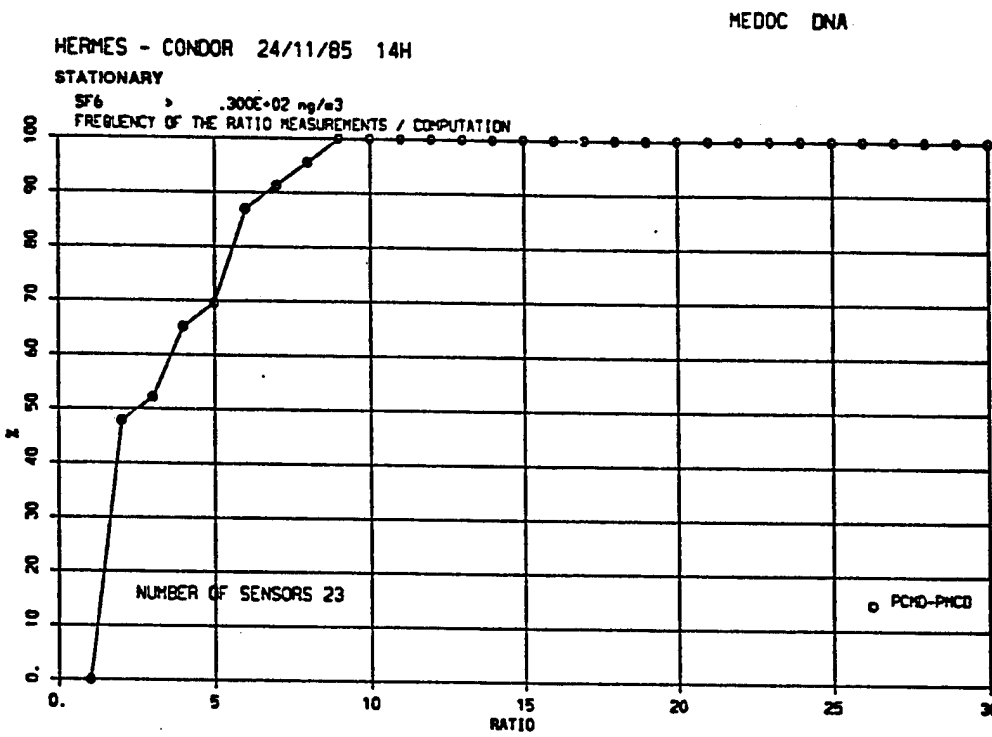


Figure 4-23. Ground level concentration contours with color shading for 24 November based on HERMES with CONDOR winds.



HERMES DATE = 24/11/85 - 14 H 0 MN 0 S.

Figure 4-24. Cumulative frequency distribution for HERMES calculation with CONDOR winds on 24 November.

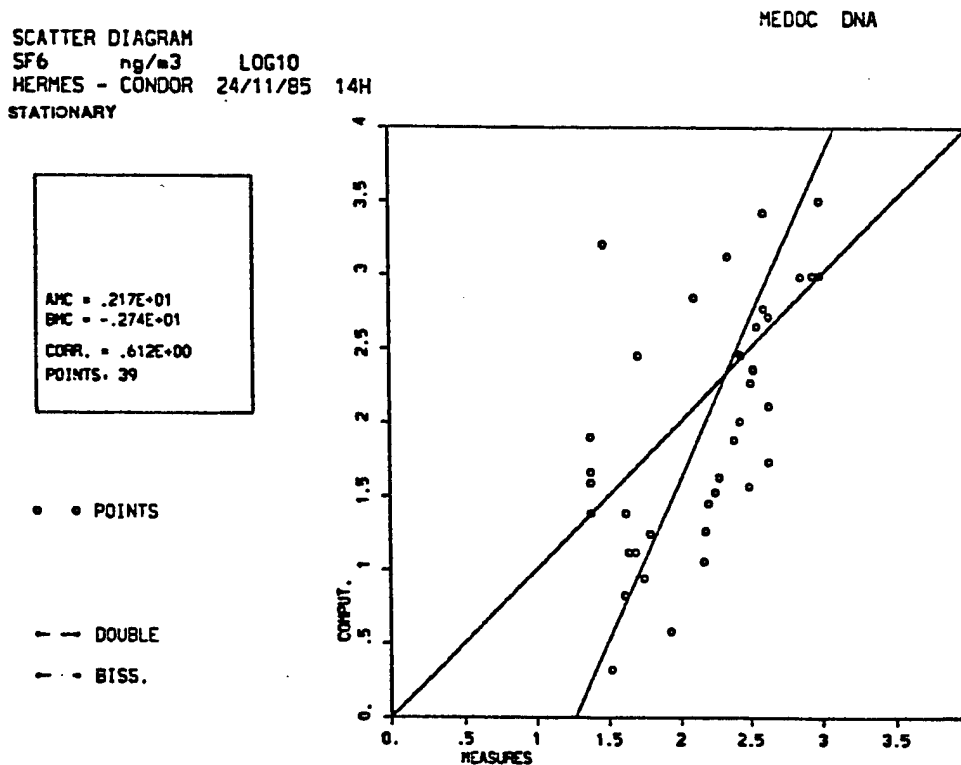


Figure 4-25. Scatter diagram for HERMES calculation with CONDOR winds on 24 November.

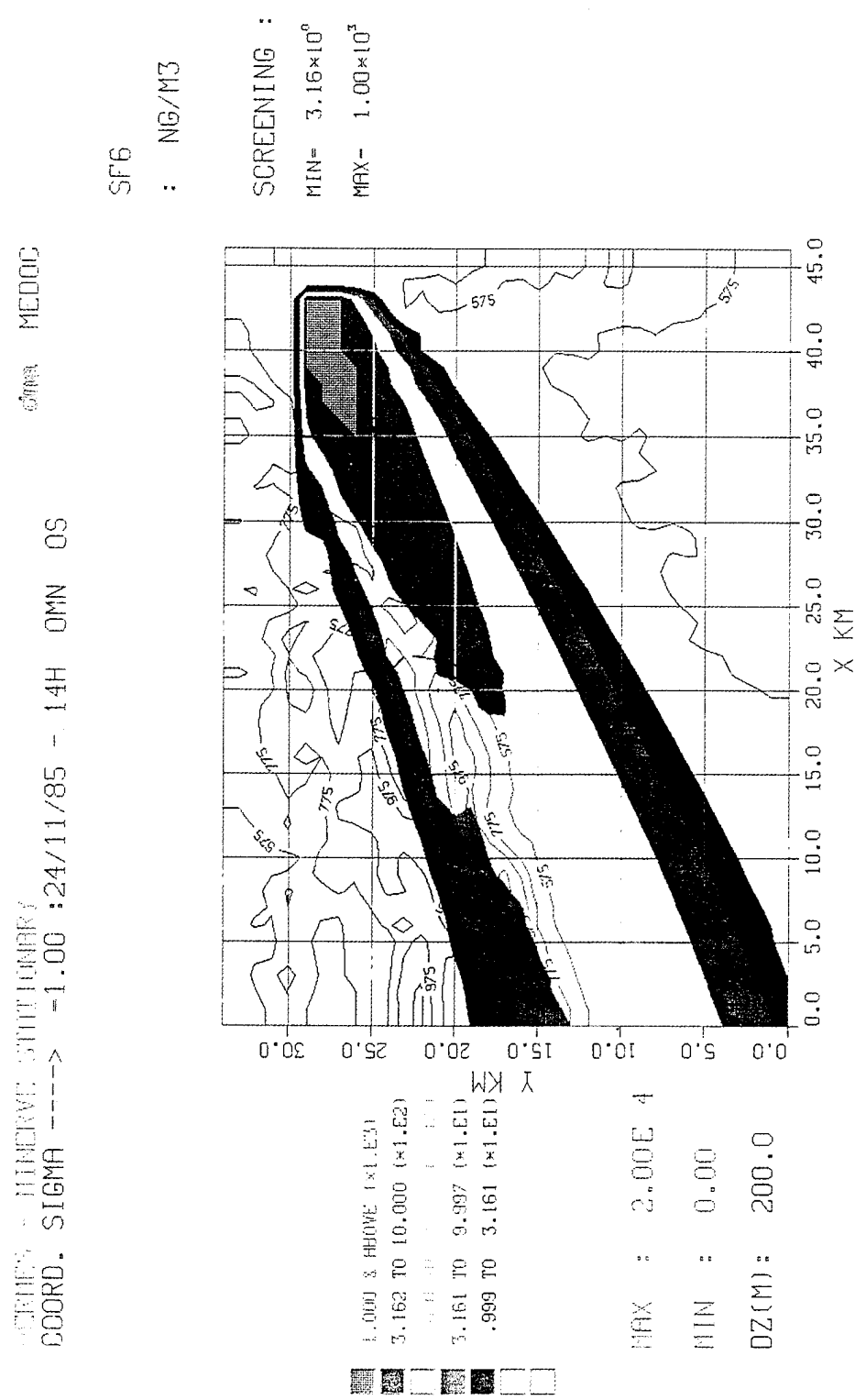


Figure 4-26. Ground level concentration contours with color shading for 24 November based on HERMES with stationary MINERVE winds.

HERMES HERMVF NON-SHIFT UNIFRT
 COORD. SIGMA --> = 1.00 : 24/11/85 - 14H 05
 HERMES MEDOC : 24/11/85

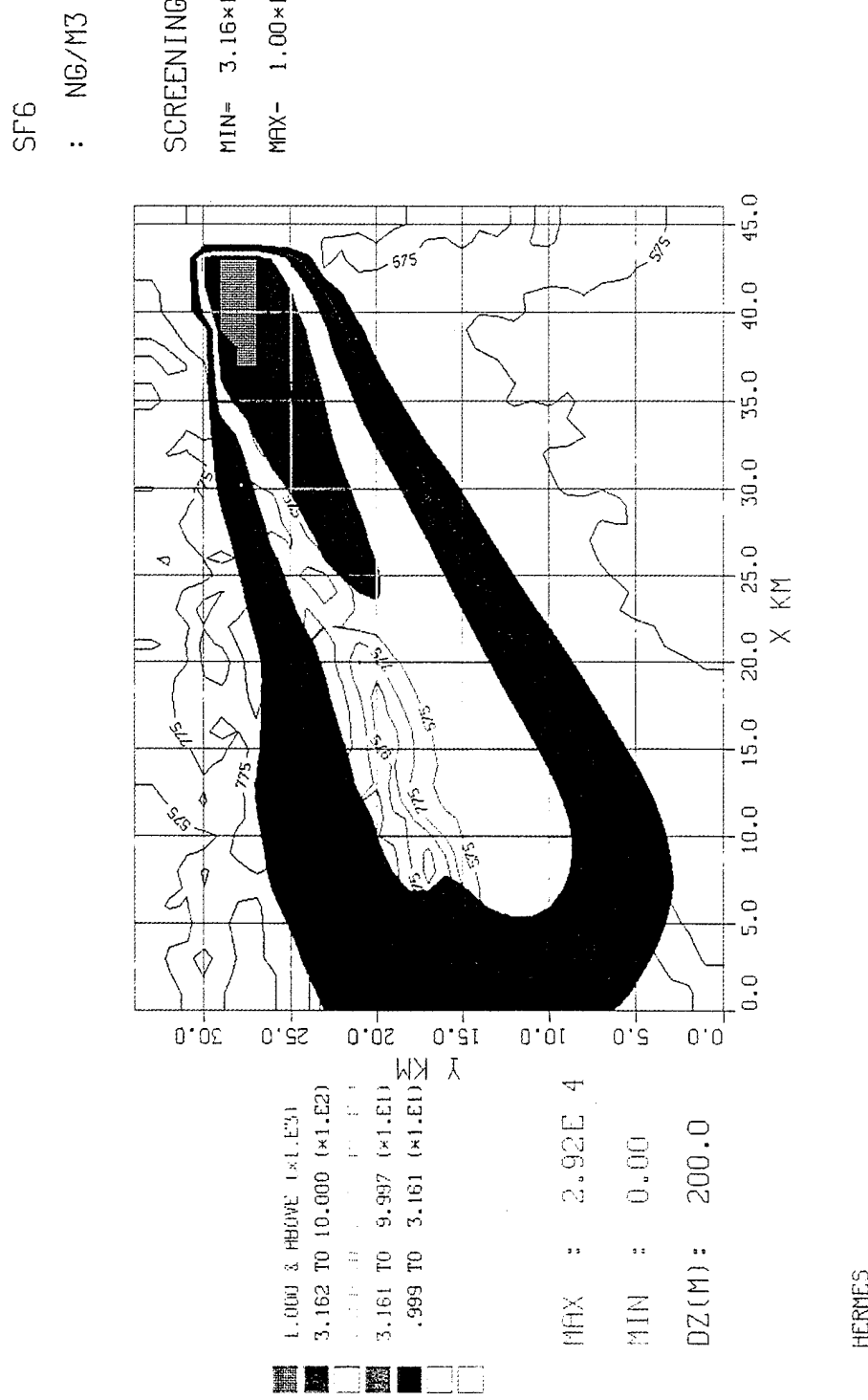
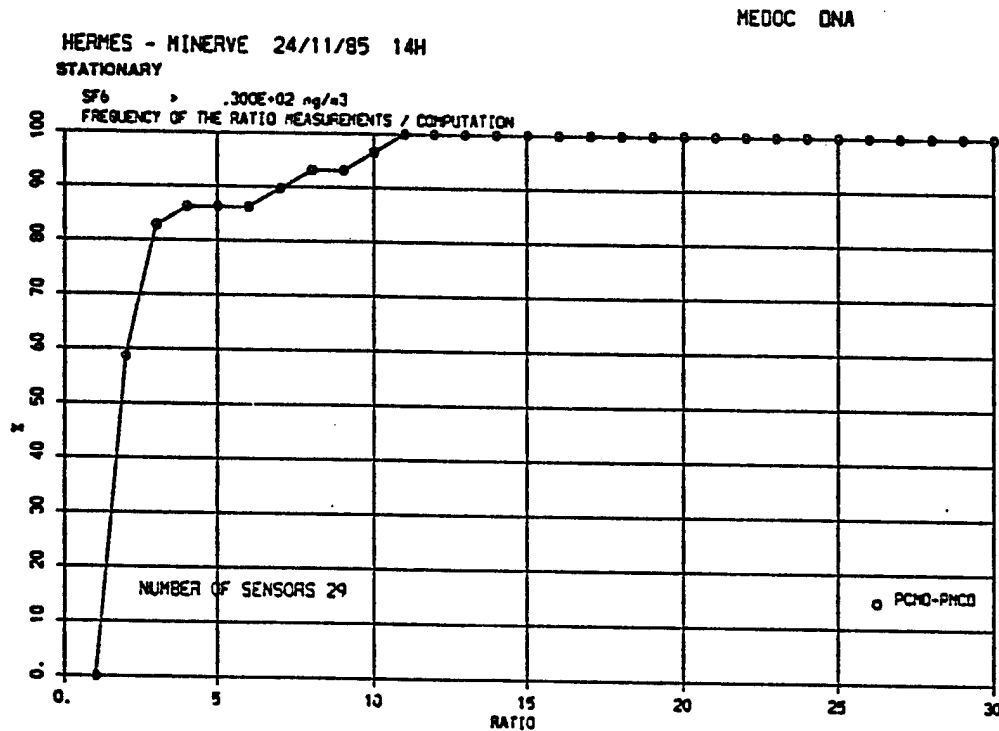


Figure 4-27. Ground level concentration contours with color shading for
 24 November based on HERMES with nonstationary MINERVE winds.



HERMES DATE = 24/11/85 - 14 H 0 MN 0 S.

Figure 4-28. Cumulative frequency distribution for HERMES calculation with stationary MINERVE winds on 24 November.

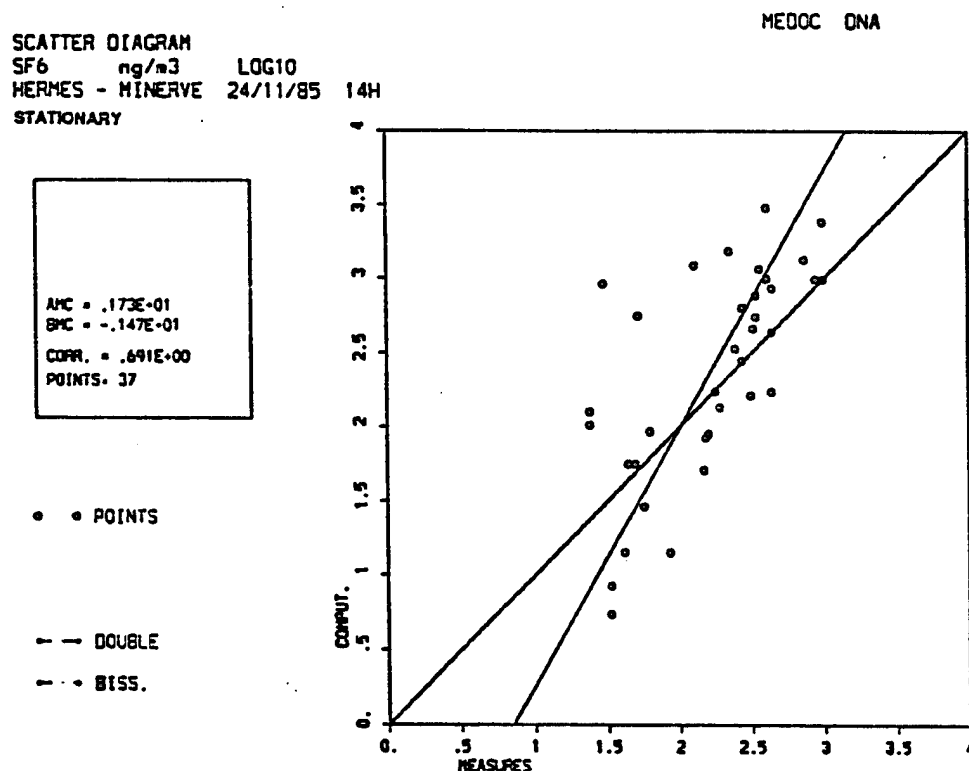


Figure 4-29. Scatter diagram for HERMES calculation with stationary MINERVE winds on 24 November.

to overestimate for the higher concentrations. To some extent this tendency is a result of the asymmetric screening which keeps low computed values but not low measured values.

As a further evaluation of HERMES, as well as MINERVE, the wind field on the 24th was recalculated with MINERVE for both stationary conditions as assumed by CONDOR, and for the time varying, nonstationary, conditions. These resulting winds were then used to carry out new HERMES concentration calculations. Figures 4-26 and 4-27 display the HERMES ground level concentrations based on the MINERVE stationary and nonstationary winds respectively. Comparing the MINERVE driven stationary plume (Figure 4-26) with that based on CONDOR (Figure 4-23) shows a very similar structure. The plumes follows a trajectory slightly farther to the south, i.e., somewhat more in the main valley and less in the north valley. For the nonstationary MINERVE/HERMES results, Figure 4-27 also shows a plume turned somewhat to the south as for the stationary MINERVE result. In addition, however, the nonstationary plume appears wider, with a reduced downwind extend, thus indicating somewhat reduced effective wind speeds.

To assess the validity of the MINERVE related concentration calculations, frequency distributions and scatter diagrams were generated as for the CONDOR/HERMES calculations. Figure 4-28 and 4-29 show the frequency distribution and scatter diagram respectively for the stationary MINERVE case. Comparing the frequency distribution based on the stationary MINERVE winds (Figure 4-28) with that based on CONDOR (Figure 4-24) shows that MINERVE gives better results than CONDOR, i.e., greater frequency of lower PCMD-PMCD ratios. Comparison of the scatter diagrams (Figures 4-29 and 4-25) shows a similar relationship between calculated and measured concentrations, but with an improved correlation coefficient of 0.691 using MINERVE, versus 0.612 with CONDOR. Since results are basically the same using MINERVE and CONDOR, this serves as a code-to-code validation of MINERVE. Since concentration measurements are well represented by calculations based on MINERVE winds, it also provides an indirect, but data based, validation of MINERVE. The fact that HERMES agrees well with data, using either CONDOR or MINERVE, also serves to validate HERMES.

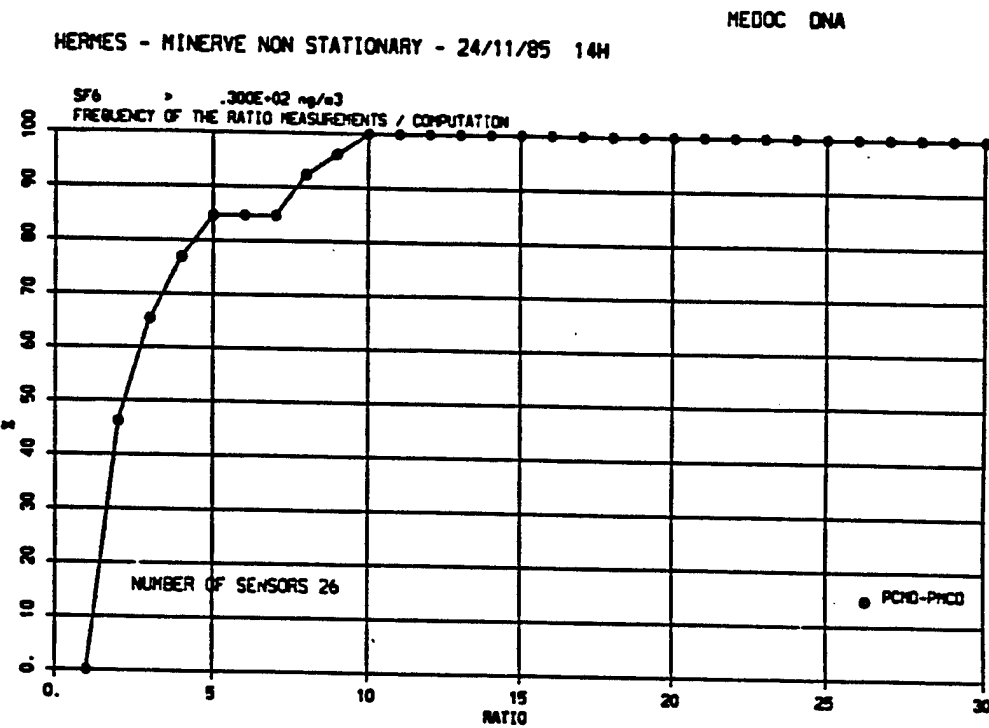


Figure 4-30. Cumulative frequency distribution for HERMES calculation with nonstationary MINERVE winds on 24 November.

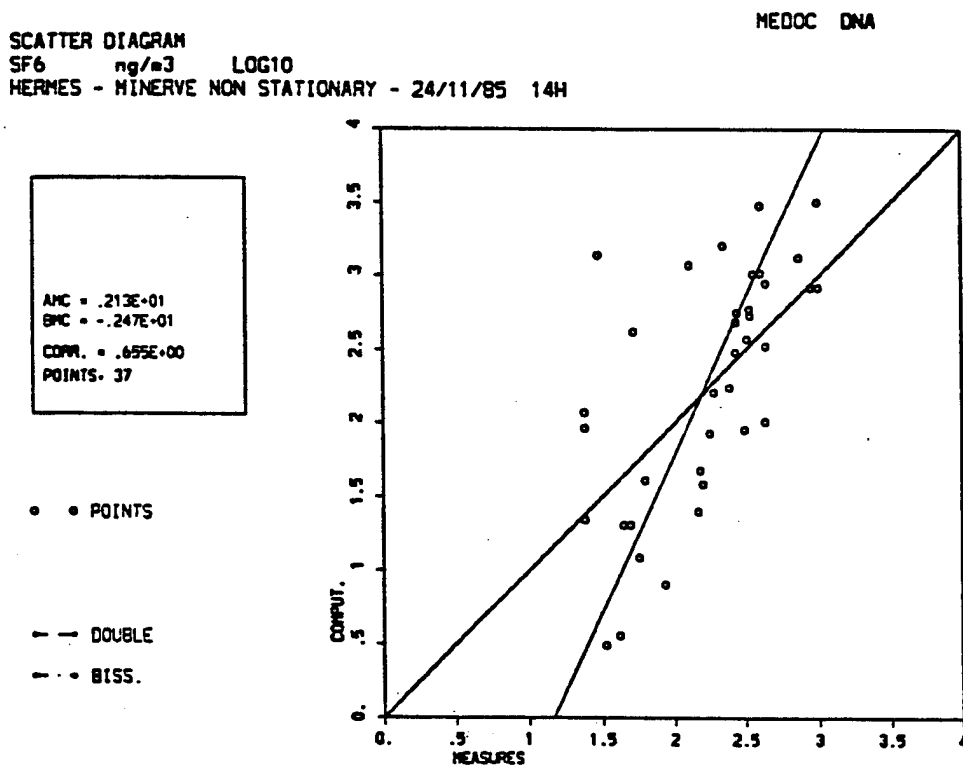


Figure 4-31. Scatter diagram for HERMES calculation with nonstationary MINERVE winds on 24 November.

Turning to the nonstationary MINERVE based results, for which time accurate HERMES calculations were performed and then averaged over the last (6th) hour, Figures 4-30 and 4-31 give the corresponding frequency distribution and scatter diagrams respectively. Comparison of the frequency distributions for the stationary and nonstationary MINERVE cases (Figures 4-28 and 4-30) indicates nominally equivalent performance, with the nonstationary results appearing not quite as good as the stationary. Comparing with results based on CONDOR, however, shows that the nonstationary MINERVE still gives slightly better results than CONDOR. This relative performance appears to be confirmed by comparison of the scatter diagrams for the three cases (Figures 4-31, 4-29, and 4-25). Though relative performance is not entirely obvious from the scatter points, other than approximately equivalent performance for the three cases, the associated correlation coefficients show stationary MINERVE as best and nonstationary MINERVE as second best.

As a further display of modeling performance, Figure 4-32 displays side by side bar indicators for calculated and measured concentrations for the nonstationary MINERVE/HERMES case. While somewhat difficult to discern, due to the closeness of sensor locations, generally good agreement appears. The primary difference between calculated and measured values appears to be a tendency for calculations to underestimate measurements by increasing amounts towards the southern limits of the measurement arcs. This could be due to very slight errors in wind directions, thus emphasizing the importance of accurate wind fields. Another potential cause is the selected computational domain which does not include an additional weather station which is located south of the domain and which shows somewhat more northerly winds. Other computational errors can be seen along the first measurement arc, in the northeast corner nearest the source, where measured values are somewhat overestimated by calculations. In general, such differences are far from excessive in atmospheric transport dispersion modeling. In fact, the overall agreement especially including the more distant arcs, is considered very reassuring.

SCALAR FIELD. 24/11/85 14H 0
SCALAR BARS (MEASUREMENTS/COMPUTATIONS) - SF6 NG /
HERMES - UNSTEADY WINDS
HERMES - UNSTEADY WINDS

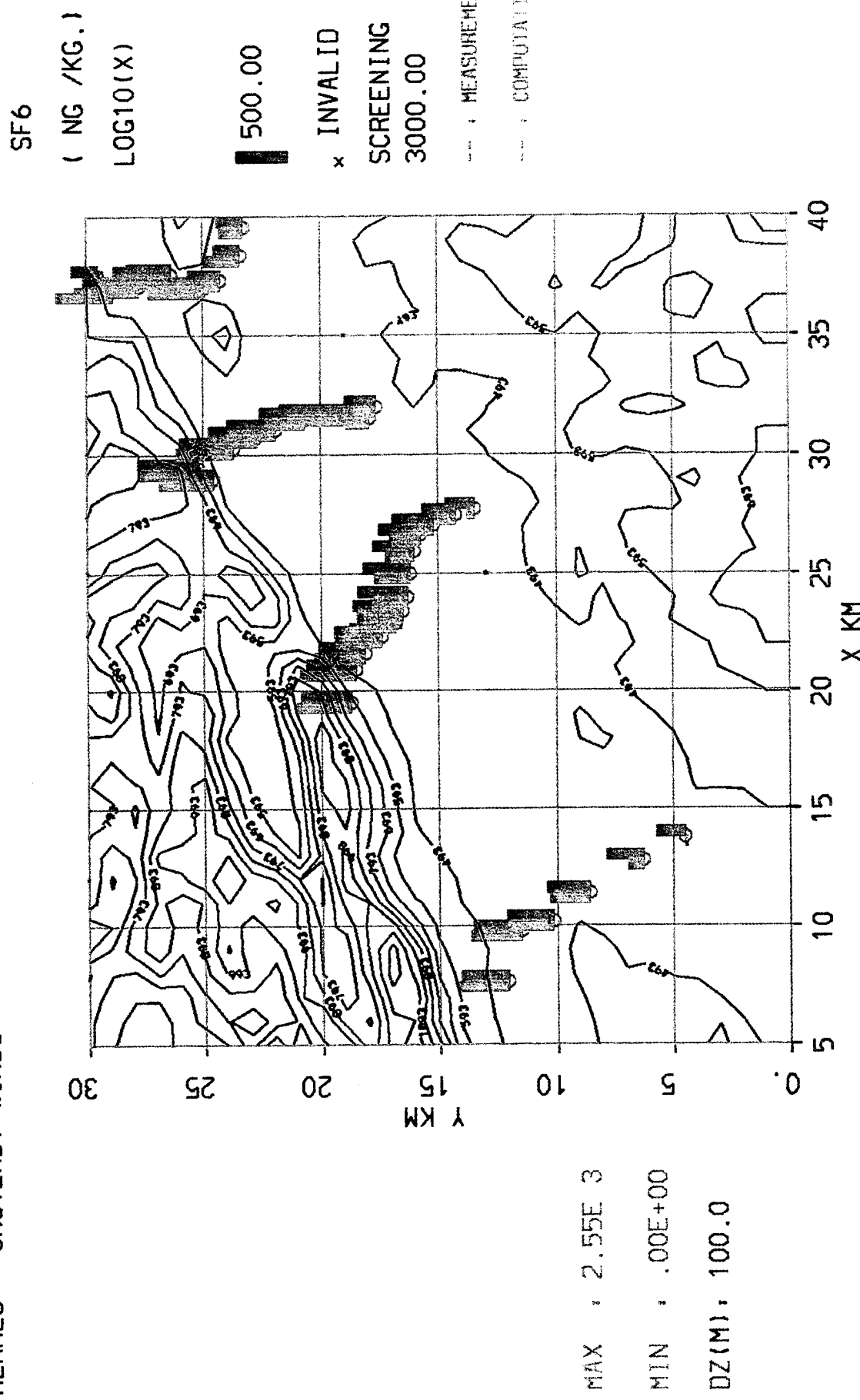


Figure 4-32. Bar indicator comparisons between SIESTA measurements on 24 November and HERMES calculations with nonstationary MINERVE winds.

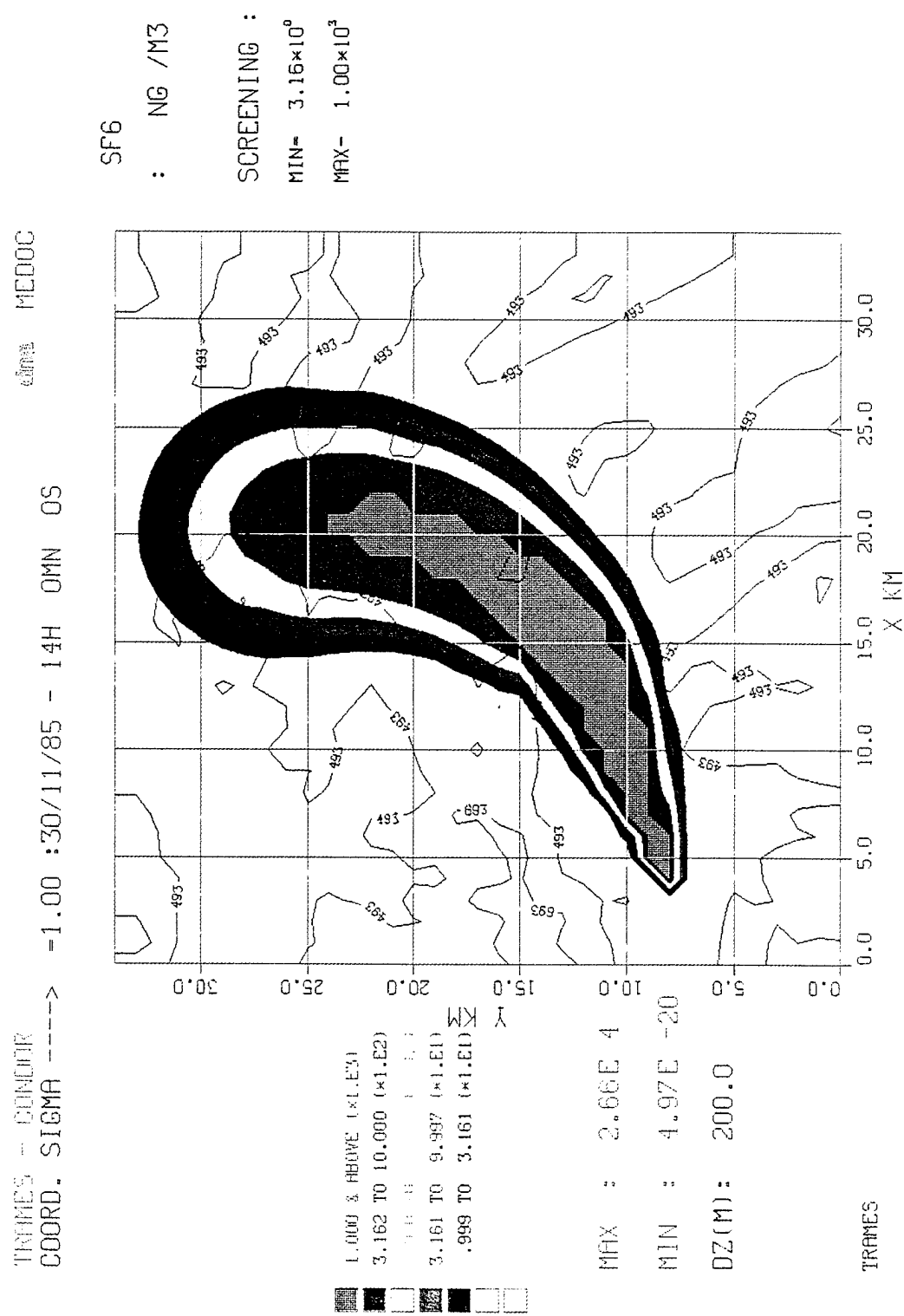


Figure 4-33. Ground level concentration contours with color shading for 30 November based on TRAMES with CONDOR winds.

SCATTER DIAGRAM
SF6 NG /M3 LOG10
TRAMES - CONDOR 30/11/85 14H
STATIONARY

MEDOC DNA

AMC = .295E+01
BMC = -.498E+01
CORR. = .555E+00
POINTS = 71

• • POINTS

— — DOUBLE

— - - BISS.

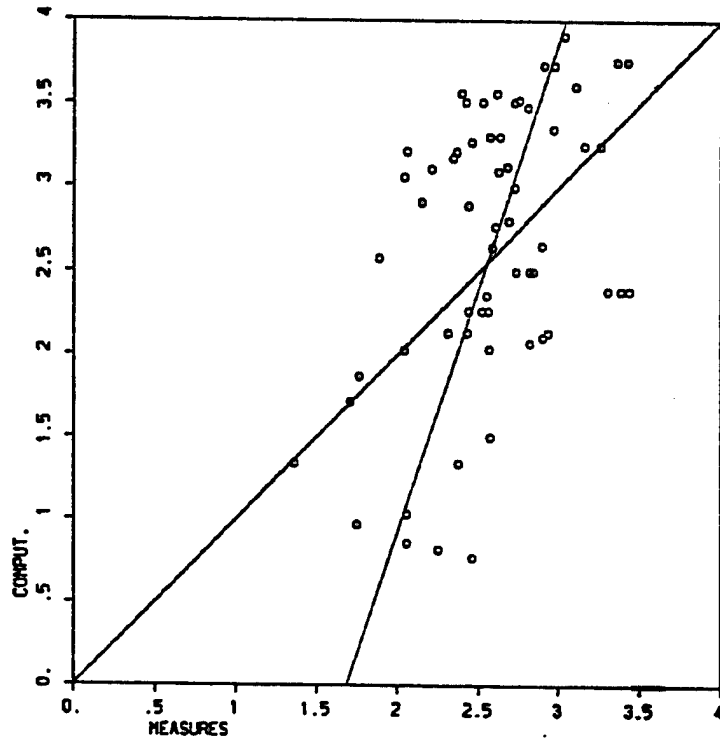


Figure 4-34. Scatter diagram for TRAMES/CONDOR calculated concentrations for 30 November SIESTA Experiment.

4.4.4 TRAMES Validations with SIESTA

Starting again with the 30th of November experiment, TRAMES was exercised under the original PSI model evaluation using the CONDOR stationary wind field. The resulting ground level concentrations are shown in Figure 4-33. Comparing this with the HERMES/CONDOR ground level concentrations (Figure 4-18), TRAMES is seen to yield a more simple/classical ground level profile representing a narrower/tighter or less diffusive plume. Peak concentrations for TRAMES are somewhat higher, while the downwind extent is less. The frequency distribution for the TRAMES calculation, as calculated by PSI, is illustrated in Figure 4-19 where it is designated as PUFF-2. Thus TRAMES is seen to provide less accurate results than

HERMES, and might be rated as average to low average compared with other models in the PSI evaluation. The scatter diagram for TRAMES is given in Figure 4-34, and again by comparison with the corresponding diagram for HERMES (Figure 4-20), clearly shows less accuracy with TRAMES.

For further evaluation of TRAMES on 30 November, new calculations were performed using a MINERVE stationary wind field calculation. The resulting ground level concentrations are displayed in Figure 4-35. Comparing with the TRAMES/CONDOR plume, the MINERVE based plume is seen to blow further to the east and to have a greater downwind extent. To determine the relationship of these differences to modeling accuracy, the frequency distribution and scatter diagram were generated. These are presented in Figures 4-36 and 4-37 respectively. While the frequency distribution in Figure 4-36 can be compared with the TRAMES results in Figure 4-19, the different coordinate scales make such comparison somewhat difficult. Thus Figure 4-38 shows the TRAMES/CONDOR frequency distribution regenerated in the same coordinate system. Now comparing frequency distributions in Figures 4-36 and 4-38, the TRAMES/MINERVE calculations are clearly seen as more accurate than the TRAMES/CONDOR results. Thus it appears that a small difference in wind directions and speed, as calculated with MINERVE, is relatively important to the placement and size of the TRAMES plume, and more importantly on impact at the sensor locations. This sensitivity is

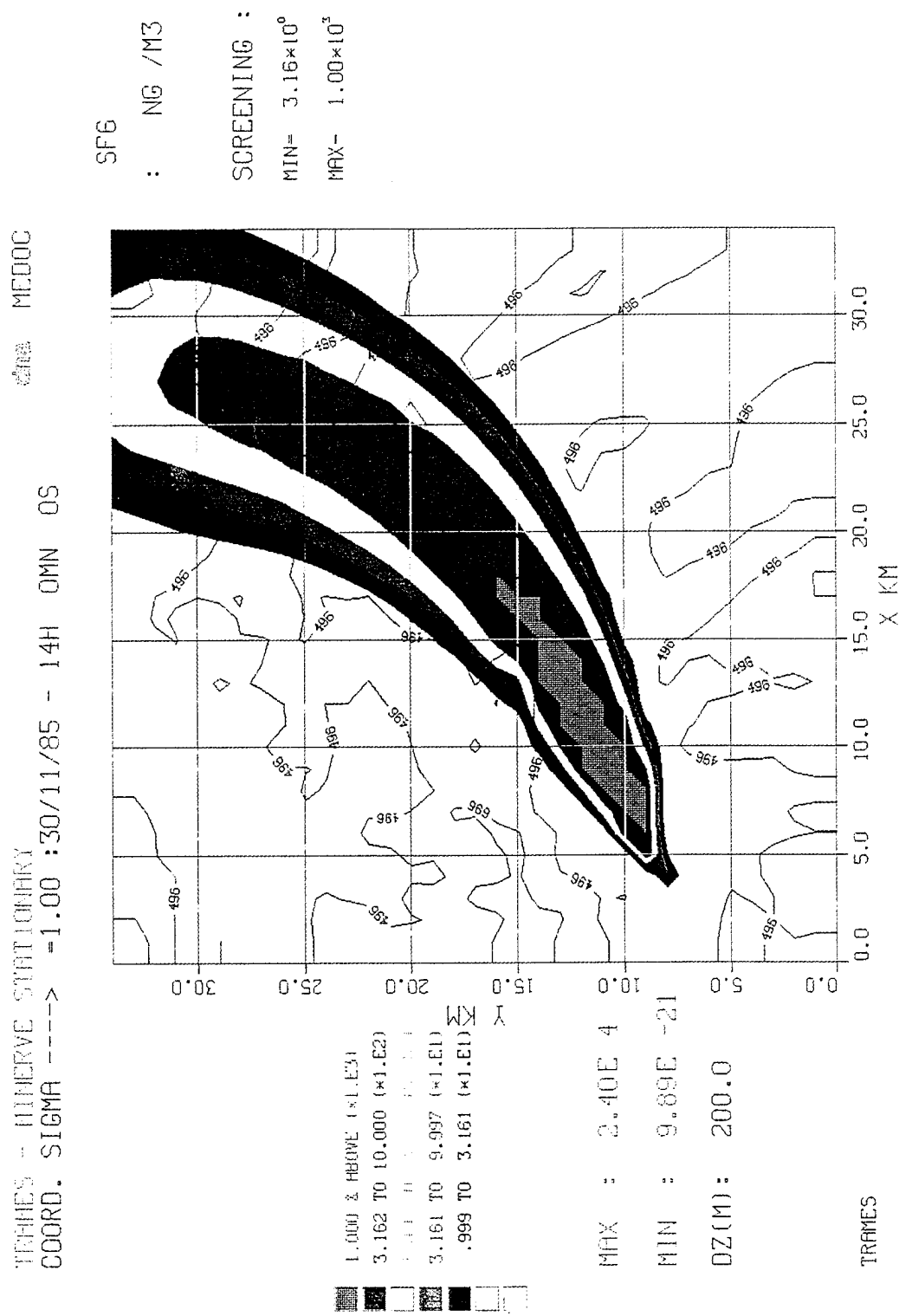


Figure 4-35. Ground level concentration contours with color shading for 30 November based on TRAMES with stationary MINERVE winds.

MEDOC DNA
TRAMES - MINERVE STATIONARY 30/11/85 14H

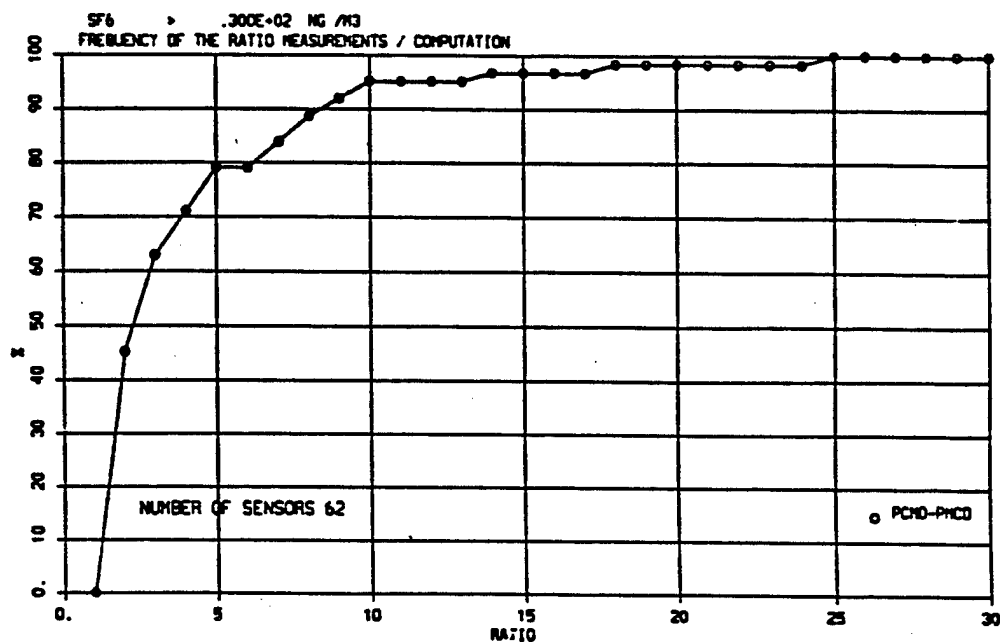


Figure 4-36. Cumulative frequency distribution for TRAMES calculations with stationary MINERVE winds on 30 November.

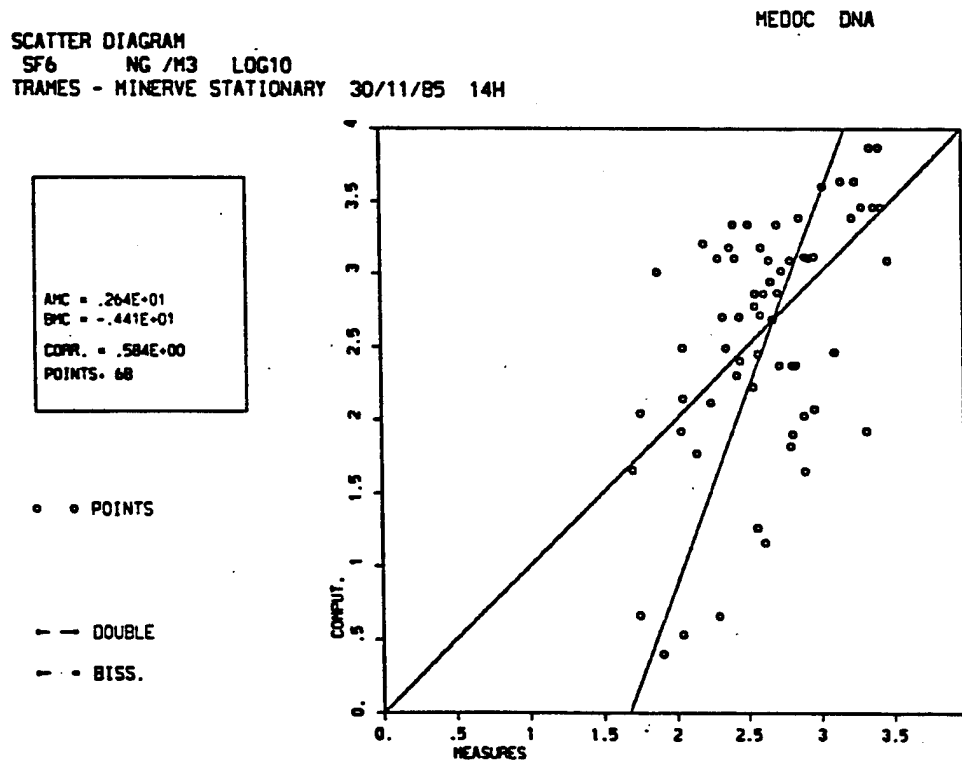


Figure 4-37. Scatter diagram for TRAMES calculations with stationary MINERVE winds on 30 November.

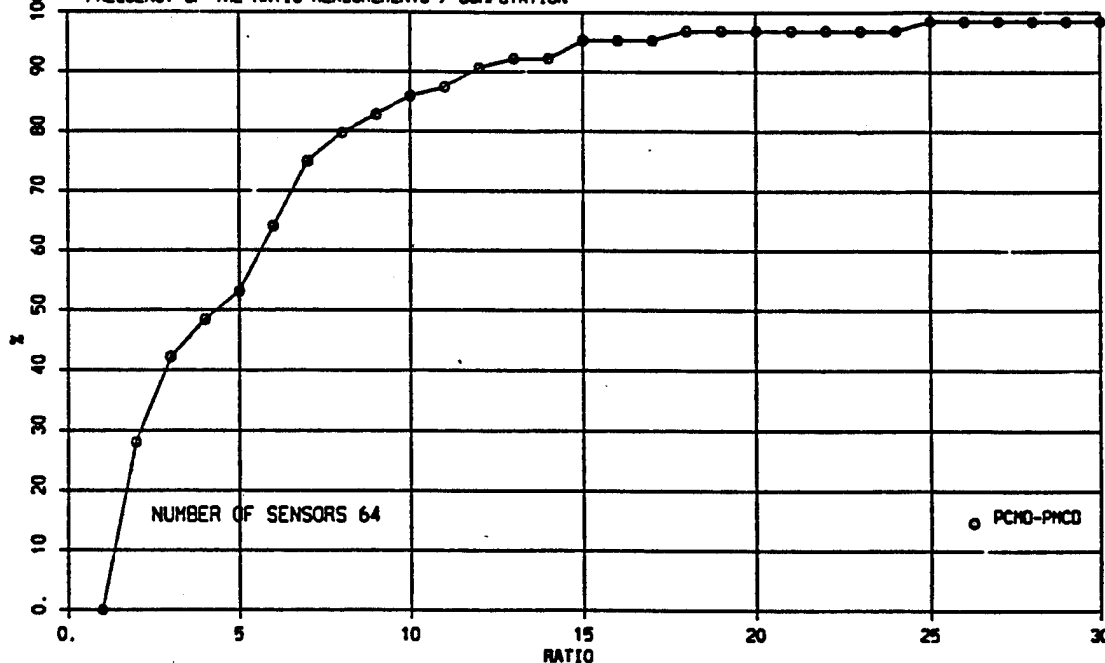
MEDOC DNA

TRAMES - CONDOR 30/11/85 14H

STATIONARY

SF6 > .300E+02 NG /M3

FREQUENCY OF THE RATIO MEASUREMENTS / COMPUTATION



TRAMES DATE = 30/11/85 - 14 H 0 MN 0 S.

Figure 4-38. Cumulative frequency distribution for TRAMES calculations with CONDOR winds on 30 November.

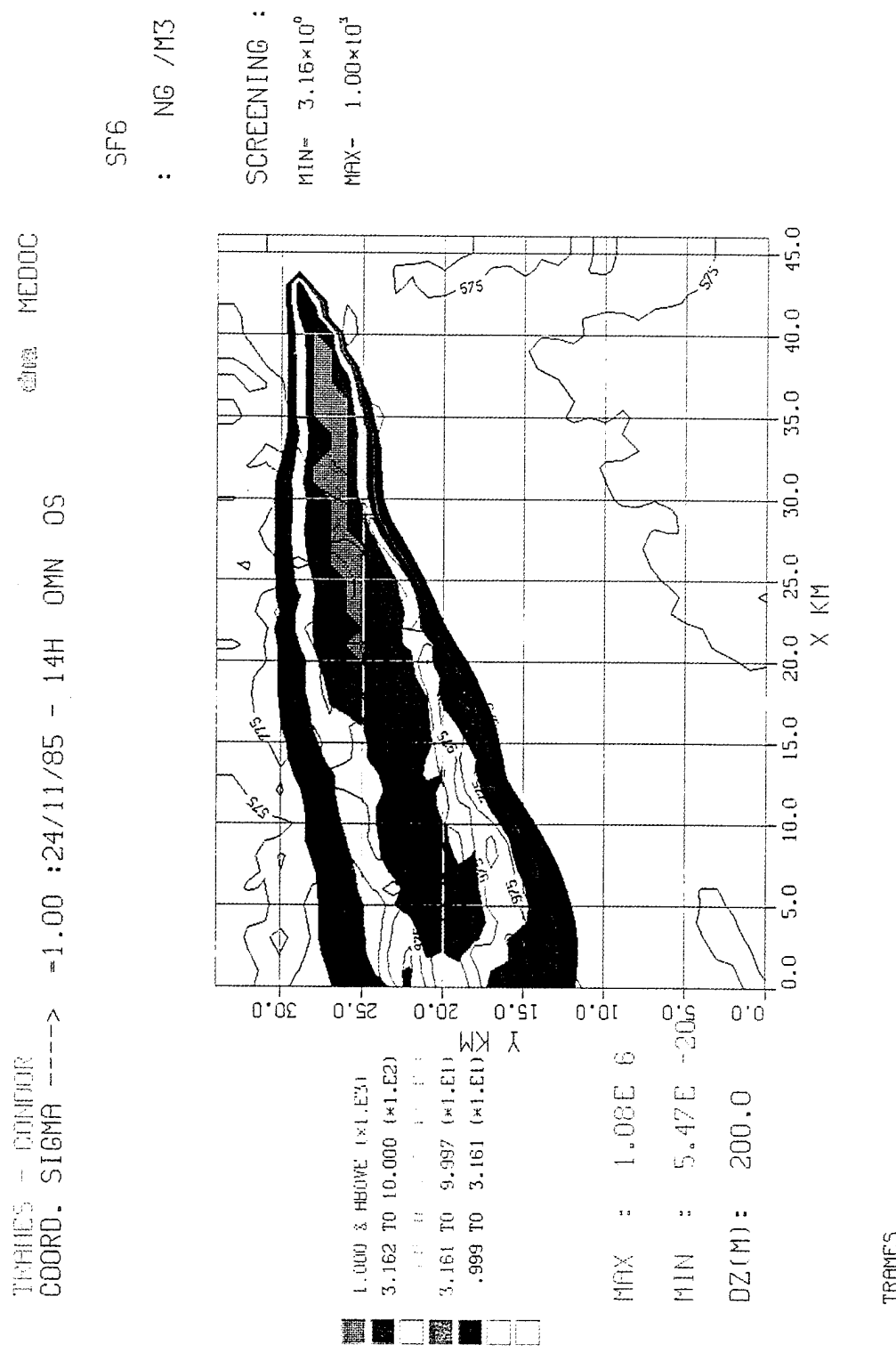


Figure 4-39. Ground level concentration contours with color shading for 24 November based on TRAMES with CONDOR winds.

believed to be a result of the relative narrowness of the TRAMES plume. For example, similar calculations using MINERVE with the relatively diffuse HERMES plume calculations showed minimal differences in accuracy. Turning to the scatter diagrams for the MINERVE and CONDOR driven TRAMES calculations (Figures 4-37 and 4-34), the MINERVE scatter is apparently less, though not clearly so. Comparison of correlation coefficients shows a slightly better value for MINERVE than for CONDOR (.584 vs .555). In any case the overall consistency and approximate agreement between modeling approaches and measurements can be interpreted as further validation of MINERVE.

Turning to the 24 November SIESTA Experiment, TRAMES ground level concentrations calculated for the CONDOR wind field are displayed in Figure 4-39. Surprisingly in this case, the TRAMES plume is blown almost entirely into the northern mountains, with little or nothing in the main valley where most sensors were located. As a result, with double screening as performed by PSI, too few points are obtained for meaningful determination of frequency distribution. This conceivably happened for a number of the other models in the PSI evaluation and is possibly the reason frequency distributions were not presented for the 24th as they were for the 30th of November.

To further evaluate TRAMES on the 24th, the MINERVE stationary wind field, which led to improve results with HERMES, was also used with TRAMES. The resulting ground level concentration profile is shown in Figure 4-40. Using MINERVE winds, the TRAMES plume is seen to be significantly diverted to a more southerly trajectory, thus giving a plume somewhat similar to the HERMES results with calculated values in both the north valley and the main valley to the south. As for 30 November, however, the TRAMES plume is narrower with higher concentrations toward the centerline. The frequency distribution and correlation coefficient for TRAMES using stationary MINERVE winds is given in Figures 4-41 and 4-42 respectively. While much better than the TRAMES/CONDOR results, the new results are still not as good as HERMES. With a correlation coefficient of 0.526, the TRAMES calculations with stationary MINERVE winds are classified as average for such a topography.

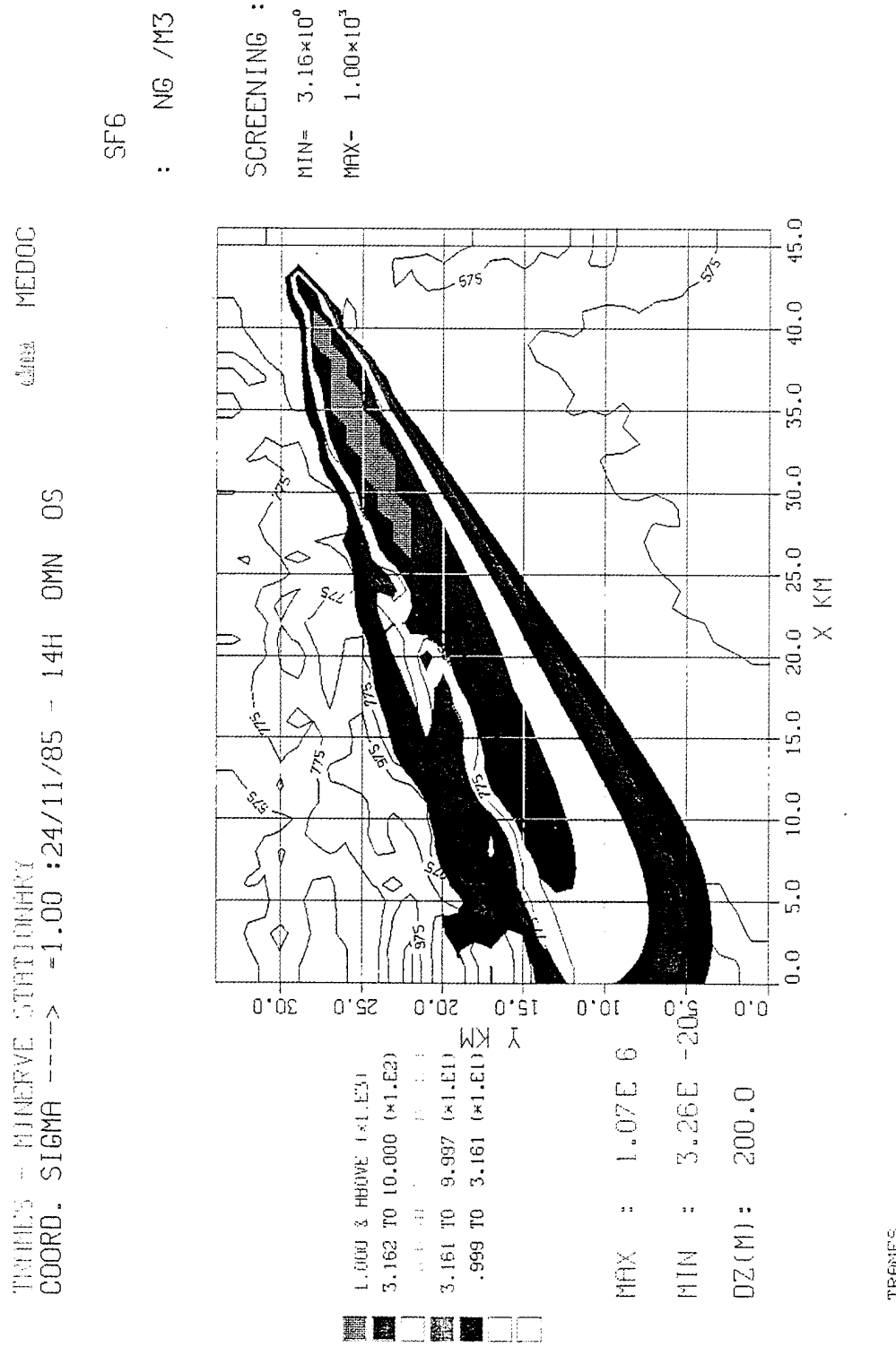


Figure 4-40. Ground level concentration contours with color shading for
 24 November based on TRAMES with stationary MINERVE winds.

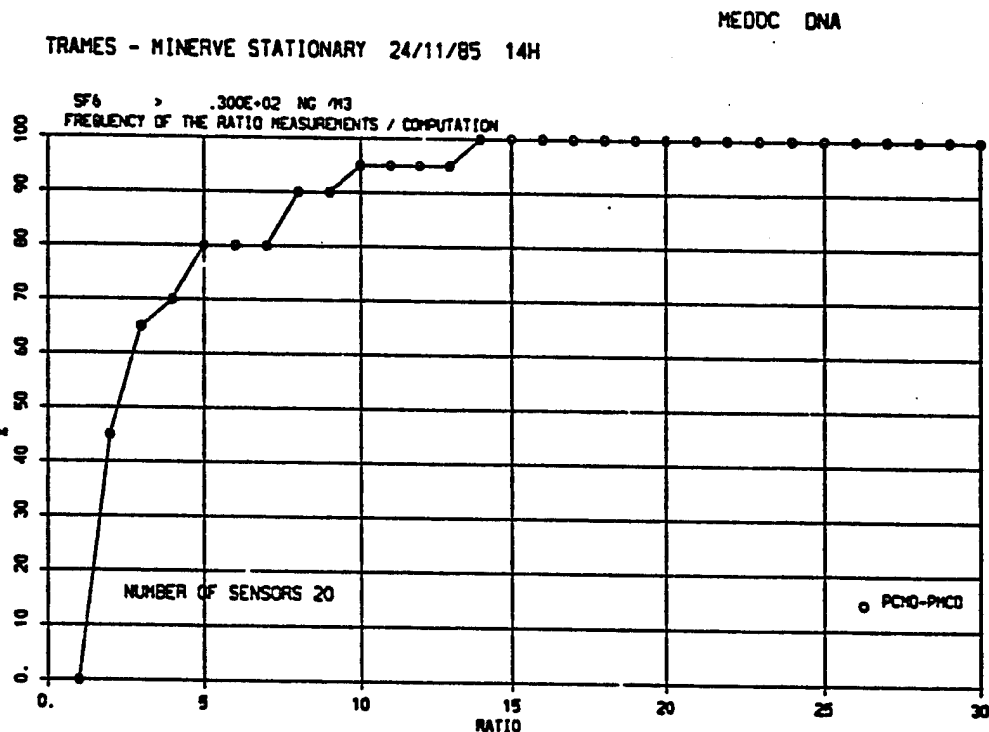


Figure 4-41. Cumulative frequency distribution for TRAMES calculations with stationary MINERVE winds on 24 November.

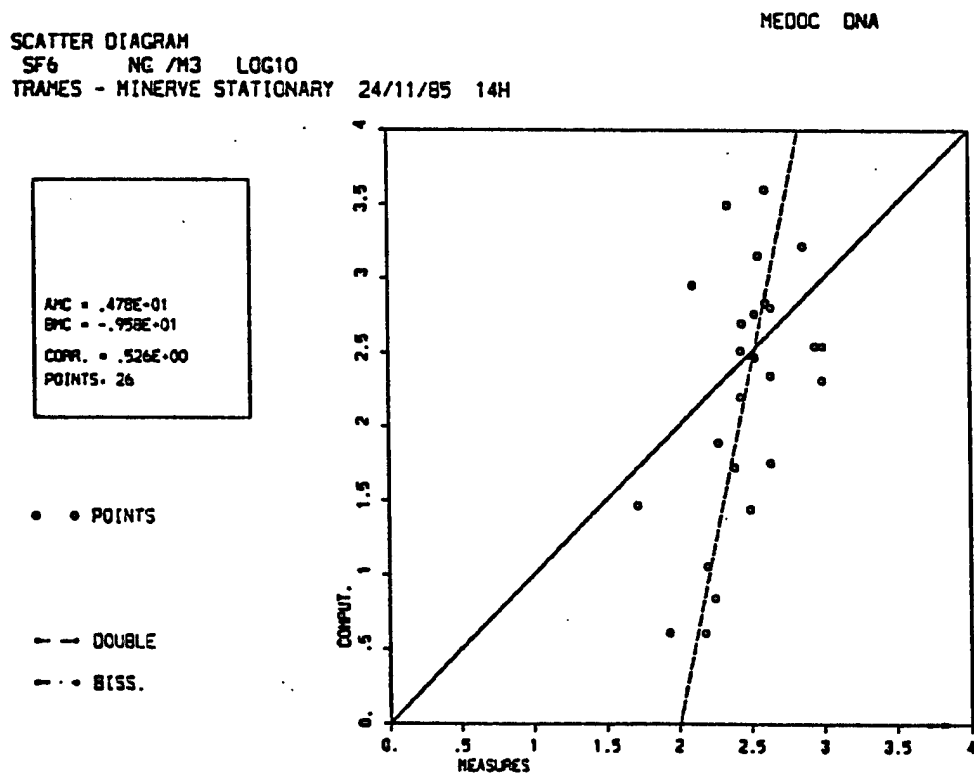


Figure 4-42. Scatter diagram for TRAMES calculations with stationary MINERVE winds on 24 November.

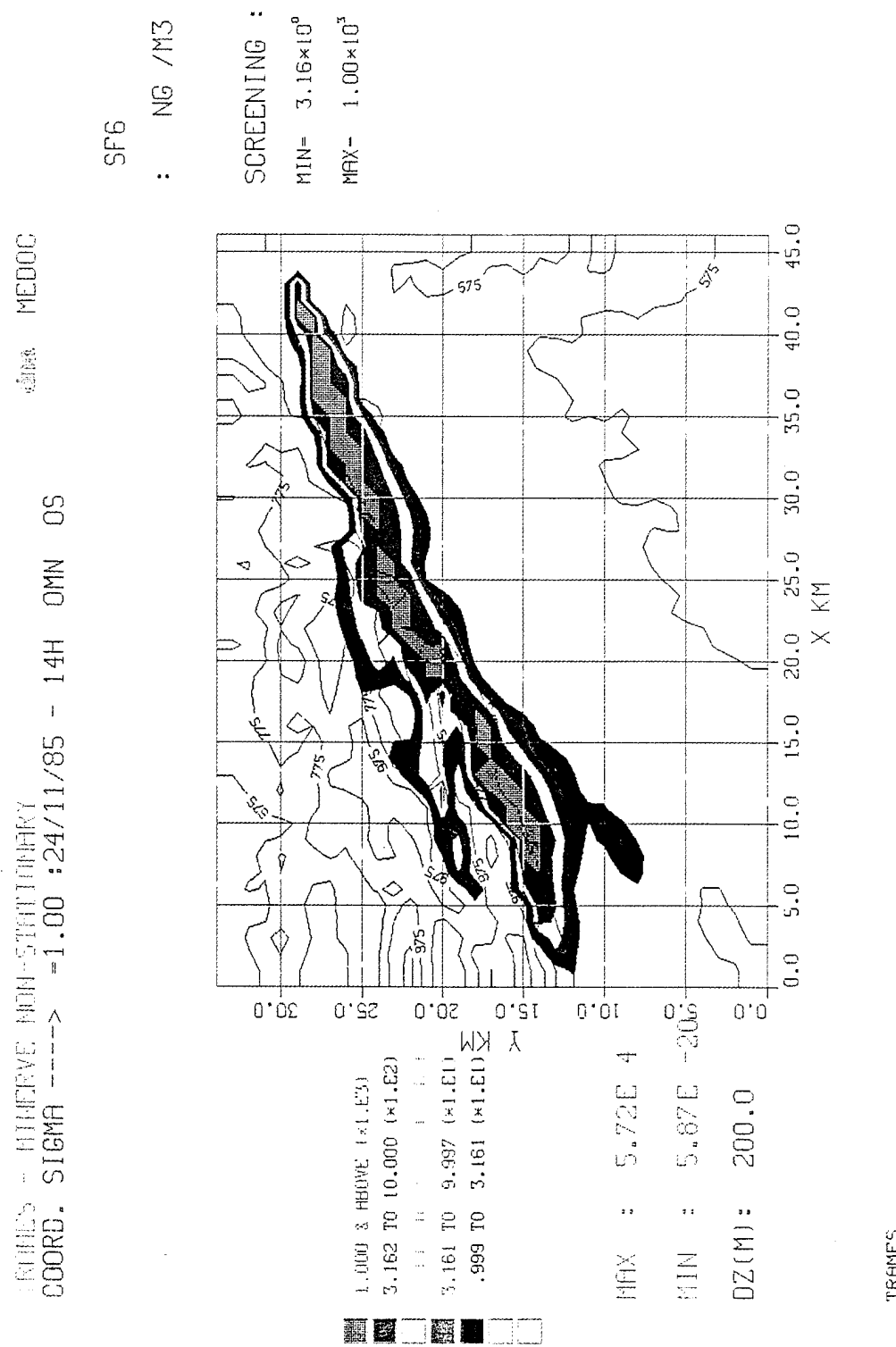


Figure 4-43. Ground level concentration contours with color shading for
24 November based on TRAMES with nonstationary MINERVE winds.

ADSO TRAJECTORIES. 24/11/85 14H 0
 FRAMES - MINERVE NON STATIONARY - 24/11/85 14H
 0: 24/11/85 8H 0MN -> 24/11/85 14H 0MN

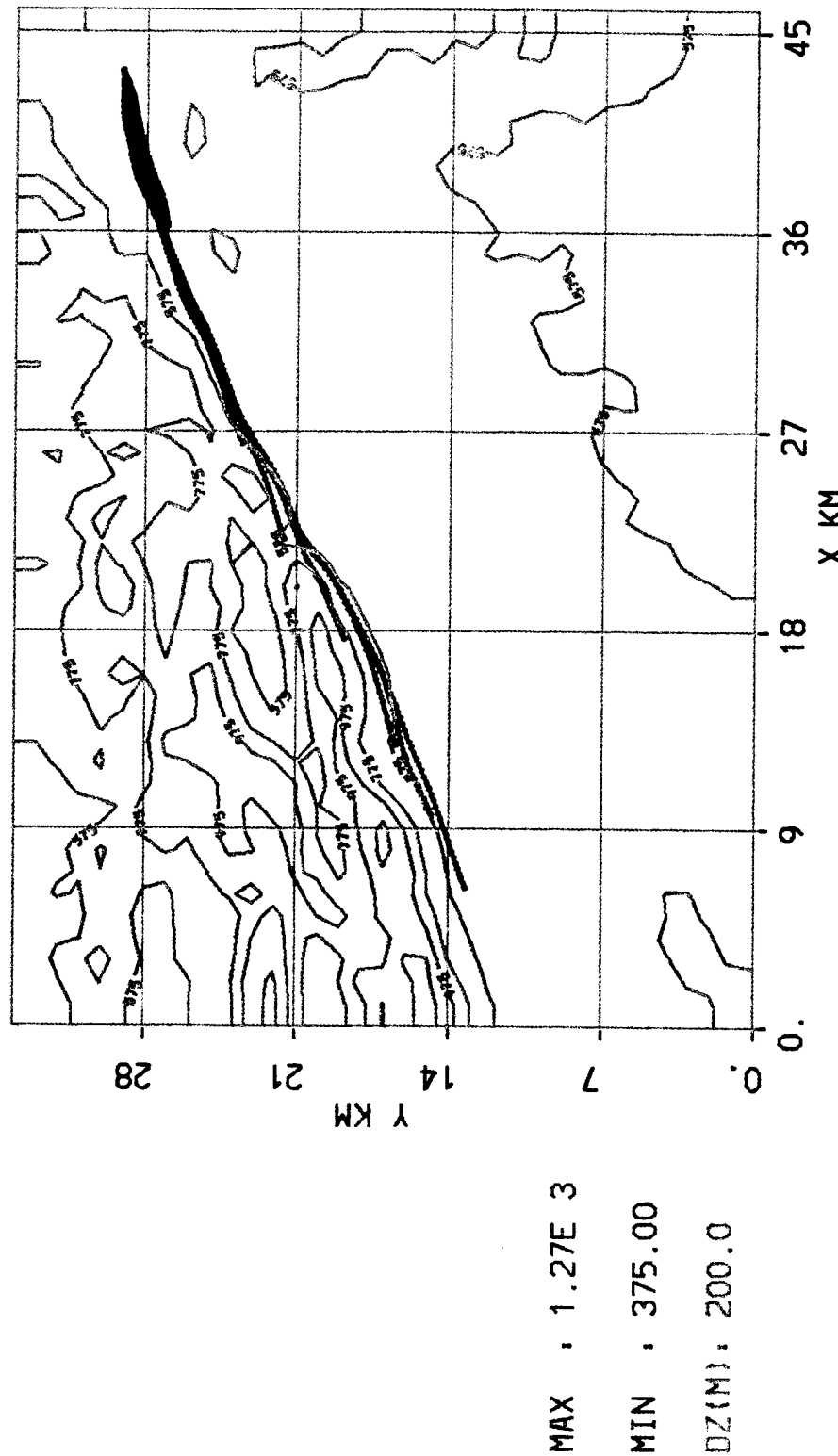


Figure 4-44. TRAMES trajectories for nonstationary MINERVE winds on 24 November.

Applying TRAMES with the nonstationary MINERVE wind field gives the ground level concentrations shown in Figure 4-43. Compared with ground level concentrations based on stationary MINERVE winds (Figure 4-40), the plume is narrower and more structured but with approximately the same placement. Impacts are found in both the north and the main valleys. The frequency distribution and scatter diagrams are not significantly different from the stationary case. In general the TRAMES calculations have been found to be less accurate than HERMES. Given good wind fields, the plume trajectories appear to be quite good. The TRAMES trajectories for the nonstationary MINERVE winds are shown in Figure 4-44. The trajectories are seen to follow along the south side of the Jura Ridges, allowing possible impact in both the north and main valleys. The amount and extent of this impact to the north and south of course depends on the amount of lateral spreading in the TRAMES model. According to the SIESTA data comparisons, both the 24th and the 30th of November, this lateral spreading was apparently underestimated. The amount of such spreading was calculated by means of the Pasquill-Gifford (P-G) correlations with stability classes. While the P-G correlations have been used extensively and found to provide reasonable approximations, it is not uncommon in rough complex terrain for modelers to use a higher (more unstable) stability class than normal, thus accounting for added turbulence due to terrain roughness. Such an adjustment to TRAMES for the SIESTA cases will increase lateral spreading and lower centerline concentrations, both of which should improve agreement with the SIESTA data. Unfortunately, the available time and resources did not allow this expectation to be investigated.

SECTION 5

CONCLUSIONS

MEDOC represents a comprehensive capability for determining the impact of nuclear, biological, and chemical releases in the atmosphere. It includes the effects of complex terrain and applies over a range of scales from 100's of KM to 10's of KM, with the ability to efficiently operate at resolutions as fine as 100 m. The MEDOC codes predict concentrations and dosages as well as the underlying meteorology. They can be driven by an irregular network of weather stations or by regular gridded data from larger scale forecast models and archived data sources. The codes have been extensively validated over a period of approximately 10 years, i.e., since their development was initiated. They are operational on both supercomputers (CRAY) and workstation level platforms (IBM RISC/6000). MEDOC has been installed on DNA workstations where it has been applied to a variety of problems by DNA personnel. The codes have been specifically adapted to applications and operating requirements of the DNA.

MEDOC is comprised of codes, for both the meteorology and the material transport. In addition, alternate methodologies are provided to give the user options between models which are based on more accurate first principles modeling or more approximate but computationally efficient approaches. As a result, MEDOC is very well suited to a wide variety of applications/operating modes requiring a range of modeling response times and fidelity. For example, emergency response at the local scale which requires computations within minutes, can be readily achieved on a workstation with the more approximate MEDOC codes. For regional scale calculations, where immediate response is not necessary, and where higher fidelity is desired, the first principles MEDOC codes can be applied. Other applications for which MEDOC can be used very effectively include planning exercises and parametric analyses requiring numerous solutions, often involving extensive sets of statistical/climatological data. The more approximate computationally efficient MEDOC codes are ideally suited for such applications, with the higher fidelity codes also being useful in such cases for benchmark purposes. Because MEDOC involves a system of codes which can be operated independently, e.g., wind field generators and concentration/dosage solvers, its elements can be advantageously

coupled with other meteorological and concentration models to improve their performance. The MINERVE mass consistency code, for example, has been used to provide initial conditions for nonhydrostatic meteorological codes and to generate 3D wind fields for other (non-MEDOC) material transport/diffusion models. At DNA, MINERVE output files are used to supply improved 3D wind fields for concentration calculations with the SCIPUFF/HASCAL codes. With MEDOC's ability to provide emergency response as well as to perform in a complementary capacity with other models, it also constitutes a potentially valuable element for other capabilities such as the DNA Hazardous Prediction and Assessment Capability (HPAC).

In summary, MEDOC is a validated, operational, and versatile capability at DNA which allows computationally efficient calculation of all facets of meteorological transport, dispersion, and impacts due to NBC materials released in the atmosphere.

SECTION 6

REFERENCES

1. Kaplan, M. L., Zack, J. W., Wong, V. C., and Tuccillo, J. J., "Initial Results from a Mesoscale Atmospheric Simulation System and Comparisons with an AVE-SESAME I Data Set," Monthly Weather Review, Vol. 110, pp. 1564-1590, 1982. (U)
2. SSESCO, "savi3D Environmental Work Bench Users Guide," Supercomputer Systems Engineering and Services Co., Minneapolis, MN, 1994. (U)
3. Louis, J. F., "A Parametric Model of Vertical Eddy Fluxes in the Atmosphere," Boundary Layer Meteorology, Vol. 17, pp. 187-202, 1979. (U)
4. Janvier, L., "Parametrisations de la Turbulence et de l'interface sol/atmosphère dans un modèle tridimensionnel à mesoscale," Doctoral Thesis, L'Ecole Centrale De Lyon, October 1987. (U)
5. Therry, G., and Lacarrere, P., "Improving the Eddy Kinetic Energy Model for Planetary Boundary Layer Description," Boundary Layer Meteorology, Vol. 25, pp. 63-88, 1983. (U)
6. Businger, J. A., Wyngaard, J.C., Izumi, Y., and Bradley, E. F., "Flux-Profile Relationships in the Atmospheric Surface Layer," Journ. Atmos. Sci., Vol. 28, pp. 181-189, 1971. (U)
7. Perdriel, S., "Principles and Basic Equations of the HERMES Model," ARIA Technologies Report No. ARIA/93.008, Colombes, France, 1993. (U)
8. Perdriel, S., "HERMES Users Manual," ARIA Technologies Report No. ARIA/93.016, Colombes, France, 1993. (U)
9. Perdriel, S., "Note De Principe Du Code MINERVE 4.0," ARIA Technologies Report No. ARIA/94.019, Colombes, France, 1994. (U)
10. "Notice D'Utilisation Du Code MINERVE 4.0," ARIA Technologies Report No. ARIA/94.020, Colombes, France, 1994. (U)
11. Perdriel, S., "TRAMES General Design Manual - Release 5.1," ARIA Technologies Report, Colombes, France, 1992. (U)

REFERENCES (Continued)

12. Tinarelli, G., et al., "Lagrangian Particle Simulation of Tracer Dispersion in the Lee of a Schematic Two-Dimensional Hill," Journal of Applied Meteorology, Vol. 33, pp. 744-756, 1994. (U)
13. Moussiopoulos, Flassak, Th., and Knittel, G., "A Refined Diagnostic Wind Model," Computer Techniques in Environmental Studies, Computational Mechanics Publications, Southampton, Boston, 1988. (U)
14. Athey, G. F., Sjoreen, A. L., Ramsdell, J. V., and McKenna, T. J., "RASCAL Version 2.0 User's Guide," U.S. Nuclear Regulatory Commission, Report No. NUREG/CR-XXXX. (U)
15. Sykes, R. I., Lewellen, W. S., and Parker, S. F., "A Gaussian Plume Model of Atmospheric Dispersion Based on Second-Order Closure," Journal of Climate and Applied Meteorology, Vol. 25, pp. 322-331, 1986. (U)
16. Geai, P., Perdriel, S., and Caneill, J. Y., "Assessing the Transport-Diffusion of Effluents at Mesoscale - An Application to the Rhone River Valley Area," AMS - Ninth International Symposium on Turbulence and Diffusion, San Diego, CA, April, 1988. (U)
17. Finardi, S., et al., "Boundary-Layer Flow over Analytical Two-Dimensional Hills: A Systematic Comparison of Different Models with Wind Tunnel Data," Boundary Layer Meteorology, Vol. 63, pp. 259-291, 1993. (U)
18. Khurshudyan, L. H., Synder, W. H., and Nekrasov, I. V., "Flow and Dispersion of Pollutants over Two-Dimensional Hills," U.S. Envir. Prot. Agency, Rpt. No. EPA-600/4-81-067, Research Triangle Park, NC, 1981. (U)
19. Gassmann, F., and Buerki, D., "Experimental Investigations of Atmospheric Dispersion over the Swiss Plain - Experiment SIESTA," Boundary Layer Meterology, Vol. 41, pp. 295-307, 1987. (U)
20. Herrnberger, V. R. D., Doria, P., and Prohaska, G., "Atmospheric Dispersion of Radioactivity in Complex Terrain: Model Evaluation and Selection for Real Time Emergency Applications," Proceedings of the Seminar on Environmental Impact of Nuclear Installations, Univ. of Fribourg, Fribourg, Switzerland, Sept. 1992. (U)
21. Flassak, T., and Moussiopoulos, N., "CONDOR3, Calculation of Non-Divergent Flowfields over Rough Terrain, Level 3.0, Version PSI-3.37," from Kaufmann, P., and Gallus, M., CH-5232 Villigen PSI, 1990. (U)

DISTRIBUTION LIST

DNA-TR-94-182

DEPARTMENT OF DEFENSE

DEFENSE INTELLIGENCE AGENCY

2 CY ATTN: ANDY GIBB/PAX-3
ATTN: DIW-4
ATTN: PAX-5B G WEBER

DEFENSE NUCLEAR AGENCY

2 CY ATTN: ISST
ATTN: PMPA DR C GALLOWAY
ATTN: WEL
ATTN: WELE LTC JIM HODGE
ATTN: WELE LTC M BYERS
ATTN: WELE MAJ D MYERS
ATTN: WELE MAJ R COX

DEFENSE TECHNICAL INFORMATION CENTER

2 CY ATTN: DTIC/OCP

FIELD COMMAND DEFENSE NUCLEAR AGENCY

ATTN: FCTO
ATTN: FCTT DR BALADI

JOINT STAFF/J-8

ATTN: J8 WAR FIGHTING DIV

DEPARTMENT OF THE ARMY

ARMY RESEARCH LABORATORIES

ATTN: AMSRL-SL-CE

DEP CH OF STAFF FOR OPS & PLANS

ATTN: DAMO-NCZ

U S ARMY ATMOSPHERIC SCIENCES LAB

ATTN: SLCAS-AR-M R SUTHERLAND

U S ARMY ENGR WATERWAYS EXPER STATION

ATTN: C WELCH CEWES-SD-R
ATTN: CEWES-SS-E P GRAHAM
ATTN: CEWES-SS-R DR BALSARA
ATTN: D RICKMAN CEWES-SE-R
ATTN: E JACKSON CEWES-SD-R
ATTN: F DALLRIVA CEWES-SS-R

U S ARMY NUCLEAR & CHEMICAL AGENCY

ATTN: MONA-NU DR D BASH

U S ARMY RESEARCH LAB

ATTN: AMSRL-WT-TA G BULMASH
ATTN: SLCBR-SS-T

U S ARMY DUGWAY PROVING GROUNDS

ATTN: J BOWERS

U S ARMY EDGEWOOD RESEARCH,

ATTN: SCBRD-RT A STUEMPFL

DEPARTMENT OF THE NAVY

NAVAL RESEARCH LABORATORY

ATTN: CODE 5227 RESEARCH REPORT

NAVAL SURFACE WARFARE CENTER

ATTN: CODE K42 L VALGE
ATTN: R GIBBS

OFFICE OF CHIEF NAVAL OPERATIONS

ATTN: NUC AFFAIRS & INT'L NEGOT BR

DEPARTMENT OF THE AIR FORCE

AIR UNIVERSITY LIBRARY

ATTN: AUL-LSE

HQ USAF/XOFS

ATTN: XOFN

PHILLIPS LABORATORY

ATTN: PL/WS MR SHARP

USAF SPACE COMMAND

ATTN: LT OL CROSS

DEPARTMENT OF ENERGY

LAWRENCE LIVERMORE NATIONAL LAB

ATTN: PAUL GUDIKSEN

ATTN: R PERRETT

LOS ALAMOS NATIONAL LABORATORY

ATTN: A S MASON

ATTN: J NORMAN

ATTN: R W WHITAKER

ATTN: B SHAFER

OTHER GOVERNMENT

CENTRAL INTELLIGENCE AGENCY

ATTN: OSWR/NED 5S09 NHB

DEPARTMENT OF DEFENSE CONTRACTORS

AEROSPACE CORP

ATTN: P RAUSCH

AEROTHERM CORP

ATTN: C NARDO

APPLIED RESEARCH ASSOCIATES, INC

ATTN: J KEEFER

APTEK, INC

ATTN: T MEAGHER

BOEING TECHNICAL & MANAGEMENT SVCS INC

ATTN: D ECKBLAD

CALSPAN CORP

ATTN: M DUNN

ATTN: M HOLDEN

CARPENTER RESEARCH CORP

ATTN: H J CARPENTER

EASTWIND RESEARCH CORP

ATTN: RICHARD D SMALL

GENERAL ATOMICS, INC

ATTN: CHARLES CHARMAN

HORIZONS TECHNOLOGY, INC

ATTN: B KREISS

ATTN: B LEE

INSTITUTE FOR DEFENSE ANALYSES
ATTN: CLASSIFIED LIBRARY
ATTN: E BAUER

JAYCOR
2 CY ATTN: CYRUS P KNOWLES

KAMAN SCIENCES CORP
ATTN: T STAGLIANO

KAMAN SCIENCES CORP
ATTN: D MOFFETT

KAMAN SCIENCES CORPORATION
ATTN: DASIA

LOGICON R & D ASSOCIATES
ATTN: LIBRARY
ATTN: R ROSS

LOGICON R & D ASSOCIATES
ATTN: G GANONG

LOGICON R & D ASSOCIATES
ATTN: J WEBSTER

SCIENCE APPLICATIONS INTL CORP
ATTN: J STODDARD

SCIENCE APPLICATIONS INTL CORP
ATTN: D BACON
ATTN: J COCKAYNE
ATTN: J MCGAHAH
ATTN: P VERSTEEGEN
ATTN: W LAYSON

SCIENCE APPLICATIONS INTL CORP
2 CY ATTN: C DOUGHERTY
2 CY ATTN: J SONTOWSKI

SCIENCE APPLICATIONS INTL CORP
ATTN: J MANSCHIP

SRI INTERNATIONAL
ATTN: M SANAI

TECH REPS, INC
ATTN: F MCMULLAN

TITAN CORPORATION (THE)
ATTN: P HOOKHAM

TRW S I G
ATTN: NORMAN LIPNER